

**Probing the collectivity in  
neutron-rich Cd isotopes via  
 $\gamma$ -ray spectroscopy**

Inaugural-Dissertation

zur

Erlangung des Doktorgrades  
der Mathematisch-Naturwissenschaftlichen Fakultät  
der Universität zu Köln

vorgelegt von

**Farheen Naqvi**

aus Amroha, Indien

Köln, 2011

Berichtersteller:

Prof. Dr. Jan Jolie

Prof. Dr. Peter Reiter

Tag der mündlichen Prüfung:

16 Mai 2011

# Abstract

The spin and configurational structure of excited states of  $^{127}\text{Cd}$ ,  $^{125}\text{Cd}$  and  $^{129}\text{Cd}$ , having two proton and three, five and one neutron holes, respectively in the doubly magic  $^{132}\text{Sn}$  core have been studied. The isomeric states in Cd isotopes were populated in the fragmentation of a  $^{136}\text{Xe}$  beam at an energy of 750 MeV/u on a  $^9\text{Be}$  target of 4 g/cm<sup>2</sup>. The experiment was performed at GSI Darmstadt. The neutron-rich Cd isotopes were selected using the  $B\rho - \Delta E - B\rho$  method at the FRagment Separator (FRS). Event by event identification of fragments in terms of their  $A$  (mass) and  $Z$  (charge) was provided by the standard FRS detectors. The reaction residues were implanted in a plastic stopper surrounded by 15 Ge cluster detectors from the RISING array to detect the  $\gamma$  decays. In  $^{127}\text{Cd}$ , an isomeric state with a half-life of 17.5(3)  $\mu\text{s}$  has been detected. This yrast  $(19/2)^+$  isomer is proposed to have mixed proton-neutron configurations and to decay by two competing stretched  $M2$  and  $E3$  transitions. Experimental results are compared with the isotone  $^{129}\text{Sn}$ . In  $^{125}\text{Cd}$ , apart from the previously observed  $(19/2)^+$  isomer, two new metastable states at 3896 keV and 2141 keV have been detected. A half-life of 13.6(2)  $\mu\text{s}$  was measured for the  $(19/2)^+$  isomer, having a decay structure similar to the corresponding isomeric state in  $^{127}\text{Cd}$ . The higher lying isomers have a half-life of 3.1(1)  $\mu\text{s}$  and 2.5(15) ns, respectively. Time distributions of delayed  $\gamma$  transitions and  $\gamma\gamma$ -coincidence relations were exploited to construct decay schemes for the two nuclei. Comparison of the experimental data with shell-model calculations is also discussed. The new information provides input for the proton-neutron interaction in nuclei around the doubly magic  $^{132}\text{Sn}$  core. The  $\gamma$  decays of the isomeric states in  $^{129}\text{Cd}$  were not observed experimentally. The reasons for the non-observation of delayed  $\gamma$  rays for  $^{129}\text{Cd}$  are either an isomeric half-life of less than 93 ns based on the experimentally obtained isomeric ratios of the  $(19/2)^+$  in  $^{127,125}\text{Cd}$ , or an  $E3$  spin trap emerging from shell-model calculations.

# Zusammenfassung

Der Spin und die Konfiguration von angeregten Zuständen in  $^{127}\text{Cd}$ ,  $^{125}\text{Cd}$  und  $^{129}\text{Cd}$  wurden untersucht. Die Isotope entsprechen zwei Protonen- und drei, fünf bzw. ein Neutronen-Loch Konfigurationen im doppelt magischen Kern  $^{132}\text{Sn}$ . Die isomeren Zustände in den Cadmium-Isotopen wurden durch Fragmentation von  $^{136}\text{Xe}$  (750 MeV/u) an einem  $4\text{ g/cm}^2$   $^9\text{Be}$  Target populiert. Das Experiment wurde an der GSI Darmstadt durchgeführt. Die neutronenreichen Cadmium-Isotope wurden mittels der  $B\rho - \Delta E - B\rho$  Methode am FRagment Separator (FRS) selektiert. Zur Bestimmung der Masse ( $A$ ) und Kernladungszahl ( $Z$ ) der Fragmente wurden die Standard-FRS Detektoren eingesetzt. Die zu untersuchenden Fragmente wurden in einen passiven Stopper implantiert, der von 15 Ge Detektoren des RISING Arrays umgeben war, um  $\gamma$  Zerfälle zu messen. In  $^{127}\text{Cd}$  wurde ein isomerer Zustand mit einer Halbwertszeit von  $17.5(3)\ \mu\text{s}$  gefunden. Für diesen isomeren  $(19/2)^+$  Yrast-Zustand, der über  $M2$  und  $E3$  Übergänge zerfällt, wird eine gemischte Proton-Neutronen Konfiguration vorgeschlagen. Die experimentellen Ergebnisse wurden mit dem Isoton  $^{129}\text{Sn}$  verglichen. In  $^{125}\text{Cd}$  konnten neben dem zuvor beobachteten  $(19/2)^+$  Isomer zwei neue metastabile Zustände bei 3896 keV und 2141 keV nachgewiesen werden. Für das  $(19/2)^+$  Isomer, das eine ähnliche Zerfallsstruktur wie das entsprechende Isomer in  $^{127}\text{Cd}$  aufweist, wurde eine Halbwertszeit von  $13.6(2)\ \mu\text{s}$  gemessen. Die höheren-energetischen Isomere haben eine Halbwertszeit von  $3.1(1)\ \mu\text{s}$  und  $2.5(15)\ \text{ns}$ . Das Zerfallsschema für die beiden Kerne konnte anhand von  $\gamma\gamma$ -Koinzidenzen und der Zeitspektren der Gammaübergänge erstellt werden. Die experimentellen Daten wurden mit Schalenmodellrechnungen verglichen und konnten so neue Informationen über die Proton-Neutron Wechselwirkung in der Region um den doppelt magischen Kern  $^{132}\text{Sn}$  liefern. Die Ursache für das Fehlen verzögerter  $\gamma$ -Emissionen für  $^{129}\text{Cd}$  sind entweder eine isomere Halbwertszeit von weniger als 93 ns, begründet durch die experimentell bestimmten Isomerenverhältnisse des  $(19/2)^+$  Zustands in  $^{127,125}\text{Cd}$  oder die Ausbildung einer  $E3$  Drehimpulsfalle, wie es Schalenmodellrechnungen nahelegen.

*To my parents*



# Contents

Contents	i
List of figures	1
List of tables	7
<b>1 Introduction</b>	<b>9</b>
<b>2 The Nuclear Shell Model</b>	<b>15</b>
2.1 Empirical Approach	17
2.2 Schematic Interactions	17
2.3 Realistic Interactions	17
2.4 Transition rates	19
<b>3 Experimental Techniques</b>	<b>21</b>
3.1 Acceleration facility at GSI	21
3.2 Production of exotic-nuclear beams	22
3.2.1 Production mechanism	22
3.2.2 Production yields	23
3.3 FRagment Separator (FRS)	23
3.4 Selection of the reaction residues by the $B\rho$ - $\Delta E$ - $B\rho$ technique	24
3.5 Identification of the ions: Principle and the equipment	27
3.5.1 $A/Z$ determination	29
3.5.2 $Z$ identification	33
3.6 Calibration of the FRS detectors	36
3.6.1 Multi-wire proportional chamber calibration	36
3.6.2 MUSIC calibration	36
3.6.3 Scintillator calibration	37
3.7 Implantation of the ions	40
3.8 The RISING cluster array	42
3.8.1 Technical details	43

<b>4</b>	<b>Data Analysis</b>	<b>47</b>
4.1	Particle selection . . . . .	47
4.2	Removal of contaminants . . . . .	48
4.3	Gamma-ray spectroscopy . . . . .	49
4.3.1	Energy calibration . . . . .	51
4.3.2	Add-back principle . . . . .	52
4.3.3	Lifetime analysis . . . . .	54
4.3.4	Building level schemes . . . . .	56
<b>5</b>	<b>Results</b>	<b>63</b>
5.1	$^{127}\text{Cd}$ . . . . .	63
5.2	$^{125}\text{Cd}$ . . . . .	72
5.3	Isomeric ratios . . . . .	92
5.4	$^{129}\text{Cd}$ . . . . .	93
<b>6</b>	<b>Discussion</b>	<b>97</b>
6.1	Shell-model interaction . . . . .	97
6.2	Structure of the odd Cd isotopes . . . . .	98
6.3	The role of proton-neutron interaction in $^{132}\text{Sn}$ region. . . . .	103
<b>7</b>	<b>Outlook</b>	<b>109</b>
7.1	Slowed Down Beams at GSI : A test measurement . . . . .	110
7.1.1	Experimental Problems . . . . .	111
7.1.2	Experimental setup . . . . .	116
7.1.3	Results . . . . .	118
	<b>Bibliography</b>	<b>123</b>

# List of Figures

1.1	Sequence of the single-particle energy orbitals in shell model. . . . .	10
1.2	Excitation energy of yrast $2^+$ states in Cd, Te, Xe, Ba and Ce isotopic chains. . . . .	12
2.1	Schematic representation of the free nucleon-nucleon potential. . . . .	18
3.1	A schematic diagram of the FRS. . . . .	24
3.2	Effect of the angle of degrader wedges on the momenta of fragments for an achromatic setting. . . . .	26
3.3	Effect of the angle of degrader wedges on the momenta of fragments for a monochromatic degrader. . . . .	27
3.4	An example of phase-space of a fragment beam achieved using achromatic and monochromatic focusing. . . . .	28
3.5	Fragment separator with its particle identification detectors. . . . .	29
3.6	Readout of the cathodes of multi-wire proportional chambers. . . . .	31
3.7	Readout of the scintillator detectors. . . . .	32
3.8	Readout electronics for anode strips of multi-sampling ionization chambers. . . . .	34
3.9	(a): Energy loss in MUSIC41 as a function of multi-wire MW41 position in X direction. The curve has some distortions at the ends which are needed to be corrected for good Z resolution. (b): The corrected curve for energy loss to remove the position dependence. . . . .	35
3.10	Energy loss in MUSIC41 as a function of primary beam velocity. . . . .	35
3.11	Z deduced from the energy loss information in MUSIC41. . . . .	37
3.12	The time difference $dt$ from two ends of SC21 versus the position in multi-wire MW21. . . . .	38
3.13	The product of primary beam velocity $\beta$ and measured time-of-flight as a function of $\beta$ . . . . .	39
3.14	The Z versus A/Z identification plot for the fragments. . . . .	40

3.15	Count rate in scintillator SC43 as a function of S4 degrader thickness. . . . .	41
3.16	A schematic layout of seven HPGe crystals from a RISING cluster detector. . . . .	42
3.17	Energy versus time matrix for the $\gamma$ rays associated with the decay of $^{127}\text{Cd}$ . . . . .	44
3.18	Width of the prompt flash in time. . . . .	45
3.19	The energy versus time matrix of $\gamma$ rays for an energy range of 50 keV to 4 MeV and a time window of 25 $\mu\text{s}$ after the ion implantation. . . . .	46
4.1	The $Z$ information extracted from the two ionization chambers. . . . .	48
4.2	Position of Cd isotopes at S2 as a function of their $A/Z$ ratio. . . . .	49
4.3	Horizontal position of the Cd isotopes at S4. . . . .	50
4.4	The energy loss of the fragments in SC42 versus the energy loss in MUSIC42. . . . .	50
4.5	Left: The calibrated gamma spectrum of $^{126}\text{In}$ for lower energies with 1 keV/ch and 0.25 keV/ch calibration factors. Right: $^{152}\text{Eu}$ energy spectrum. The 0.25 keV/ch improves the resolution of doublets present at energies 1085.8 keV and 1089.7 keV considerably. . . . .	51
4.6	Multiplicity distribution of 7 crystals in a RISING cluster. . . . .	52
4.7	Difference in time as a function of difference in energies of gamma radiations recorded in two neighbouring crystals. . . . .	54
4.8	(a): The comparison between the intensity of a 121.8 keV $\gamma$ transition before and after add back. (b): The spectrum showing the increase in the intensity of 963.8 keV transition after add back. . . . .	55
4.9	Energy spectra for $^{125}\text{Cd}$ with time windows of 380 ns to 3 $\mu\text{s}$ and 7 $\mu\text{s}$ to 11 $\mu\text{s}$ after implantation. . . . .	58
4.10	Prompt and delayed coincidence $\gamma$ spectra of 869.3 keV transition in $^{125}\text{Cd}$ . . . . .	59
4.11	A typical $\gamma\gamma\Delta t$ matrix gated on 198.0 keV transition in $^{125}\text{Cd}$ . . . . .	60
4.12	(a): The symmetric Gaussian distribution of relative time between two prompt-coincident $\gamma$ transitions. The red line is the zero time. (b): Relative time distribution of two delayed $\gamma$ rays with a shift in the centroid with respect to zero time. . . . .	62
5.1	Singles gamma-ray energy spectrum of $^{127}\text{Cd}$ . . . . .	64
5.2	$\gamma\gamma$ -coincidence spectra of five gamma transitions assigned to the decay of $^{127}\text{Cd}$ . . . . .	65

5.3	The sum of time distributions of the 711.2, 738.8, 821.2 and 848.9 keV transitions with a single exponential decay fit. . . .	67
5.4	The two relative time spectra showing symmetric distribution with respect to the zero time. . . . .	69
5.5	The proposed level schemes for $^{127}\text{Cd}$ . . . . .	70
5.6	Singles gamma-ray energy spectrum of $^{125}\text{Cd}$ . . . . .	73
5.7	The singles gamma-ray energy spectra for $^{125}\text{Cd}$ with two different time windows after the ion implantation. . . . .	74
5.8	Prompt $\gamma\gamma$ -coincidence relations of 665.9 keV and 796.6 keV transitions. . . . .	76
5.9	Prompt $\gamma\gamma$ -coincidence spectra gated on 719.5 keV and 742.9 keV transitions. . . . .	78
5.10	Prompt $\gamma\gamma$ -coincidence spectra gated on 487.2 keV, 924.9 keV and 975.3 keV. . . . .	79
5.11	Delayed $\gamma\gamma$ -coincidence spectra gated on 719.5 keV and 742.9 keV. . . . .	80
5.12	Prompt $\gamma\gamma$ -coincidence spectra gated on 99.2 keV, 786.4 keV and 869.3 keV transitions. . . . .	81
5.13	Prompt $\gamma\gamma$ -coincidence spectra gated on 198.0 keV, 480.6 keV, 269.8 keV and 408.7 keV transitions. . . . .	83
5.14	(a) and (b): Time distribution of 198.0 keV transition relative to the 786.4 keV $\gamma$ line and the 869.3 keV $\gamma$ line, respectively. (c) and (d): Time distribution of 269.8 keV transition relative to the 786.4 keV $\gamma$ line and the 869.3 keV transition, respectively. The red line represents the zero time. Centroids of all the distributions are shifted forward in time indicating the emission of 786.4 keV and 869.3 keV $\gamma$ lines before the 198.0 keV and 269.8 keV transitions. . . . .	84
5.15	(a): The reference zero time line (in red) and the shifts in centroids of relative time distributions of 198.0 keV and 269.8 keV transitions with respect to the 408.7 keV and 480.6 keV transitions, respectively, in time units. (b) is similar to (a) with an addition of centroid shifts of relative time distribution between the 198.0 keV, 269.8 keV, 408.7 keV and 480.6 keV transitions and 786.4 keV and 869.3 keV transitions. . . . .	85
5.16	The time distribution of 198.0 keV transition (a), 269.8 keV transition (b), 408.7 keV transition (c) and 480.6 keV transition (d) relative to 786.4 keV $\gamma$ line added to the analog distributions relative to 869.3 keV $\gamma$ line. . . . .	86

5.17 (a): Time distribution of 198.0 keV transition relative to 480.8 keV $\gamma$ line. (b): Time distribution of 269.8 keV transition relative to 408.7 keV $\gamma$ line. . . . .	87
5.18 (a): Sum of time distributions of the 269.8, 408.7, 480.6, 786.4 and 869.3 keV transitions with a single exponential decay fit. (b): Sum of time distributions of the 719.5 keV and the 742.9 keV transitions originating from the isomeric state at 1462 keV with a two-component exponential decay fit. . . . .	88
5.19 The proposed decay schemes for $^{125}\text{Cd}$ with tentative spin and parity assignments of the excited states. . . . .	91
5.20 Singles $\gamma$ -ray energy spectrum of $^{129}\text{Cd}$ for an energy up to 1000 keV (a) and the full energy range of 4000 keV (b). Both of the spectra do not contain any characteristic $\gamma$ lines from the decay of this nucleus. Background lines are marked with an asterisk (*). . . . .	95
6.1 Theoretically calculated level scheme for $^{129}\text{Cd}$ . . . . .	99
6.2 The proposed level schemes for $^{127}\text{Cd}$ and the theoretically calculated spectra using SM and LSSM interactions. . . . .	100
6.3 The proposed level scheme for $^{125}\text{Cd}$ and the SM calculated energies of the excited levels. . . . .	102
6.4 Single particle (hole) energy levels in $^{132}\text{Sn}$ and $^{208}\text{Pb}$ . . . . .	105
6.5 Systematics of the energy of $15/2^-$ , $13/2^-$ levels in $^{125,127,129}\text{Cd}$ and their analogue, $2_2^+$ and $2_1^+$ states in the neighboring even $^{128}\text{Cd}$ . . . . .	108
7.1 $B(E2)$ values of the first excited $2^+$ states in the even-even Cd isotopes. . . . .	110
7.2 Simulated angular spread of a $^{64}\text{Ni}$ beam after slowing down in an Al degrader. . . . .	112
7.3 The simulated yield of contaminants from nuclear reactions. . . . .	113
7.4 Simulated energy straggling of a $^{64}\text{Ni}$ beam after slowing down to 13 MeV/u. . . . .	114
7.5 The time-of-flight spectrum between scintillators SC21 and SC41 at FRS. . . . .	115
7.6 A cross sectional view of microchannel plate (MCP) surface. . . . .	115
7.7 Two microchannel plate detectors with chevron configuration of the channels. . . . .	116

7.8	Left: A schematic layout of the secondary electron emission microchannel plate detector with electrostatic mirror taken from Ref. [86]. Right: A picture of the secondary electron detector based on microchannel plates used for beam tracking and TOF measurement in the present experiment. . . . .	117
7.9	Left: Time-of-flight spectrum between the two MCP detectors separated by a distance of 10 cm. A triple alpha source was used for the measurement. Right: An image of mask placed in front of the Mylar foil of one of the MCP detectors. A position resolution of 1.5 mm was obtained for both horizontal and vertical directions of the MCP. . . . .	118
7.10	A schematic setup for the slowed down beam experiment. . . . .	119
7.11	Left: $\Delta E$ in Si detector versus the energy distribution of the slowed down $^{64}\text{Ni}$ beam. The results were compared to simulations (right). The plot shows that the $^{64}\text{Ni}$ ions are mostly stopped in Si detector whereas contaminants produced in the nuclear reactions in degrader punch through it. This gives an estimate of the range of energy of the background contaminants. . . . .	119
7.12	Left: The X coordinate from MCP1 versus the X coordinate from MCP2. Only the events lying in the straight cut are correlated. Right: The Y versus X image of MCP1. The events lying inside the gate shown in red were further analysed. . . . .	120
7.13	Energy distribution of $^{64}\text{Ni}$ ions after slowing down. . . . .	121
7.14	Simulated counts in the photopeak of gamma transitions from $2^+ \rightarrow 0^+$ and $4^+ \rightarrow 2^+$ populated in the Coulomb excitation of $^{64}\text{Ni}$ on a $^{197}\text{Au}$ target of $0.76 \text{ mg/cm}^2$ thickness. . . . .	122



# List of Tables

3.1	The characteristic resolving power and momentum and angular acceptance of the FRagment Separator. . . . .	24
5.1	Summary of the measured relative gamma intensities and the half-lives of isomeric states in $^{127}\text{Cd}$ . . . . .	66
5.2	Experimental transition strengths and branching ratios of $\gamma$ transitions in $^{127}\text{Cd}$ . . . . .	71
5.3	Summary of the relative gamma intensities and half-lives of isomeric states in $^{125}\text{Cd}$ , obtained by fitting the time distributions of individual gamma transitions. . . . .	75
5.4	The shift in the centroid of relative time distributions from the reference zero time. . . . .	88
5.5	Experimental reduced transition strengths for $\gamma$ rays decaying from the state at 1462 keV in $^{125}\text{Cd}$ . . . . .	89
5.6	Experimentally measured isomeric ratio of the states in $^{125}\text{Cd}$ and $^{127}\text{Cd}$ . . . . .	93
6.1	Experimental and shell-model transition strengths and branching ratios of gamma transitions in $^{127}\text{Cd}$ . . . . .	100
6.2	Experimental and shell-model calculated transition strengths and $\gamma$ -branching ratios in $^{125}\text{Cd}$ . . . . .	101
6.3	$E2$ transition rates between the high-spin states in $^{125}\text{Cd}$ calculated by shell model. . . . .	103
6.4	The wave function partitions of $15/2^-$ , $13/2^-$ states in $^{125,127,129}\text{Cd}$ and their analogue, $2_2^+$ and $2_1^+$ states in $^{128}\text{Cd}$ . . . . .	107



# Chapter 1

## Introduction

A nucleus is a dense volume of neutrons and protons interacting via the strong binding nucleon-nucleon force. The structure exhibited by a nucleus is the consequence of this underlying nuclear interaction. In spite of the complicated many-body composition, nuclei possess structures marked by the orderly motion of their constituents. The many faceted aspects of nuclear structure all over the nuclear chart has been dealt with by theories to understand and build a consistent picture of the nucleon-nucleon interaction in the nuclear medium. The basic characteristics of this strong interaction has long been recognized, for example, the constant binding energy per nucleon for the heavy nuclei ( $BE(\frac{A}{Z}X_N) \propto A$ ) and the nuclear radius varying as  $R = r_0 A^{1/3}$ , suggests that the nuclear medium is incompressible and the nuclear force saturates. These empirical observations stem up to the idea, that the interaction governing the motion of the nucleons in a nucleus can be approximated by an average mean potential [1] with the nucleons moving independently in it.

The combination of above hypothesis and experimentally observed extra binding energy for the nuclei having specific number of neutrons and protons led to the development of shell model for the nucleons, analogous to that of the electrons in an atom. The nuclear shell model proposed by Mayer and Jensen [2, 3] provides a quantum mechanical description of the nuclear structure in terms of energy levels as shown in Fig. 1. The energy eigenstates are referred to as orbitals and are characterized by a set of quantum numbers such as total angular momentum,  $j$ , orbital quantum number,  $l$  and number of nodes of radial wavefunction,  $n$ . The first choice of Mayer and Jensen [2, 3] for nuclear potential as the harmonic oscillator combined with the spin-orbit coupling term  $\alpha(\vec{l} \cdot \vec{s})$  and the centrifugal force term  $\beta(\vec{l} \cdot \vec{l})$  resulted in groups of different  $j$  orbitals called shells with typical energy gaps of the order of few MeV between them. One of the major successes of this model was the explanation of the so-called *magic* numbers. The large energy gaps at specific

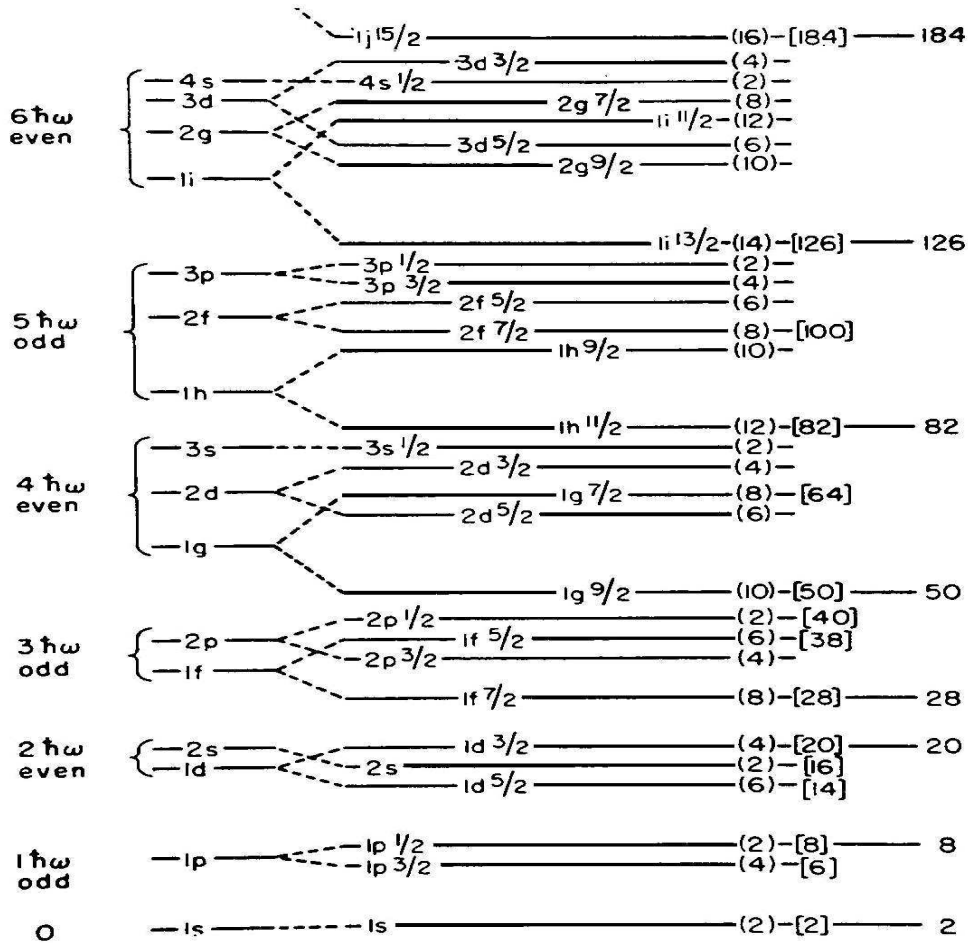


Figure 1.1: Single-particle energy states with harmonic oscillator potential as the one-body central potential. The degeneracy of the levels is resolved by adding a spin-orbit coupling term. On the right hand side, well known magic numbers are marked. Figure is taken from Ref. [4].

numbers of neutrons or protons make the nuclei favor the configurations with completely filled shells. The binding energies and ground state nuclear spins could also be predicted for most of the nuclei. The spins of the individual nucleons couple to give the total nuclear spin  $J$ . A nucleus with closed shells or filled orbitals has angular momentum zero since all possible substates of the  $J$  are filled, whereas the neighboring odd- $A$  nucleus with one valence nucleon (particle outside or missing from the filled shell) would have a spin  $J$  corresponding to the orbital in which the last odd nucleon stays. This is a

direct consequence of the independent particle motion and is supported by vast amount of experimental data on the odd- $A$  stable nuclei.

However, the structure of almost all the nuclei in their excited states show that the single-particle independent motion is not definitely the complete picture and the nucleons interact with each other. This interaction between the nucleons can be treated as a higher order perturbation to their independent motion and is known as the residual interaction. One of the ways of understanding the effect of the residual interaction on the structure of nuclei is a systematic study of the energies of their first excited states as a function of neutron and proton number.

Starting with doubly-magic nuclei, with both neutron and proton shells completely filled, the first excited states are often at an energy less than the corresponding shell gaps. This is a consequence of residual interaction leading to configuration mixing. The interaction between two particles (holes) scatters them to a different pair of orbitals compared to the initial ones. Such scatterings give rise to configurations of the resulting states with different occupancy patterns of nucleons over the valence orbitals. The mixing of all possible configurations with same total angular momentum  $J$  leads to rearrangement of their energies with further lowering of the corresponding lowest energy state. Departing away from the magic numbers and by adding both protons and neutrons (particles or holes) to the filled shells results in a large number of configurations coupled to a given  $J$  due to an overall increase in the pairs of interacting nucleons. As a consequence, an increased mixing and lowering of the first excited states is observed. The enhanced proton-neutron correlations in these cases give rise to a characteristic collective motion and the existence of low-lying yrast states in a nucleus is an experimental signature of collectivity.

As an example, the energies of the yrast  $2^+$  states in Xe, Ba, Ce, Te and Cd isotopes as a function of neutron number,  $N$ , are plotted in Fig. 1. For Te isotopes with two protons outside the  $Z = 50$  magic shell, the  $2^+$  excitation energy decreases smoothly as more and more neutrons are removed. The increasing number of neutron holes provide the enhanced configuration mixing and thus the gradual lowering of  $E(2^+)$ . Similar trend is observed for  $_{54}\text{Xe}$ ,  $_{56}\text{Ba}$  and  $_{58}\text{Ce}$  chains, the energy of  $2^+$  state is maximum at the  $N = 82$  neutron shell closure, while moving inside the neutron shell there is an expected monotonic decrease in  $E(2^+)$ . In the middle of the shells, often collective nuclear structures are encountered. However, in heavy neutron-rich  $_{48}\text{Cd}$  isotopes, the  $2^+$  excitation energy deviates from expected systematics. It first increases from  $N = 70$  to  $N = 76$  and a flattening of the  $E(2^+)$  curve occurs at  $N = 78$  and  $N = 80$ . The  $2^+$  energy in  $^{126}\text{Cd}$  is 6 keV larger than in the neighbouring  $^{128}\text{Cd}$  [5, 6]. This anomalous behaviour

of the neutron-rich Cd isotopes motivated the present work which deals with the investigation of the structure of excited states in  $^{125,127,129}\text{Cd}$  nuclei via gamma-ray spectroscopy.

With present day high-intensity radioactive beams [7, 8, 9, 10, 11, 12] and powerful radiation detection [13, 14] equipments, the exotic regions with extreme  $N/Z$  ratio such as neutron-rich Cd isotopes can also be explored. Testing theories built on the grounds of properties shown by stable nuclei in the region of extremes of nuclear existence would facilitate in building a self-consistent picture of the nucleon-nucleon interaction.

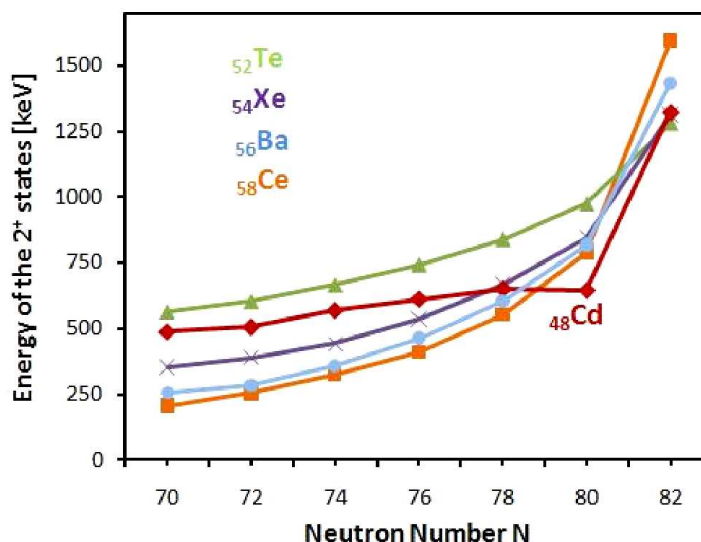


Figure 1.2: The systematics of the energy of first excited  $2^+$  states in Cd, Te, Xe, Ba and Ce as a function of neutron number  $N$ .

The neutron-rich Cd isotopes with  $Z = 48$  and valence neutron holes lie in the vicinity of doubly-magic  $^{132}\text{Sn}$  and thus are key points in probing the residual proton-neutron ( $\pi\nu$ ) interaction in a neutron-rich environment. The astrophysical rapid-neutron capture process, responsible for synthesis of heavy neutron-rich nuclei above Fe in nature follows a path along the  $N = 82$  line. To test theoretical models describing this process in the region around  $A = 130$ , the availability of experimental data on evolution of the  $N = 82$  shell gap is crucial. The predicted reduction of this gap [15, 16] led to the recent investigations on the structure of  $^{130}\text{Cd}$  [17] and  $^{131}\text{In}$  [18]. The energy of first excited  $2^+$  state in  $^{130}\text{Cd}$  indirectly points toward a robust shell closure at  $N = 82$ , which was confirmed by a direct measure of the shell gap

[18]. Missing evidence for a shell quenching in all these cases calls for a need to modify the mass model [19] explaining the abundances of  $A = 130$  nuclei in nature. Furthermore, unexpected lowering of the yrast  $2^+$  states in  $^{126}\text{Cd}$  and  $^{128}\text{Cd}$  [5, 6] was inferred as a consequence of an enhanced collectivity. The theoretical studies based on beyond mean field calculations with Gogny force explored the phenomenon and attributed it to the quadrupole deformation of states [20]. To gain more insight on this issue, a detailed comparison of experimental data on the excited states of odd Cd isotopes with theoretically predicted results was performed and an enhanced  $\pi\nu$  interaction was concluded to be the reason of prevailing collectivity in the region.

This thesis is divided into 7 chapters. In chapter 2, we lay out the theoretical framework of the thesis. In chapters 3 and 4, we present the experimental techniques and data analysis methods used in obtaining the experimental results. Chapter 5 summarizes the results obtained for three Cd isotopes studied and in chapter 6, we discuss the theoretical interpretation of the obtained results using shell-model calculations. Chapter 7 provides an outlook on the future research aspects along the lines of this work.



# Chapter 2

## The Nuclear Shell Model

The theoretical interpretation of the experimental results presented in this work will be compared with shell-model calculations. In this chapter, the basis of shell-model theory along with some of the concepts specific to the used calculations are discussed briefly. Detailed mathematical derivations are beyond the scope of this thesis, therefore the readers are encouraged to consult relevant references provided in the chapter.

The basic assumption of the shell model is the independent motion of each nucleon in a potential created by average interaction with the other nucleons in the nucleus. The Hamiltonian,  $H_0$ , for such a system of nucleons can be expressed as

$$H_0 = \sum_{i=1}^A [T_i + U_i], \quad (2.1)$$

with  $A$  denoting the total number of nucleons in the nucleus,  $T_i$  the kinetic energy of the  $i^{\text{th}}$  particle and  $U_i$  the one-body average potential.

However, in a many-nucleon system, because of the two-particle interaction,  $W(i, j)$ , the Hamiltonian generalizes to

$$H = \sum_{i=1}^A T_i + \sum_{1=i<j}^A W(i, j), \quad (2.2)$$

Using eq. (2.1), the above expression can be rewritten as

$$H = \sum_{i=1}^A [T_i + U_i] + \sum_{1=i<j}^A W(i, j) - \sum_{i=1}^A U_i = H_0 + H_{res}, \quad (2.3)$$

where  $H_{res}$  is the residual Hamiltonian defining the mutual interaction between the nucleons. It is treated as a small perturbation to the single-particle

Hamiltonian,  $H_0$ .

The perturbation theory provides a framework to compute the energy of the  $p^{\text{th}}$  state as a sum of single-particle energies,  $E_k^0$  and the contribution due to the residual interactions. The total energy of this state with its wave function,  $\psi_p$  expanded as linear combinations of the unperturbed basis states  $\phi_k^0$ , becomes

$$E_p a_{lp} = \sum_{k=1}^n \langle \phi_l^0 | H_0 + H_{res} | \phi_k^0 \rangle a_{kp}, \quad (2.4)$$

with

$$\psi_p = \sum_{k=1}^n a_{kp} | \phi_k^0 \rangle. \quad (2.5)$$

Since the unperturbed basis functions  $\phi_k^0$  are the eigenfunctions of  $H_0$  and  $E_k^0$  are the corresponding energy eigenvalues, one can write eq. (2.4) in the form of a matrix equation

$$\sum_{k=1}^n H_{lk} a_{kp} = E_p a_{lp}, \quad (2.6)$$

with an element of the Hamiltonian matrix also known as the two-body matrix element (TBME) being

$$H_{lk} = E_k^0 \delta_{lk} + \langle \phi_l^0 | H_{res} | \phi_k^0 \rangle. \quad (2.7)$$

To obtain the energy  $E_p$ , the matrix defined in (2.7) must be constructed and diagonalized. The resulting eigenvectors are the total wave functions,  $\psi_p$ . This phenomenon of defining certain states as a linear combination of unperturbed energy eigenfunctions is called configuration mixing, and the process conserves the total isospin and angular momenta of the states. In other words, configurational mixing takes place only between the states coupled to same angular momentum  $J$  and isospin  $T$ . Ref. [21] provides a detailed qualitative insight on the configurational mixing phenomenon, for mathematical formalism one can refer to [22, 23].

The large dimensionality of the matrix for a nucleus with  $\sim 100$  nucleons makes it impossible to diagonalize it for the whole basis space. Due to computational limitations, the large basis space is truncated. The extracted nucleon-nucleon interaction is therefore a modified effective two-body interaction which spans only a subset of the total basis space referred as the model space. The main aim of the shell-model calculations is to obtain the energy eigenvalues and the eigenfunctions for the mixed states by diagonalizing the effective Hamiltonian matrix, restricted to the model space. Once the wave

functions are obtained, several observables can be computed to explain the experimental data. In the following sections three main approaches to obtain the matrix elements for the effective two-body interaction are listed.

## 2.1 Empirical Approach

The two-body matrix elements and the single-particle energies for a particular mass region are obtained as the parameters of a fit to experimental data. This iterative procedure starts with an initial guess of the parameters which are used to diagonalize the Hamiltonian matrix. The calculated energies of the states are compared to the experimental energy spectrum and the parameters are adjusted by performing a least-square fit to describe the experimental data. The iteration is repeated until a good convergence is obtained. The effective interaction extracted using this approach is usually dependent on the set of experimental data taken and works well for a particular mass region. This approach has been very successful in estimating the binding energies and the energies of the excited states, however, the wave function description is still limited. For a more detailed discussion refer to [24].

## 2.2 Schematic Interactions

Some of the basic nuclear properties can be explained using simple schematic nucleon-nucleon interactions. For example, the characteristics like short-range nature of the nuclear force and saturation of the nuclear binding energies is very well simulated by delta interaction. The definition of the  $\delta$  function itself explains that an interaction scaling like a  $\delta$  function vanishes unless the active nucleons do not occupy the same spatial positions. Another widely discussed interaction explaining the tendency of the like nucleons to align their angular momenta as  $J^\pi = 0^+$ , is the pairing interaction. These schematic forms of the nucleon-nucleon interaction allows one to perform analytical calculation of the effective two-body matrix elements (TBME).

## 2.3 Realistic Interactions

In this approach, the effective interaction is constructed starting from the parametrized bare nucleon-nucleon force in free space. The inputs to the parameters of the free nucleon-nucleon force come from phase shifts observed in between the incoming and outgoing waves describing the scattered nucleons

in the  $pp$  and  $np$  scattering experiments. The resulting two-body nuclear interaction consists of a short-range repulsive part and a long-range attractive part. The repulsive part, often referred as a hard core increases with decreasing distance between the nucleons. In Fig. 2.3, a schematic representation of the nucleon-nucleon force as a function of internucleon distance in the spin singlet configuration ( $S = 0$ ,  $T = 1$ ) is shown.

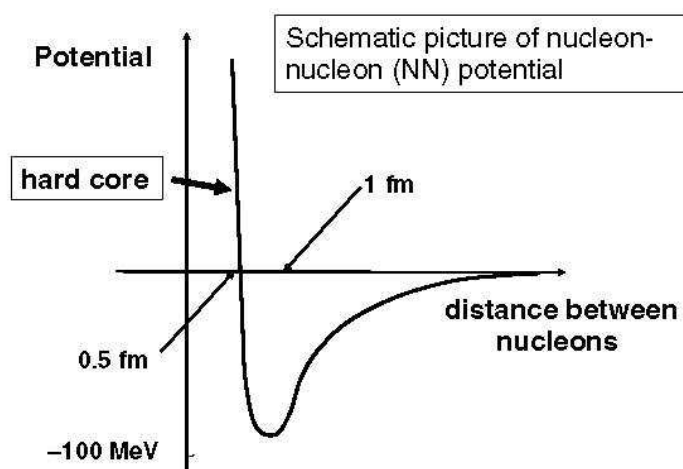


Figure 2.1: Schematic representation of the nucleon-nucleon potential. At an approximate internucleon distance of 0.5 fm, the force starts to be repulsive and the region is referred as hard core.

Extraction of the effective interactions from realistic nucleon-nucleon forces  $V_{N-N}$  involves a many-body perturbation technique in which the effects of excluded Hilbert space are taken into account. A detailed mathematical formalism of this can be found in [25]. The property of  $V_{N-N}$  going to infinity at small internucleon distances poses a mathematical problem in calculating the TBME. The matrix elements become very large or even infinite in this region. This problem is solved by using one of the very successful approaches based on Brueckner's G-matrix theory [26]. The resulting effective interactions are well behaved in repulsive hard core region.

Kuo and Brown derived first such interaction for the  $A = 18$  nuclei ( $sd$  shell) [27] starting from the Hamada-Jonston [28] description of the bare nucleon-nucleon force. Later this technique was extended to the  $fp$  model space and one of the widely used effective interaction in this region is that of Hjorth-Jensen and collaborators [29].

## 2.4 Transition rates

A nuclear energy state having an average lifetime of  $\tau$ , makes a transition to a lower state by emitting a quanta of energy with a rate

$$\lambda = \frac{1}{\tau}. \quad (2.8)$$

This transition rate  $\lambda$  can be computed using Fermi's Golden rule

$$\lambda = \frac{2\pi}{\hbar} |\langle \psi_{j_f, m_f} | V_{int} | \psi_{j_i, m_i} \rangle|^2 \rho(f), \quad (2.9)$$

which states that the transition rate is proportional to the square of the expectation value of interaction  $V_{int}$  responsible for transition between the initial state  $\psi_{j_i, m_i}$  and final state  $\psi_{j_f, m_f}$  and the density of final energy states  $\rho(f)$ .

Introducing a notation,  $T_{fi}(\omega L)$  to specify the electric and magnetic type of transitions, the above expression can be formulated as

$$T_{fi}(\omega L) = \frac{8\pi(L+1)}{L(2L+1)!!^2} \frac{1}{\hbar} \left(\frac{E_\gamma}{\hbar}\right)^{2L+1} |\langle \psi_{j_f, m_f} | o(\omega L, M) | \psi_{j_i, m_i} \rangle|^2, \quad (2.10)$$

where  $E_\gamma$  is the energy of the quanta and  $o(\omega L, M)$  is the corresponding multipole operator.

The matrix elements of  $o(\omega L, M)$  are made independent of the projection quantum number  $M$  by applying the Wigner-Eckart theorem. The resulting matrix elements are the reduced matrix elements,  $\langle \psi_{j_f} || o(\omega L) || \psi_{j_i} \rangle$  and the reduced transition probability  $B(\omega L, j_i \rightarrow j_f)$  is defined as

$$B(\omega L, j_i \rightarrow j_f) = \frac{1}{2j_i + 1} \langle \psi_{j_f} || o(\omega L) || \psi_{j_i} \rangle^2. \quad (2.11)$$

The transition rate in terms of the reduced transition probability then becomes

$$T_{fi}(\omega L) = \frac{8\pi(L+1)}{L(2L+1)!!^2} \frac{1}{\hbar} \left(\frac{E_\gamma}{\hbar}\right)^{2L+1} B(\omega L, j_i \rightarrow j_f). \quad (2.12)$$

In a model dependent calculation, the projections of the total wave function onto the model space  $M$  are used. Therefore, the probabilities of transitions which are dependent on the wave functions of initial and final states do not give correct physical estimates of true transition rates, when calculated only for a subset of full basis space. To account for the missing transition probabilities, a concept of effective charge of protons ( $e_\pi$ ) and neutrons ( $e_\nu$ ) and effective orbital  $g$ -factor ( $g_l$ ) and effective spin  $g$ -factor ( $g_s$ ) is introduced.

These quantities differ for different multipoles of the transitions, however in a given model space constant values for effective charge and effective  $g$ -factors should give good approximation of the rates of similar transitions.

The physical meaning of effective charge for an  $E2$  transition can be understood by assuming the inert core of nucleus as a uniformly charged sphere, polarized due to interaction with surrounding valence nucleons. This polarization of core modifies the magnitude of valence charge which can be expressed as a constant  $\delta(e_{\pi,\nu})$  added to the free values of the neutron and proton charges.

# Chapter 3

## Experimental Techniques

The experiment in which  $^{129}\text{Cd}$ ,  $^{127}\text{Cd}$  and  $^{125}\text{Cd}$  were produced was performed at the accelerator facility of GSI [30], Darmstadt. Fragmentation of a primary beam of  $^{136}\text{Xe}$  at energy 750 MeV/u on a  $^9\text{Be}$  target of 4 g/cm<sup>2</sup> thickness yielded the neutron-rich Cd isotopes along with other reaction products. Separation and identification of the heavy-ions was done at the FRagment Separator (FRS) [31]. Two settings of the FRS were realized, one optimized for maximum transmission of  $^{130}\text{Cd}$  and other one tuned to predominantly transmit  $^{126}\text{Cd}$ . To select ions of interest from the reaction products, the standard  $B\rho$ - $\Delta E$ - $B\rho$  method was employed and the FRS was operated in its achromatic mode. The present chapter is devoted to provide a detailed overview of the acceleration facility at GSI, the production of exotic nuclei and their separation and identification using particle detectors which are important building blocks of the FRS.

### 3.1 Acceleration facility at GSI

The existing accelerator facility at GSI comprises of the UNiVersal Linear ACcelerator system, UNILAC [32] coupled to heavy-ion synchrotron SIS18 [33]. Elements from hydrogen to uranium are accelerated in this accelerator complex. The UNILAC delivers beams with energies in the range from 3.0 to 13 MeV/u for heavy ions, and up to 15 MeV/u for light ions. It has a pre-acceleration stage where the ion sources are stationed. The primary beam nuclei produced in the first stage are stripped before being injected into the main linear accelerator, where the maximum possible energy is reached post-acceleration. The beam delivered by UNILAC has a pulsed structure with a typical spill length of few milliseconds. The different beams are then injected to SIS18 where they are accelerated up to 90% of the speed of light. The

entrance of the synchrotron is marked by a carbon foil used as a stripper. The most abundant charge state of  $73^+$  for uranium can be obtained in one injection. The maximum energy which can be reached for protons at SIS18 is 4.7 GeV, while for uranium, it extends up to 1 GeV/u. The beams can be either extracted in a slow or fast mode and are forwarded to the different experimental areas. Depending on the needs of experiments, the length of a beam spill can be adjusted to several microseconds in fast extraction and to several seconds in slow extraction. At FRS the slow extraction mode is utilized.

## 3.2 Production of exotic-nuclear beams

The in-flight separation methods used at the accelerator complex at GSI utilize fragmentation or fission of high-energy projectiles to produce secondary beams of exotic nuclei.

### 3.2.1 Production mechanism

The high-energy primary beams with intensities around  $10^9$  pps impinge on target materials with low  $Z$ , ejecting a variety of forward focused reaction residues. The heavy projectile-induced reactions at relativistic energies can be well explained by two-step abrasion-ablation model [34]. According to this theory two ions passing each other with an impact parameter small enough to lead an overlap in their volume, undergo a shearing away of the overlapping parts. This scrapping-off of the nucleons from the projectile nuclei is referred as "*abrasion*". The number of nucleons abraded in first step solely depends on the impact parameter [34]. The intermediate products (pre-fragments) are in thermalized excited states and de-excite by the evaporation of cascades of nucleons or light clusters. This evaporation phenomenon is called as "*ablation*" process. The loss of nucleons or light clusters continues until a proton-neutron ratio is reached where the probability to emit a proton or a neutron is similar [35, 36]. This results in the production of nuclei on the proton-rich side of the line of beta stability. During "*ablation*", fission may also take place for the fissile nuclei, leading to the medium-mass neutron-rich products.

The energy and momentum spread of the reaction residues predominantly depend on the mechanism driving their production. In peripheral fragmentation reaction the pre-fragments have nearly the same velocities as the projectile [37], with small differences arising from the fact that the sheared-off nucleons have to overcome the binding energies of the nuclei [38]. The re-

sulting momentum spread in a simple form is given by the model proposed by Goldhaber *et al.* [39].

### 3.2.2 Production yields

Yields of the secondary nuclei of interest  $N$  can be calculated using the relation

$$N = n\sigma I, \quad (3.1)$$

where  $n$  is the number of target nuclei,  $I$  is the beam intensity and  $\sigma$  is the reaction cross section. The choice of beam and target to produce the exotic nuclei of interest is based on the reaction cross sections. Codes like EPAX [40, 41], using the parametrization of experimental data from high-energy reactions or ABRABLA [34] based on the abrasion-ablation model can be used to estimate the production cross sections.

Production cross section of neutron-rich Cd isotopes using fragmentation of  $^{136}\text{Xe}$  beam on a  $^9\text{Be}$  target calculated from the EPAX 2 code is of the order of  $10 \mu\text{b}$ . The cross sections increase for less neutron-rich nuclei and hence, a large amount of side products were also produced in the experiment. To separate the fragments of interest from other reaction residues, they were guided to the FRagment Separator, a spectrometer designed to select the heavy-ions with relativistic energies.

## 3.3 FRagment Separator (FRS)

The FRagment Separator at GSI is a zero degree magnetic spectrometer with energy degrader used to separate the reaction residues isotopically. The system consists of four ion-optical focal planes (S1-S4), each characterized by a  $30^\circ$  dipole magnet and quadrupoles before and after each dipole as shown in Fig. 3.1. The  $B\rho$ - $\Delta E$ - $B\rho$  technique is exploited to select the nuclei to be studied. Achromatic and monochromatic modes of operation of the spectrometer give a freedom to focus the isotopically separated beams with small position and momentum spread, respectively, at the final focal plane (S4). Table 3.1 summarizes the general characteristics of the FRS. The finite momentum and angular acceptance of the FRS in combination with the losses of fragments along the beam line governs the transmission of nuclei to the exit of the separator. The total flight path through the spectrometer is  $\approx 72$  m which limits the lifetimes of the states populated in the production mechanism that can be studied at the final focal plane to few hundred nanoseconds. In section 3.4 an introduction of selection principle of the FRS

based on the  $B\rho$ - $\Delta E$ - $B\rho$  technique is given. Section 3.5 deals with the procedure of identification of the fragments and the particle detectors involved. A detailed overview of the FRS and its working principle can be found in Ref. [31].

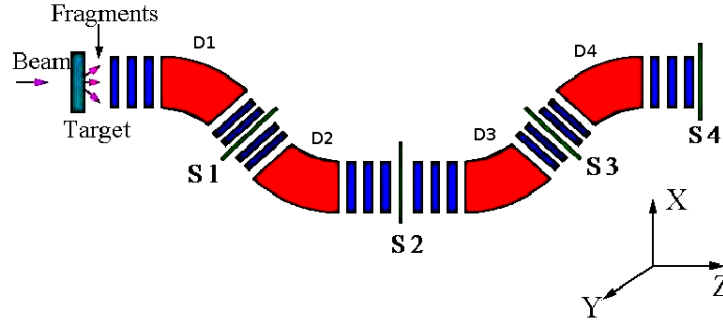


Figure 3.1: A schematic diagram of the FRS showing its four dipoles and the focal planes, S1, S2, S3 and S4.

Table 3.1: The characteristic resolving power and momentum and angular acceptance of the FRagment Separator.

Acceptance	Momentum : $\frac{\Delta p}{p} = \pm 1\%$
	Angle : $\Delta\theta = \pm 10$ mrad
Resolving power	$\frac{\Delta B\rho}{B\rho} = 1600$
	Maximum $B\rho = 18$ Tm

### 3.4 Selection of the reaction residues by the $B\rho$ - $\Delta E$ - $B\rho$ technique

**First  $B\rho$  selection:** The first two dipoles of the FRagment Separator act as the momentum filter for the ions. The selection principle is based on the Lorentz force  $\vec{F}_{Lorentz}$  exerted by a homogeneous magnetic field on a moving charged ion. The motion of the ion in this case is given by the Lorentz equation

### 3.4 Selection of the reaction residues by the $B\rho$ - $\Delta E$ - $B\rho$ technique

$$\vec{F}_{Lorentz} = q(\vec{v} \times \vec{B}), \quad (3.2)$$

where  $q$  and  $\vec{v}$  denote the charge and velocity of the ion and  $\vec{B}$  is the magnetic field it is moving in. The magnetic field in the dipoles of FRS is perpendicular to the velocity of traversing ions which forces them to follow a circular path. Hence, the centrifugal force due to circular motion of the ions balances the Lorentz force such that

$$F_{Lorentz} = \frac{mv^2}{\rho}, \quad (3.3)$$

where  $m$  is the mass of the particle and  $\rho$  is the radius of the circular path. Combining the two equations above one finds that the magnetic rigidity,  $B\rho$ , is

$$B\rho = \frac{mv}{q}. \quad (3.4)$$

For relativistic energies of the charged particles this expression provides a relation between the  $A/Q$  ratio of the fragments and their magnetic rigidity as

$$B\rho = \frac{A}{Q} \left( \frac{uc\beta\gamma}{e} \right), \quad (3.5)$$

with  $u$  being the atomic mass unit,  $A$  the atomic number of the ions,  $Q$  the ionic charge,  $c$  the speed of light and  $e$  the electron charge. The velocity  $\beta$  and the relativistic factor  $\gamma$  are given by the relations  $\beta = v/c$  and  $\gamma = \sqrt{1/(1-\beta^2)}$ , respectively. At the FRS, bending radius of the dipoles is fixed to  $\rho = 11.25$  m. For fully stripped ions,  $Q$  is the measure of their atomic number  $Z$ . The  $B$  fields of the four dipoles (D1, D2, D3 and D4) (see Fig. 3.1) are maintained in a way that ions with a particular  $A/Z$  ratio traverse central trajectory in the dipoles. The  $A/Z$  bands transmitted in first  $B\rho$  filtering stage depend on momentum and angular spread of the fragmentation residues. The position of arrival of the fragments at S2 after the second dipole is given by the expression

$$X_{S2}(p) = \left( \frac{\partial x}{\partial(\delta p)} \right)_{TA-S2} \frac{\Delta p}{p}, \quad (3.6)$$

where  $p$  is the momentum ( $\approx B\rho$ ) and  $\partial x/\partial(\delta p)$  is the horizontal dispersion of the fragments referred as  $D_{TA-S2}$  at the middle focal plane due to their initial momentum spread at the entrance of the separator. This momentum dependent spatial distribution of the ions is utilized by the profiled energy

degrader placed at the middle focal plane (S2) to introduce a change in the momentum of traversing ions in order to achieve either a monochromatic or achromatic characteristics.

**Energy loss in the degrader:** At S2, the fragments traverse a thick wedge-shaped material with variable thickness. The degrader system consists of a homogeneous wedge, a ladder and a disk [42]. The amount of matter in the beam path is varied by adjusting the wedge and the ladder thickness. The disk is inserted to change the angle of degrader in order to realize achromatic and monochromatic settings. By rotating the disk perpendicular to beam axis, a gradient in the thickness of degrader is acquired. Thus the thickness of material in the path of ions varies according to their horizontal point of arrival at the degrader. The energy loss of the ions with same  $A/Z$  ratio at this point can be optimized to focus the ions at the final focal plane (S4).

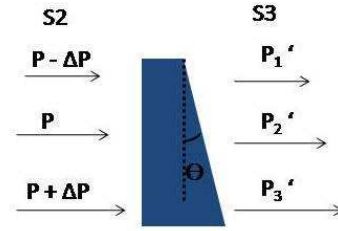


Figure 3.2: Effect of the angle  $\theta$  of degrader wedges on the momenta of fragments for an achromatic setting. As a consequence the fragments are focused at S4. See text for details.

For an achromatic mode, the energy loss of the same  $A/Z$  ratio arriving at different horizontal positions is such that the momentum dispersion introduced by the first two dipoles gets compensated at the final focal plane by the second  $B\rho$  filtering (see Fig. 3.2). The resulting horizontal position of fragments at the final focal plane with a fixed  $A/Z$  ratio only depends on their position at the middle focal plane and their spread is defined by the momentum spread  $\Delta p$  at S2.

$$X_{S4}(p) = \left( \frac{\partial x}{\partial x} \right)_{S2-S4} + \left( \frac{\partial x}{\partial(\delta p)} \right)_{S2-S4} \frac{\Delta p}{p}. \quad (3.7)$$

The quantity,  $(\partial x/\partial x)_{S2-S4}$  stands for the magnification ( $M_{S2-S4}$ ) in the position of fragments while going from S2 to S4 and  $(\partial x/\partial(\delta p))_{S2-S4}$  is the horizontal dispersion at S4 as a result of the momentum spread at S2. This achromatic mode produces spatially focused beams at the final plane

as shown in Fig. 3.4(top panel). This technique finds its application in cases where well focused secondary beam is required at S4, for example, in the Coulomb scattering experiments involving small area secondary targets.

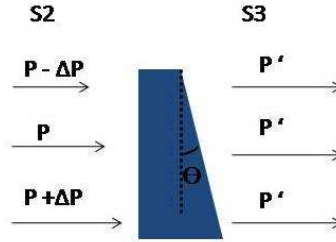


*Figure 3.3:* Effect of the angle  $\theta$  of degrader wedges on the momenta of the fragments for a monochromatic degrader. The fragments have a sharp energy at S4 after the second  $B\rho$  filtering.

In monochromatic setting the angle of the disk is arranged in such a manner that the momentum dispersion before the degrader is canceled at its exit for a given  $Z$  (see Fig. 3.3). As a result, a sharp energy of the secondary beam is achieved. This unique property of the monochromatic setting makes it suitable for the  $\beta^-$  decay experiments in which the maximum number of fragments are required to stop in a thin Si active stopper [43].

The momentum change introduced by the degrader at S2 is analysed by second  $B\rho$  selection stage to transmit a subset of nuclei with constant  $A/Z$  ratio.

**Second  $B\rho$  filtering:** The final selection and focusing is done with the same principle as in first  $B\rho$  selection. After the fourth dipole, achromatic mode minimizes the spatial spread of the ions, whereas monochromatic mode reduces the momentum uncertainty on the expense of large horizontal spread as shown in Fig. 3.4.

### 3.5 Identification of the ions: Principle and the equipment

To identify the selected reaction residues in terms of their atomic masses ( $A$ ) and atomic numbers ( $Z$ ), the FRS has two sets of detectors placed at the middle (S2) and final focal planes (S4). A schematic diagram of the FRS with its identification detectors is demonstrated in Fig. 3.5. At the middle focal

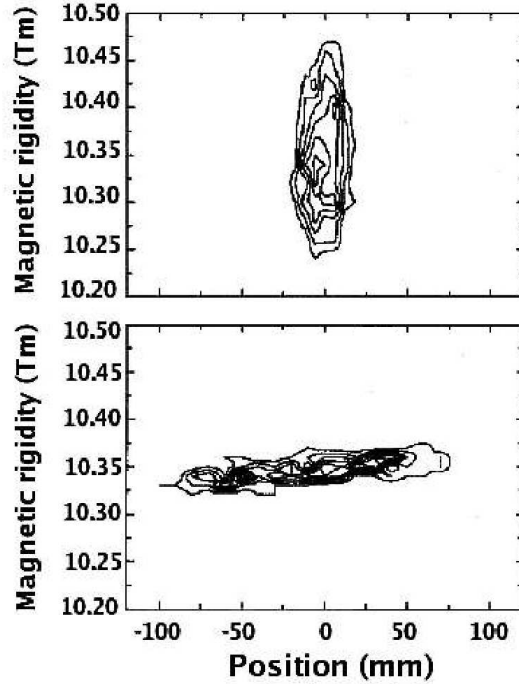


Figure 3.4: An example of the  $B\rho$ - $X_{S4}$  phase-space of a fragment beam of  $^{36}\text{P}$  produced by the fragmentation of a 1000 MeV/u  $^{40}\text{Ar}$  primary beam. The top panel represents the focusing of fragments using an achromatic degrader and the bottom panel corresponds to the monochromatic setting. The figure is taken from Ref. [31].

plane of FRS, SC21 gives the position coordinates of the ions and at the exit of the spectrometer this information is provided by two multi-wire proportional chambers MW41 and MW42. Time-of-flight between SC21 at S2 and SC41 at S4 determines the velocity of the beam particles. Reconstruction of the ion trajectories from S2 and S4 is done via the position information at the two foci. For a complete identification,  $Z$  of the fragments is provided by the energy loss measurement in two multi-sampling ionizations chambers MUSIC41 and MUSIC42 placed at the final focal plane. The procedure to determine the  $Z$  and  $A/Z$  ratio of the ions is described below and the working principle of particle detectors involved are explained along with.

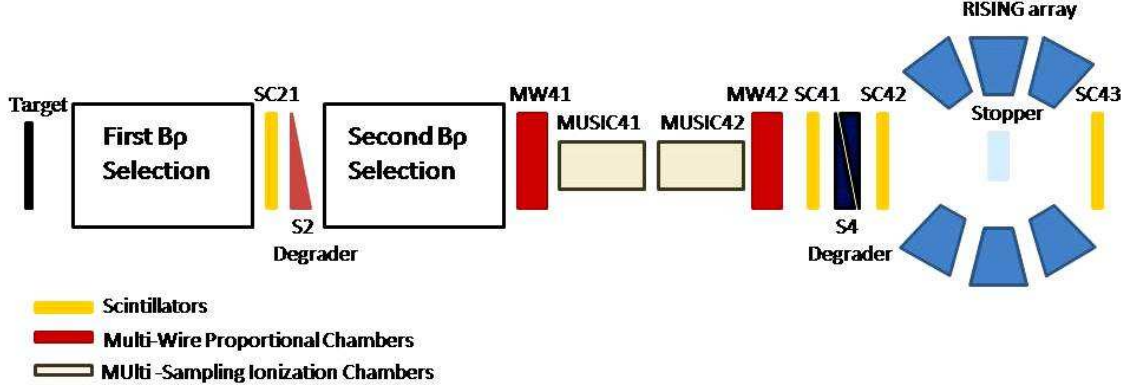


Figure 3.5: Fragment separator with its particle identification detectors at S2 and S4.

### 3.5.1 $A/Z$ determination

According to eq. (3.5), determination of the  $A/Z$  ratio of the fully stripped ions requires two quantities,  $B\rho$  and the velocity  $\beta$ .

#### 3.5.1.1 $B\rho$ measurement

The magnetic field strength  $B$  in which the fragments are moving is manually set for the four dipoles to allow a particular isotope of a nucleus follow the central trajectory. Due to dispersion in their momenta, fragments tend to deviate from the trajectory obtained from eq. (3.5). Defining the theoretically obtained trajectory as  $\rho_0$ , the effective trajectory traversed by the fragments in first two dipoles is computed from the relation

$$\rho = \rho_0 \left( 1 + \frac{X_2}{D_{TA-S2}} \right), \quad (3.8)$$

and in the third and fourth dipoles as

$$\rho = \rho_0 \left( 1 + \frac{X_4 - M_{S2-S4}X_2}{D_{S2-S4}} \right), \quad (3.9)$$

with  $M_{S2-S4}$  and  $D_{S2-S4}$  being the magnification and dispersion coefficients from S2 to S4 and  $X_4$  and  $X_2$ , the horizontal positions at the two focal planes. Therefore, to extract the effective trajectory and the magnetic rigidity, spatial coordinates of the fragments at the two foci of the FRS are required. At S4, this information is provided by two Multi-Wire Proportional Chambers MW41 and MW42, while a scintillator detector SC21 is used to give the position at the middle focal plane.

**Multi-Wire Proportional Chambers:** Multi-Wire chambers at FRS [44] are the classical parallel-plate proportional counters with two stage amplification. Interactions of the beam with the fill-gas ( $\text{CO}_2/\text{Argon}$ ) atoms in the chamber knock out primary electrons. These electrons are then multiplied due to their collisions with the gas atoms while drifting in an applied electric field. In multi-wire chambers used for the experiment the first stage amplification takes place in the gap between the grids  $U_G$  and  $U_T$ . Finally, an avalanche is created in the vicinity of anode grid  $U_A$ . Meanwhile, the movement of positively charged ions towards the cathode plane localizes the point of interaction of the beam in the chamber, hence providing its spatial coordinates. The multi-wire counters MW41 and MW42 stationed at the final focal plane are equipped with two perpendicular cathode planes to give both horizontal and vertical coordinates of interaction. Readout of the cathode wires consists of delay lines as displayed in Fig. 3.6. Each wire in X and Y direction corresponds to a delay of 4 ns. Signals from the two ends of delay lines were fed to a time-to-digital converter (TDC). Start of the TDC module is provided by anode signal and stop by the delay line output. Difference in arrival times of the signals traveling to the opposite sides of delay lines were calibrated to give position information in millimeters. The method to calibrate the detectors will be explained in section 3.6.1.

**Scintillators:** The three scintillators, SC21, SC41 and SC42 used in the experiment are fast plastic detectors of thickness ranging from 3-3.2 mm and an active area of around 200 mm $\times$ 80 mm [45]. The light output from the scintillators is collected by two photomultiplier tubes (PMTs) from Hamamatsu (HM2431) mounted on the two horizontal ends of the detectors. For position measurement an electronic circuit resembling Fig. 3.7 was implemented. Outputs from the two PMTs were fed to constant-fraction discriminator (CFD) and then to time-to-amplitude converter (TAC) with one of them giving the start for the measurement while the other providing the stop. Time difference of the start and stop signals defines the amplitude of the output of TAC, which was calibrated to convert the information into time units (ns). The horizontal position of ions impinging on the plastic material was extracted from these time differences during the calibration of multi-wire detectors to yield the coefficients converting time units into spatial units.

### 3.5.1.2 $\beta$ determination

To measure the velocity of the fragments, time-of-flight (TOF) measurement between two fast scintillators, SC21 and SC41 (see Fig. 3.7) stationed at S2 and S4 (see Fig. 3.5) was performed. The two scintillators were sepa-

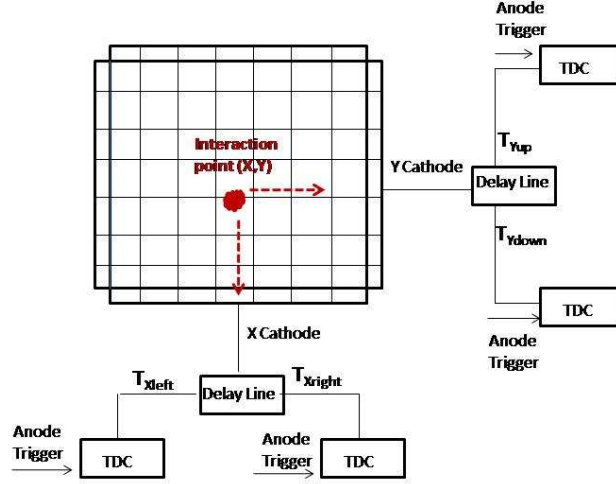


Figure 3.6: Readout of the cathodes of multi-wires giving position coordinates of the beam.

rated by a distance of 35 m. The time signals from SC21 and SC41 referred in text as  $T_{SC21}$  and  $T_{SC41}$ , respectively were fed to TAC after pre-processing (see Fig. 3.7). Since the trigger to enable the data acquisition and to the TAC measuring TOF was provided by SC41, the delaying of  $T_{SC21}$  with respect to  $T_{SC41}$  is necessary to ensure that it arrives later than the time signal from SC41. This delay,  $dT$  was chosen so to cover the finite range of TAC such that

$$T_{SC41} < dT + T_{SC21}. \quad (3.10)$$

In theory, the time-of-flight is the ratio of distance,  $d_o$  between the two scintillators and the velocity,  $v$  of the traveling ions

$$TOF = \frac{d_o}{v}. \quad (3.11)$$

Experimentally, TOF can be obtained by the difference in arrival of time signals from SC41 and SC21 as

$$TOF = T_{SC41} - T_{SC21}. \quad (3.12)$$

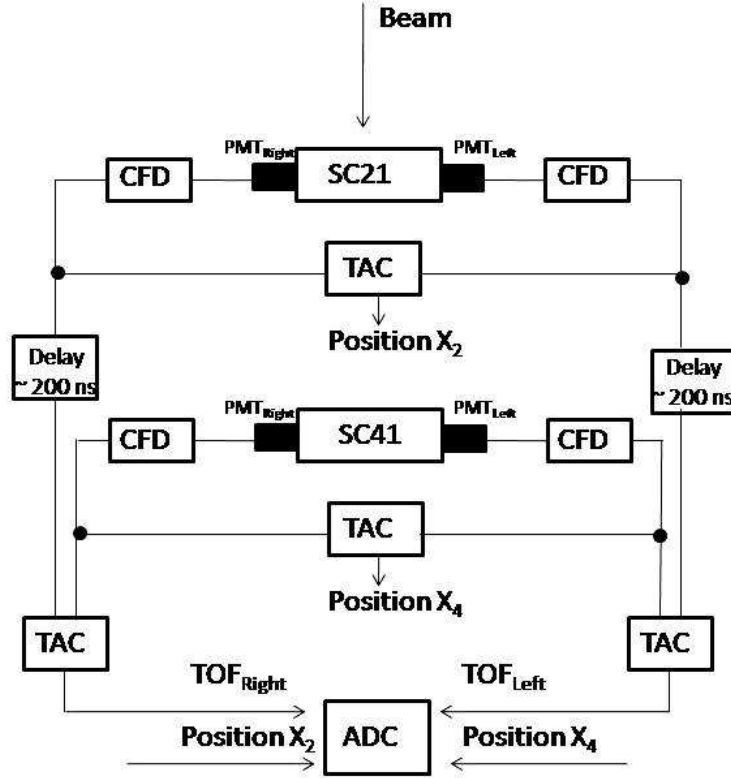


Figure 3.7: Readout of the scintillator detectors giving position coordinates of the beam and for the TOF measurement.

However, the measured TOF due to an extra delay added to  $T_{SC21}$  is

$$TOF_m = T_{SC21} + dT - T_{SC41}. \quad (3.13)$$

which can be expressed in terms of real TOF as

$$TOF = dT - TOF_m. \quad (3.14)$$

In terms of velocity eq. (3.14) can be reformulated to

$$\frac{1}{v} = \frac{dT}{d_o} - \frac{TOF_m}{d_o}, \quad (3.15)$$

$$\frac{d_o}{c} = \beta dT - \beta TOF_m. \quad (3.16)$$

$$\beta = \frac{d_o/c}{dT - TOF_m}. \quad (3.17)$$

Eq. (3.17) shows that the velocity of fragments follows a linear relationship with the measured  $\text{TOF}_m$ . The coefficients  $dT$  and  $d_o/c$  were extracted in the calibration process using a primary beam, details of which are given in section 3.6.3. The two photomultipliers attached to both sides of the scintillator detectors provided redundant TOF values as  $\text{TOF}_{Left}$  and  $\text{TOF}_{Right}$ . To cancel out the discrepancies in TOF measurements due to the deviation of ions from the central optical axis,  $\text{TOF}_{Left}$  and  $\text{TOF}_{Right}$  were averaged out.

### 3.5.2 $Z$ identification

According to Bethe Bloch formula the differential energy loss of an ion with an atomic number  $Z$ , traveling with relativistic velocities in matter is given by the relation

$$-\frac{dE}{dx} = \frac{4\pi}{m_e c^2} \frac{Z' Z^2 N_a \rho}{A' \beta^2} \left( \frac{e^2}{4\pi \epsilon_0} \right) \left[ \ln \left( \frac{2m_e c^2 \beta^2}{I(1 - \beta^2)} \right) - \beta^2 \right]. \quad (3.18)$$

In this formula,  $m_e$  represents the mass of electron,  $Z'$ ,  $A'$ ,  $\rho$  and  $I$  are atomic number, atomic mass, density and average excitation potential of the absorbing material and  $N_a$  is the Avogadro's number.

In simpler terms, the relation between stopping power of the absorber material and  $Z$  of the ions can be expressed as

$$-\frac{dE}{dx} = Z^2 f(\beta), \quad (3.19)$$

where  $f(\beta)$  is a function of velocity of impinging ions. Therefore, to obtain  $Z$ ,  $dE/dx$  and  $f(\beta)$  in a given material are needed to be quantified which is discussed in the following sections.

#### 3.5.2.1 $\Delta E$ measurement

The two Multi-Sampling Ionization Chambers (MUSICs) placed at S4 [46] provided the energy loss value of the ions passing through them.

**MULTI-Sampling Ionization Chambers (MUSICs):** The ionization chambers are called as multi sampling because of their principle of operation. Beam particles produce secondary electrons in the ionization of  $\text{CF}_4$  gas at atmospheric pressure. The number of secondary electrons created is proportional to the energy deposited by beam particles in the chamber. These

electrons are collected by the anode, which is divided into eight independently read strips. The signal from each anode strip form the input of fast pre-amplifier, the output of which was fed to the analog-to-digital converter (ADC). A schematic layout of the readout logic of MUSICs is shown in Fig. 3.8. The eight samples were averaged out geometrically to give total loss of energy in the chamber.

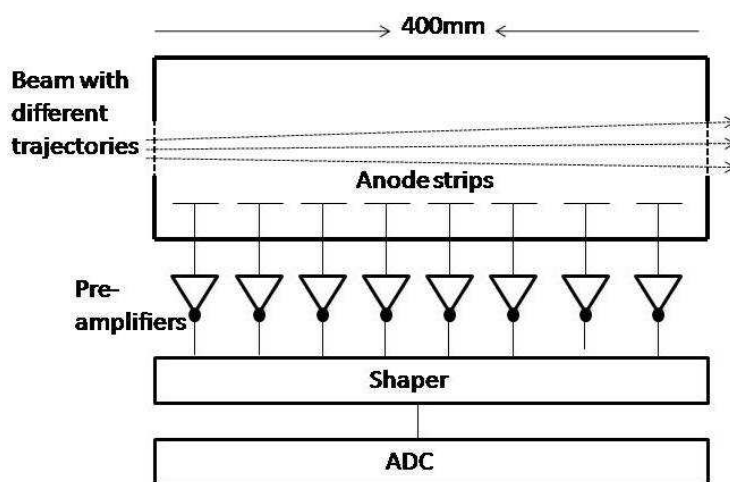


Figure 3.8: Readout electronics for eight anode strips of MUSICs.

$$\Delta E = \sqrt[8]{\Delta E_1 \dots \Delta E_8}. \quad (3.20)$$

Beam particles following different trajectories lose slightly different energies in the chamber, which gives a position subjectivity and deteriorates the resolution of the MUSICs. The dependence of energy loss on the horizontal position of fragments impinging on the ionization chambers is illustrated in Fig. 3.9(a). To cancel this effect, a correction with a fourth order polynomial was applied. To extract this correction function the whole area of the MUSIC detectors was illuminated by sweeping the primary beam in X direction. This was done by gradually changing the magnetic field of the last dipole D4. The corrected  $\Delta E$  as a function of tracked position of the beam, provided by MW41 or MW42 is plotted in Fig. 3.9(b).

The energy loss also varies with the velocity of beam particles. To determine this velocity dependence, primary beam was degraded to different energies by inserting different matter thickness in its path. Energy loss in the two MUSICs as a function of velocity of the primary beam ( $\beta_p$ ) ranging

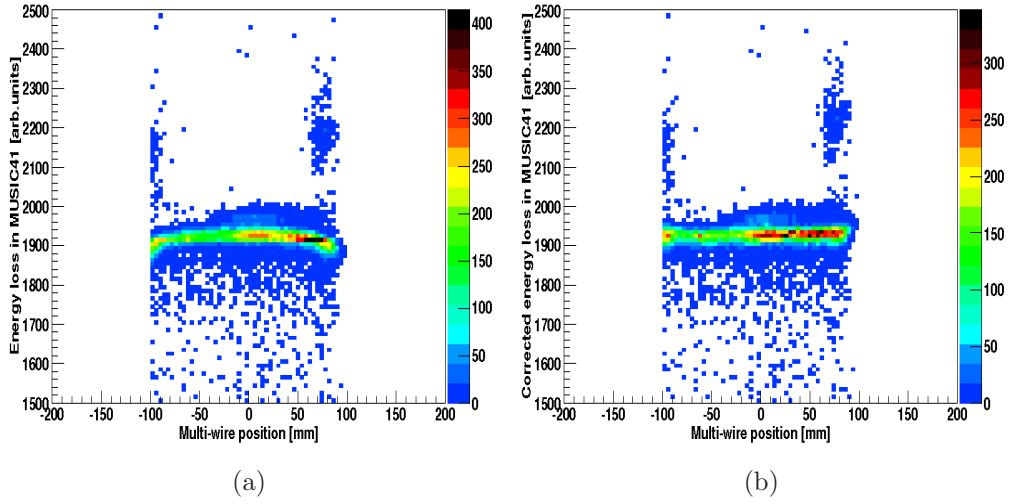


Figure 3.9: (a): Energy loss in MUSIC41 as a function of multi-wire MW41 position in X direction. The curve has some distortions at the ends which are needed to be corrected for good Z resolution. (b): The corrected curve for energy loss to remove the position dependence.

between 0.63-0.76 was plotted. The curve shown in Fig. 3.10 was fitted to a second order polynomial to express the energy loss in MUSICs as

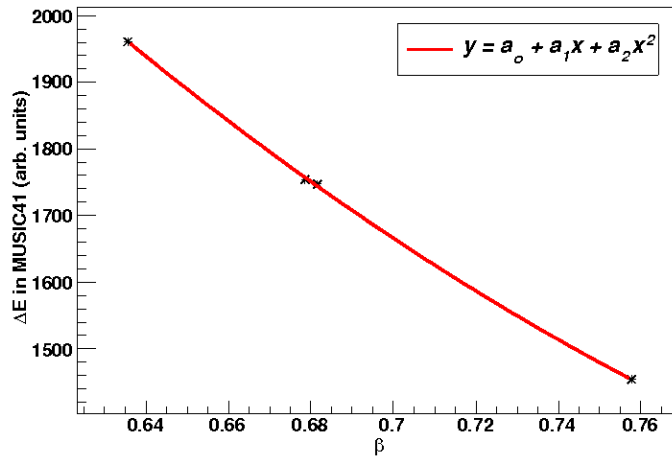


Figure 3.10:  $\Delta E_p$  as a function of  $\beta_p$ . Fit of the curve is shown in red.

$$\Delta E_p = a_0 + a_1\beta_p + a_2\beta_p^2, \quad (3.21)$$

where  $a_0$ ,  $a_1$  and  $a_2$  are the resulting coefficients. This measurement was done for a range of primary beam velocities covering the velocities of the fragments as well. Hence, the coefficients,  $a_0$ ,  $a_1$  and  $a_2$  in eq. (3.21) can be used to define the relation between energy loss of the fragments with their velocities. A normalization to the known atomic number,  $Z_p$  of primary beam can then be used to obtain  $Z_f$  of the fragments as explained in section 3.6.2.

## 3.6 Calibration of the FRS detectors

To obtain the  $Z$  and  $A/Z$  ratio of the fragments in absolute units, calibration of particle detectors used for identification is necessary. In the following sections, the procedures to calibrate the MUSIC, MWPC and scintillator detectors are described.

### 3.6.1 Multi-wire proportional chamber calibration

The spatial coordinates of the point of interaction of ions in both of the MWPCs are given as

$$X = a_0 + b_0[T_{Xleft} - T_{Xright}], \quad (3.22)$$

$$Y = a_1 + b_1[T_{Yup} - T_{Ydown}], \quad (3.23)$$

where  $T_{Xleft}$ ,  $T_{Xright}$ ,  $T_{Yup}$ ,  $T_{Ydown}$  are the time signals from the two ends of the delay lines in X and Y direction respectively and  $a_0$ ,  $a_1$ ,  $b_0$ ,  $b_1$  are the calibration coefficients.  $b_0$  and  $b_1$  are the factors transforming nanoseconds to millimeters and are given by the delay line readout of cathodes. For two wires separated by a distance of 2 mm, a delay of 4 ns was measured, which determines the required conversion factors  $b_0$  and  $b_1$ . To measure the offsets  $a_0$  and  $a_1$ , the slits mounted after the multi-wire chambers at S4 were opened very narrow, allowing only a well focused beam to pass through. By comparing the slit positions to the beam position shown by multi-wire detectors, these offsets were set.

### 3.6.2 MUSIC calibration

Ionization chambers were calibrated to give  $Z_f$  of the fragments from the measured energy loss  $\Delta E_f$ . As in expression (3.19),  $f(\beta)$  solely depends

on the velocity of traversing ions, it is similar for both primary beam and the fragments. Therefore, for a primary beam with atomic number,  $Z_p$  and differential energy loss,  $dE_p/dx$  the following relation holds

$$-\frac{dE_f}{dx}(\beta) = -\frac{Z_f^2}{Z_p^2} \frac{dE_p}{dx}(\beta). \quad (3.24)$$

Using eq. (3.21),  $Z_f$  can be deduced as

$$Z_f = Z_p \sqrt{\frac{\Delta E_f}{a_0 + a_1\beta + a_2\beta^2 + a_3\beta^3}}. \quad (3.25)$$

$\Delta E_f$ , here is corrected for the position dependence as explained in section 3.5.2.1.

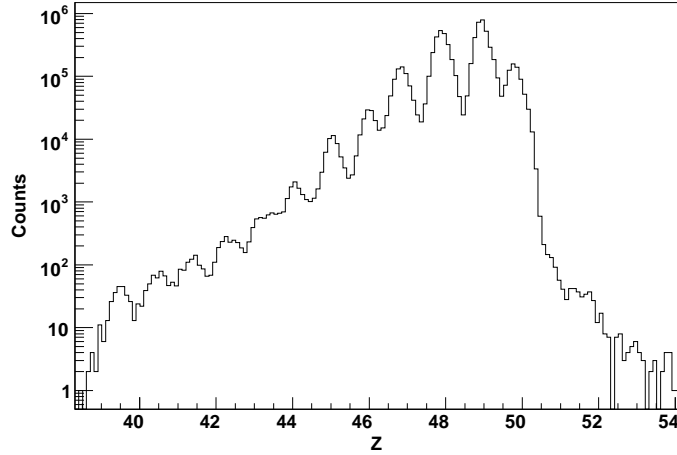


Figure 3.11:  $Z$  deduced from the energy loss information in MUSIC41 and calibrated using a reference  $^{136}\text{Xe}$  primary beam.

### 3.6.3 Scintillator calibration

The scintillator detectors measure the position of traversing ions and provide their TOF information, therefore they were calibrated for both set of measurements.

1. *Position calibration*

The primary beam was defocused to cover the whole active area of the scintillator at S2. The correlation between time difference between the signals from two ends of SC21 and the position coordinates from multi-wire is demonstrated in Fig. 3.12.

The correlation function is a first order polynomial written as

$$X = a_0 + a_1 T_{SC21}. \quad (3.26)$$

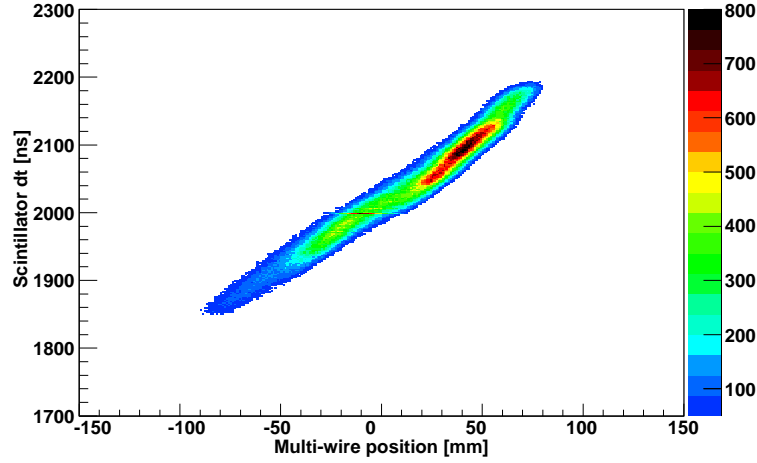


Figure 3.12: The correlation between difference in time signals  $dt$  from two ends of SC21 and the position in multi-wire MW21.

The fit of this correlation gives the calibration coefficients  $a_0$  and  $a_1$ . The MWPC at S2 were only inserted during the calibration of SC21 for position.

## 2. $\beta$ calibration

Velocity,  $\beta_f$  of the fragments can be obtained from eq. (3.17), provided, the factors  $dT$  and  $d_o/c$  are known. These numbers are acquired by plotting the product of  $\beta_p TOF_m$  as a function of  $\beta_p$ . Here,  $\beta_p$  is the velocity of primary beam calculated using the following expressions

$$E = mc^2 = \gamma m_0 c^2 \approx T + m_0 c^2. \quad (3.27)$$

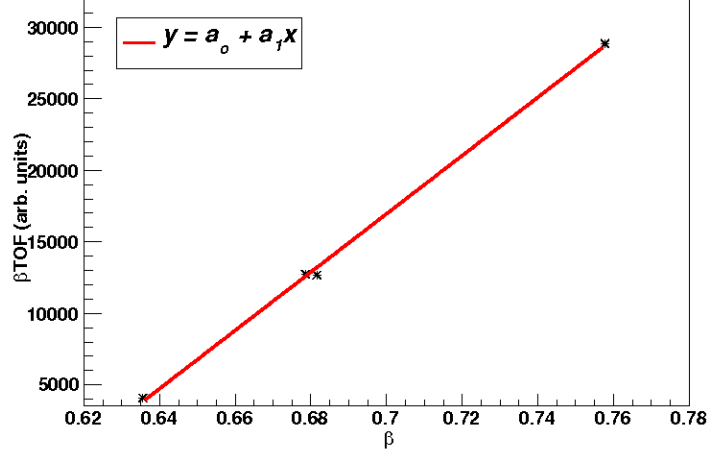


Figure 3.13: The product of primary beam velocity  $\beta_p$  and measured  $TOF_m$  versus  $\beta_p$ .

In the above equation,  $T$  is the kinetic energy of the beam in  $MeV/u$ . The relativistic factor,  $\gamma$  can be extracted from the above expression as

$$\gamma \approx 1 + \frac{T}{m_0 c^2} = 1 + \frac{T}{A.931.5}. \quad (3.28)$$

where  $A$  is the atomic mass of the beam particles and all the quantities are in lab frame of reference. Using the relation between  $\gamma$  and the velocity,  $\beta$ , one obtains the velocity of primary beam as

$$\beta_p = \frac{1}{[1 + T/(A.931.5)]} \sqrt{\left(\frac{T}{A.931.5}\right)^2 + 2 \times \left(\frac{T}{A.931.5}\right)}. \quad (3.29)$$

Summarizing, the ions traveling through the FRS are selected exploiting the  $B\rho-\Delta E-B\rho$  method. At the middle focal plane of FRS, SC21 gives the position coordinates of the ions and at the exit of the spectrometer this information is provided by two multi-wire proportional chambers MW41 and MW42. Time-of-flight between SC21 at S2 and SC41 at S4 determines the velocity of the beam particles. Reconstruction of the ion trajectories from S2 to S4 is done via the position information at the two foci. Finally, the  $A/Z$  ratio of fully stripped ions is calculated by combining eq. (3.5) and (3.9) as

$$\frac{A}{Z} = \frac{B\rho_0}{u\beta\gamma c} \left( 1 - \frac{X_4 - M_{S2-S4}X_2}{D_{S2-S4}} \right). \quad (3.30)$$

For a complete identification,  $Z$  of the fragments is provided by the energy loss measurement in two multi-sampling ionizations chambers MUSIC41 and MUSIC42 placed at the final focal plane.

The logical GATE signal enabling the digital electronics of FRS detectors to write data, namely TDCs for multi-wires and ADCs for scintillators and MUSICs were taken from the delayed timing signal of SC41 placed at the exit of the FRS. An example identification plot for the Cd isotopes along with its neighbouring nuclei produced in the FRS setting centered on  $^{130}\text{Cd}$  is shown in Fig. 3.14.

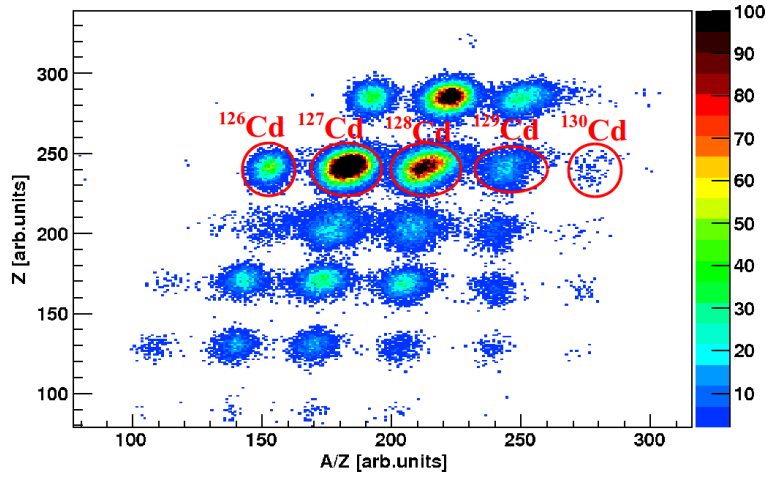


Figure 3.14: The  $Z$  versus  $A/Z$  identification plot for fragments produced in the experiment.

Once the identification of the fragments was done, they were slowed down in an Aluminum degrader and then stopped in a passive stopper surrounded by the RISING array [13] to do the gamma-ray spectroscopy.

### 3.7 Implantation of the ions

The energy of the fragments reaching the final focal plane was around  $\sim 400$  MeV/u. For isomeric decay spectroscopy these relativistic ions were stopped in a passive catcher surrounded by the RISING array. At this energy, a thick stopper is required to ensure maximum implantations. Drawback of implanting the fragments in a large volume of matter is that the  $\gamma$  radiations

emitted by the isomeric states get absorbed in the material itself, thereby reducing the detection efficiency of the  $\gamma$  detectors. To overcome this limitation, fragments were slowed down in a thick Al degrader prior to the implantation. A thin catcher of few mm thickness made of plexi-glass was then used to implant the ions.

To assure that the maximum number of ions of interest stop in the plastic catcher, thickness of the degrader placed before it to slow down the ions was calibrated. This thickness was varied until no counts were observed in scintillator detector SC43 mounted after the catcher (see Fig. 3.5). The curve representing the variation of number of counts in the scintillator as a function of thickness of degrader is shown in Fig. 3.15. This procedure was performed only once with the primary beam. The thickness of degrader when SC43 didn't register any counts was considered suitable for stopping the ions in the catcher. The calibration done in this way gives only an estimate that the ions are stopped somewhere in the stopper but in the cases where exact implantation position is required, a careful calibration is needed. For example, in the experiments involving  $\beta^-$  decay studies with an active stopper [43], the degrader calibration is done considering the count rates in individual layers of the Si array along with in SC43, thus giving an exact position of implantation. The desired situation in these cases is when the implantations take place mostly in the middle layer of Si array.

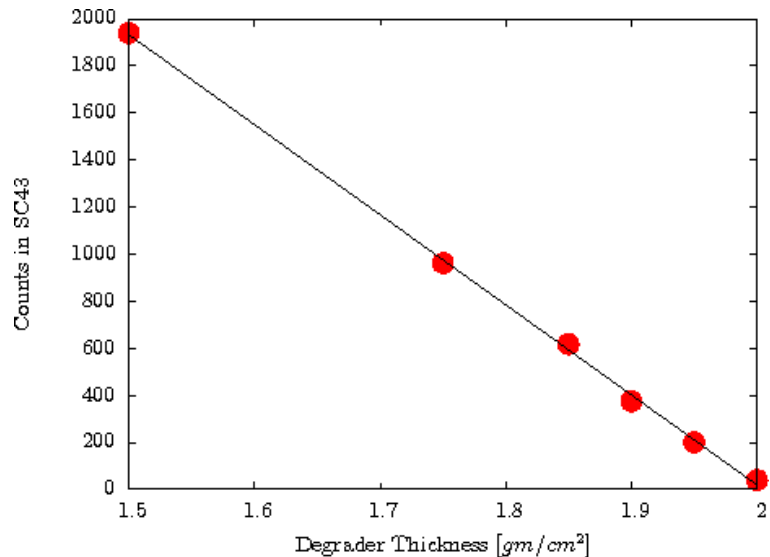


Figure 3.15: The variation in count rate in scintillator SC43 as the thickness of S4 degrader increases. The value for stopping ions in the catcher corresponds to  $\sim 2 \text{ g/cm}^2$  in this case.

Slowing down of fragments in a thick degrader led to a considerable loss of beam particles due to nuclear reactions. The products of nuclear interactions are unwanted contaminants which are removed from the data during off-line analysis. Details of the steps implemented to remove the nuclear reaction residues are explained in section 4.2. Gamma decays following the implantation were registered in the RISING Ge array. The following sections deal with the technical details and readout electronics of the array.

### 3.8 The RISING cluster array

A total number of 105 high purity hexagonal Ge crystals constitute the high efficiency RISING array.



Figure 3.16: A schematic layout showing the arrangement of seven HPGe crystals in a common cryostat of a RISING cluster detector [47].

The interaction of gamma rays with the detector material form the basis of gamma-ray spectroscopy. Three mechanisms, photoelectric absorption, Compton scattering and pair-production are mainly responsible for the attenuation or complete absorption of the gamma rays of energy below 10 MeV in the detector. The amount of energy deposited by the gamma radiation in the detector depends on energy of the radiation and the geometry of the detector. A low energy gamma ray (up to 100 keV) can get fully absorbed via the photoelectric effect, whereas at higher energies the absorption mechanism is dominated by Compton scattering and pair production. In Compton scattering the  $\gamma$  ray strikes on an atomic electron, loses a part of its energy and gets scattered. The angle of scattering determines the amount of energy deposited in one interaction according to the expression

$$E' = \frac{E_o}{1 + \frac{E_o}{m_e c^2} (1 - \cos \theta)}, \quad (3.31)$$

where  $E'$  is the energy of the  $\gamma$  ray after scattering,  $E_o$  is the incoming  $\gamma$ -ray energy,  $m_e$  is the rest mass of the electron on which the gamma photon

strikes and  $\theta$  is the angle of scattering. Energy deposited in the interaction is then given as  $E_0 - E'$ .

The pair-production mechanism utilizes the energy of interacting  $\gamma$  ray for the production of an electron-positron pair. As the minimum energy required for an electron or a positron to exist is its rest mass energy, this mechanism only takes place for gamma energies above 1022 keV. The excess energy is given out as the kinetic energies of both the out coming particles. The positron gets annihilated by an atomic electron in the vicinity and produces two  $\gamma$  rays of 511 keV. This quanta of energy can get re-absorbed or can escape the detector volume giving rise to single or double escape events. Both Compton scattering and pair-production mechanisms lead to incomplete deposition of energy of the incoming  $\gamma$  ray in a single interaction. The full energy deposition of high energy gamma rays will involve multiple interactions within the detector volume. Since physical limitations restrict the construction of a large area semiconductor detector, an array of relatively small detectors read out with an energy add-back mode is efficient. Such arrays give a large effective detection volume leading to full absorption of the  $\gamma$  rays. A schematic layout of the *RISING* cluster detector consisting of seven Ge crystals mounted in a common cryostat is shown in Fig. 3.16. This set up allows to add back the energies of events scattered in the neighbouring crystals and to recover total absorption events. By this technique the Compton background is reduced considerably increasing the photopeak efficiency of the device. Description of the performed add-back analysis is given in section 4.3.2.

### 3.8.1 Technical details

In its stopped beam configuration the whole *RISING* array had a photopeak efficiency of 15% at 661 keV with the individual detectors arranged in three angular rings at  $51^\circ$ ,  $90^\circ$  and  $129^\circ$  respective to the beam axis. The average distance of each cluster to the beam tube was approximately 22 cm. The cluster electronics allowed to extract correlated energy and time information of the interaction of  $\gamma$  rays. To obtain the energy value, digital processing of one of the two outputs from the germanium pre-amplifier was done. This branch consisted of Digital Gamma Finder (DGF-4C) modules [48, 49], each having 4 input channels with an integrated 14-bit ADC to digitize the output signals from the pre-amplifiers. A slow trapezoidal filter, sampling the pulse outputted by the ADC was implemented. The trapezoidal transformation reduces pile-up of the signals and thus works well in high rate conditions. The second output from the pre-amplifier served as the timing signal and was fed both to the DGF modules and a standard analog TFA-CFD-TDC

circuit. In DGF, the time information was acquired when a fast trapezoidal fast filter crossed the manually set threshold, marking the moment of arrival of the  $\gamma$  rays. To get the value in absolute units the output from the fast filter was associated to an internal clock running with a time-step of 25 ns. The complete electronics system was enabled by a particle trigger provided by scintillator SC41. The arrival of this trigger opened a  $\gamma$ -acceptance window of 50  $\mu$ s. One of the inputs of DGF-time branch was also fed by the particle trigger to check the internal synchronization of all modules. The parallel analog branch also activated by the delayed particle trigger provided a second time evidence to that of DGF with two TDC modules, one with a short range of 1  $\mu$ s and a temporal resolution of 0.31 ns/ch and the other with a long range of up to 800  $\mu$ s and a 0.76 ns/ch resolution.

Coincidence between the implanted ions and the detected  $\gamma$  rays within a specified time range ensured an unambiguous assignment of the detected radiations to the decay of isomeric states of the nuclides.

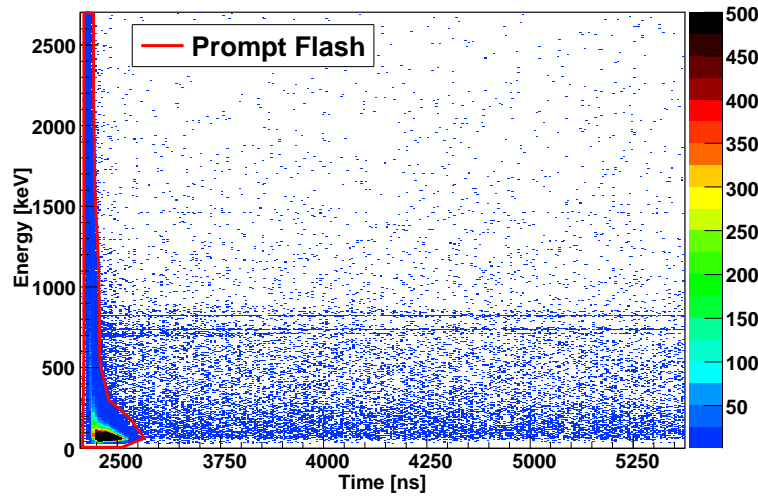


Figure 3.17: Energy versus time matrix for the  $\gamma$  rays associated with the isomeric decay of  $^{127}\text{Cd}$ . The spectrum shows “shoe-shaped” prompt flash produced due to stopping of beam in matter and the lines correlated with the time distribution of gamma rays depopulating an isomeric state.

An example of energy versus time matrix from the DGF modules for  $^{127}\text{Cd}$  isotope is shown in Fig. 3.17. A typical matrix obtained in the stopped beam geometry consists of two sets of structures which can be explained as follows:

1. Prompt flash: This arises when the beam particles with relativistic en-

ergies hit the stopper or the shielding materials upstream and ionize them. The electrons knocked out from the atoms in this process decelerate in the electromagnetic field of atomic nuclei in their vicinity. Energy of these electrons is released in the form of atomic radiation called bremsstrahlung. This prompt  $\gamma$  emission marks the time of implantation of ions in the stopper. The peculiar “shoe-shaped” structure at low energies is due to the response of Ge detectors. As a low-energy gamma ray cannot penetrate deep into the detector, it loses its energy mainly in the outer parts and thus the rise time of the pulse is mainly governed by the collection time of charge carriers drifting through the whole detector volume. On the other hand higher energy gamma rays can interact deeper and have faster rise times. Hence, a low-energy gamma ray has an electronic walk with respect to a high-energy radiation. This walk gives rise to the broadening of time spectra at low energies.

The presence of prompt high gamma flux prevents the Ge detectors from giving any valuable information about the isomeric decays for a short period of time after implantation. This inhibition limits the lifetimes of isomers that can be studied at the final focal plane in addition to the limitation due to the flight path of the FRS. The time distribution of prompt flash from the long-range TDC is shown in Fig. 3.18. A width of  $\approx 30$  ns was obtained for the energies above 500 keV. This finite width of prompt flash in time suggests that the isomers having half-lives less than 10 ns, surviving the flight path of FRS due to a hindered electronic conversion cannot be studied with this setup.

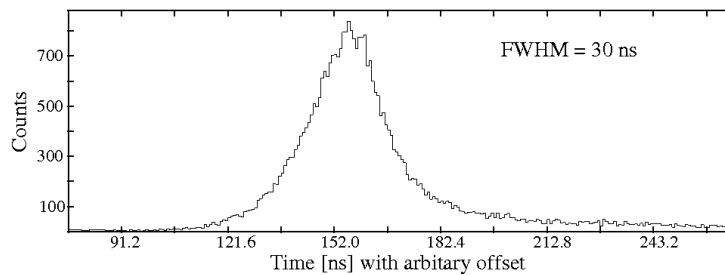


*Figure 3.18:* Width of the prompt flash in time, obtained with the long-range TDC. For details see the text.

By imposing a condition for the gamma transitions to lie outside the prompt flash region one can ensure a clean gamma spectrum. Corre-

sponding graphics showing the cleaning gate for separating  $\gamma$  transitions from the prompt flash is shown in Fig. 3.19.

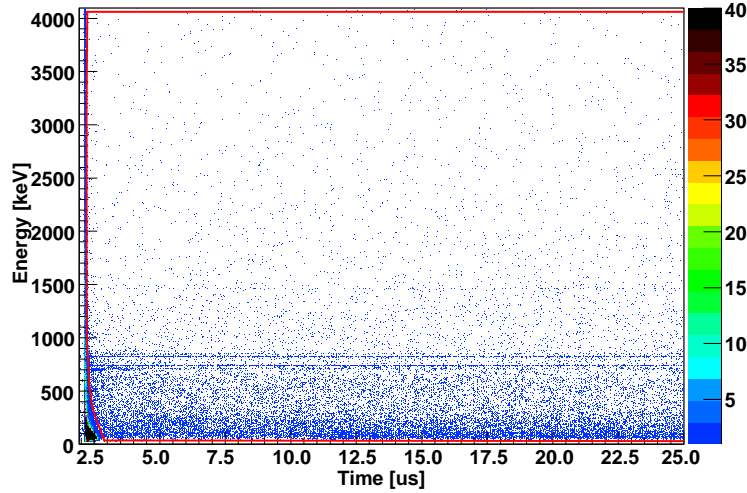


Figure 3.19: The energy versus time matrix of  $\gamma$  rays for an energy range of 50 keV to 4 MeV and a time window of 25  $\mu$ s after the ion implantation. The gate shown in red is the cleaning condition employed to separate out the prompt flash from real gamma transitions.

## 2. Gamma rays following the exponential decay law of radiation

$$I = I_0 e^{-\lambda t}, \quad (3.32)$$

where  $I_0$  is the intensity of the gamma ray at time = 0,  $\lambda$  is the decaying constant with

$$\lambda = \frac{\ln(2)}{T_{1/2}} \quad (3.33)$$

and  $t$  is the time after implantation. A uniform intensity of the gamma ray over the full time range indicates a half-life of decaying isomer much longer than the time window.

# Chapter 4

## Data Analysis

This chapter contains the methods of analysis implemented to study the isomeric  $\gamma$  decays in the  $^{127}\text{Cd}$ ,  $^{125}\text{Cd}$  and  $^{129}\text{Cd}$  isotopes. The performed analysis can be sub-divided into three main parts, namely:

- Off-line selection of the ions to be studied.  
The selection of the implanted Cd ions was achieved by confirming the  $Z = 48$  condition in  $\Delta E$  plot of two ionization chambers. Correlation between the position of arrival of the ions at the middle (S2) and the final focal planes (S4) of the FRS as a function of their mass-to-charge ratio ( $A/Z$ ) was checked in order to select a particular Cd isotope.
- Removal of contaminants produced due to the nuclear reactions of the beam ions in the layers of matter present in the beam line, thereby reducing the background in  $\gamma$ -ray spectra.
- Constructing the level schemes:  $\gamma$ -ray spectroscopy.  
This branch of analysis comprises of identifying the  $\gamma$  transitions originating from the decay of isomeric states in a nucleus followed by the assignment of observed  $\gamma$  transitions to the decaying levels based on  $\gamma\gamma$ -coincidence relations, intensity balance and the lifetime of the isomeric states.

### 4.1 Particle selection

During the experiment, a particle trigger discussed in section 3.8.1 facilitated the readout of only those  $\gamma$  rays in the RISING array which were in coincidence with the particles implanted in the stopper. To assign the observed gamma transitions unambiguously to the decay of an isomer in Cd isotopes, proper  $Z$  and  $A/Z$  of the ions were selected in the following manner.

- Selecting the  $Z$  of the nucleus.

Energy loss in one of the ionization chamber (MUSIC41) as a function of the energy loss in the other ionization chamber (MUSIC42) was plotted. The obtained spectrum is shown in Fig. 4.1. The  $Z$  selection for Cd isotopes is displayed.

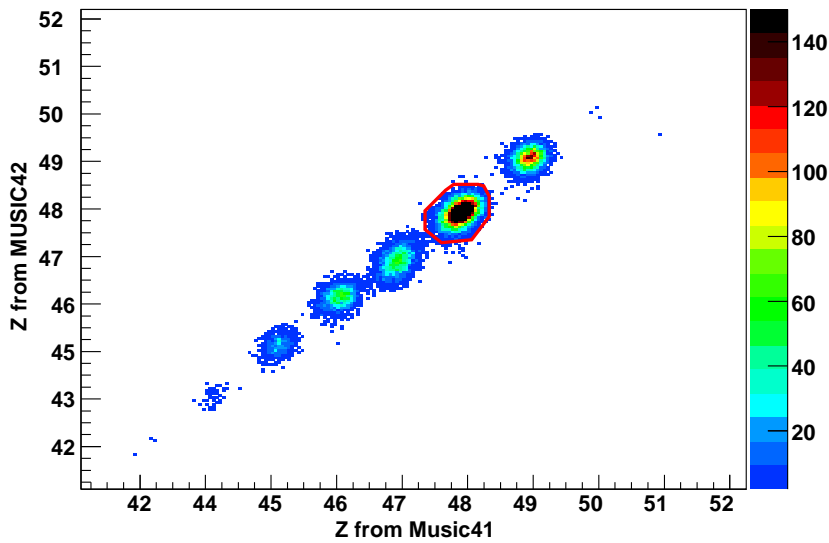


Figure 4.1: The  $Z$  information extracted from the two ionization chambers placed at S4. The condition shown in red selects Cd isotopes with  $Z = 48$ .

- Correlating the position of the fragments at S2 and their  $A/Z$  ratio.  
After the selection of the atomic number  $Z$ , a correlation between position of arrival of the ions at S2 and their  $A/Z$  ratio was investigated. The result for the Cd isotopes is illustrated in Fig. 4.2. By requiring a condition for  $A/Z$  ratio to lie within the shown gate  $^{127}\text{Cd}$  was selected.
- Correlating the position of the fragments at S4 and their  $A/Z$  ratio.  
Similar analysis as mentioned for the S2 position was done for the position of the ions at S4. The results are shown in Fig. 4.3. Selection condition for  $^{127}\text{Cd}$  is highlighted.

## 4.2 Removal of contaminants

Nuclear reactions of the beam particles in the matter placed at S2 and S4 give rise to unwanted contaminants and hence increase the background in

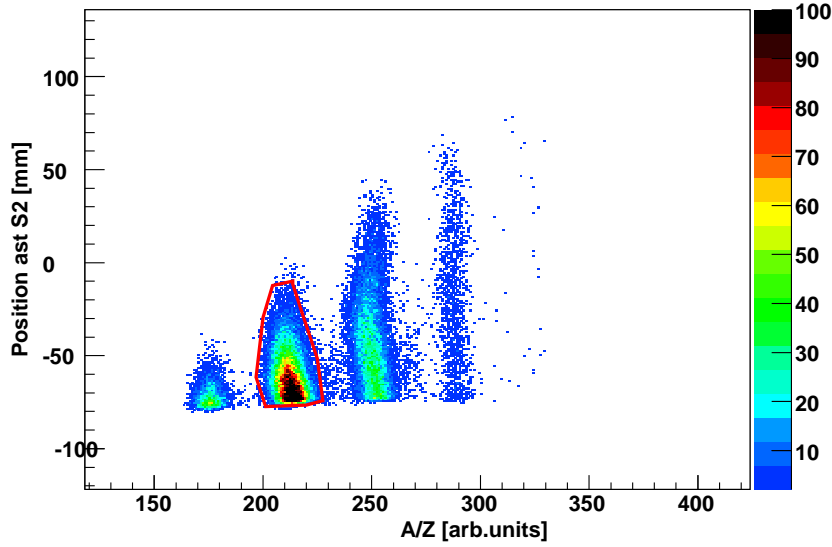


Figure 4.2: Position of the fragments at S2 with  $Z = 48$  as a function of their  $A/Z$  ratio. The condition implemented to select the  $^{127}\text{Cd}$  isotope is shown.

the resulting gamma spectra. At S4, main source of background comes from the slowing down of secondary fragments in a thick degrader. The products of these secondary reactions have different  $Z$  than that of the incoming fragments and thus can be differentiated in the energy loss spectrum of the beam before and after slowing down. The  $\Delta E$  in MUSIC41 mounted before the degrader is plotted against the  $\Delta E$  in SC42 placed after the degrader in Fig. 4.4. The fragments undergoing nuclear reactions are visible in the form of a tail. Only the events inside the selection, the ones which did not react in the degrader and did not change their  $Z$ , were further analysed.

### 4.3 Gamma-ray spectroscopy

After the clean identification and selection of the particles, the energy and time information of  $\gamma$  radiations associated with the decay of a selected isotope was processed. The required condition to see gamma transitions associated with the decay of isomers in the RISING cluster detectors is that the isomers populated at the target should have lifetimes long enough to be able to reach the final focal plane of FRS and they should be stopped in the catcher.

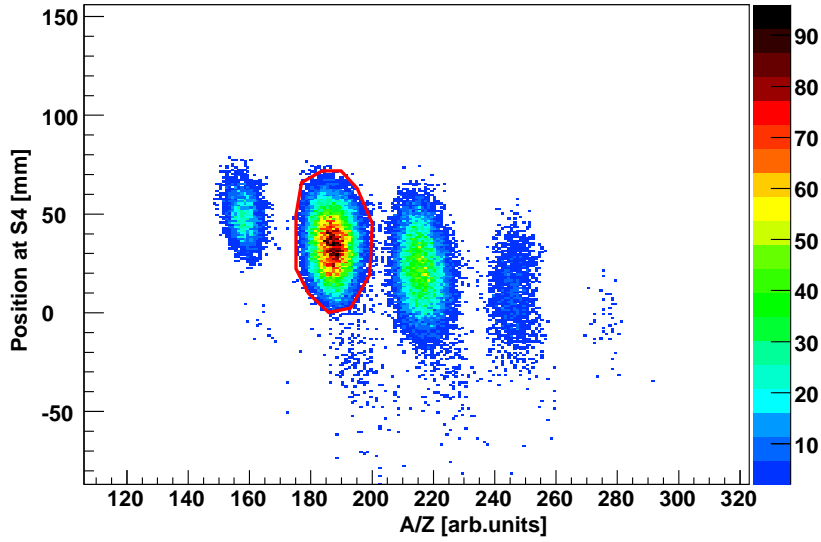


Figure 4.3: Horizontal position of the Cd isotopes at S4.  $^{127}\text{Cd}$  is selected by choosing the corresponding  $A/Z$  ratio.

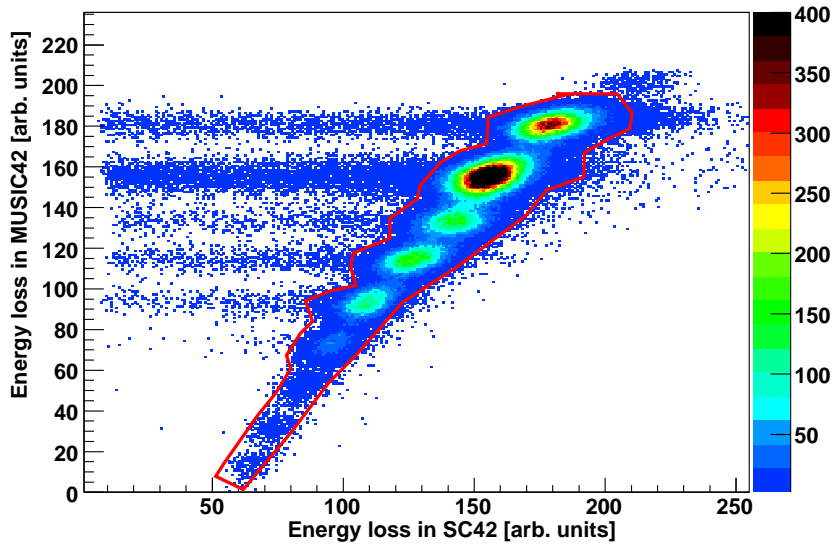


Figure 4.4: The selection done on the energy loss of the fragments in SC42 and MUSIC42. Fragments reacted in the degrader show a different energy loss in SC42 in comparison to that of MUSIC42 and thus, can be eliminated.

### 4.3.1 Energy calibration

To calibrate the  $\gamma$ -ray energy spectra, standard calibration sources of  $^{152}\text{Eu}$ ,  $^{60}\text{Co}$  and  $^{133}\text{Ba}$  covering the range of 60 keV to 1.33 MeV were used. By default 1 keV/ch calibration is sufficient but in the present case 0.25 keV/ch calibration was done because of the expected doublets at low energy for  $^{125}\text{Cd}$ . In Fig. 4.5 the factor gained when going from 1 keV/ch to 0.25 keV/ch to resolve the doublets present at energies 198.4 keV and 202.4 keV in  $^{126}\text{In}$  (experimental data) and 1085.8 keV and 1089.7 keV in  $^{152}\text{Eu}$  (calibration source) is shown.

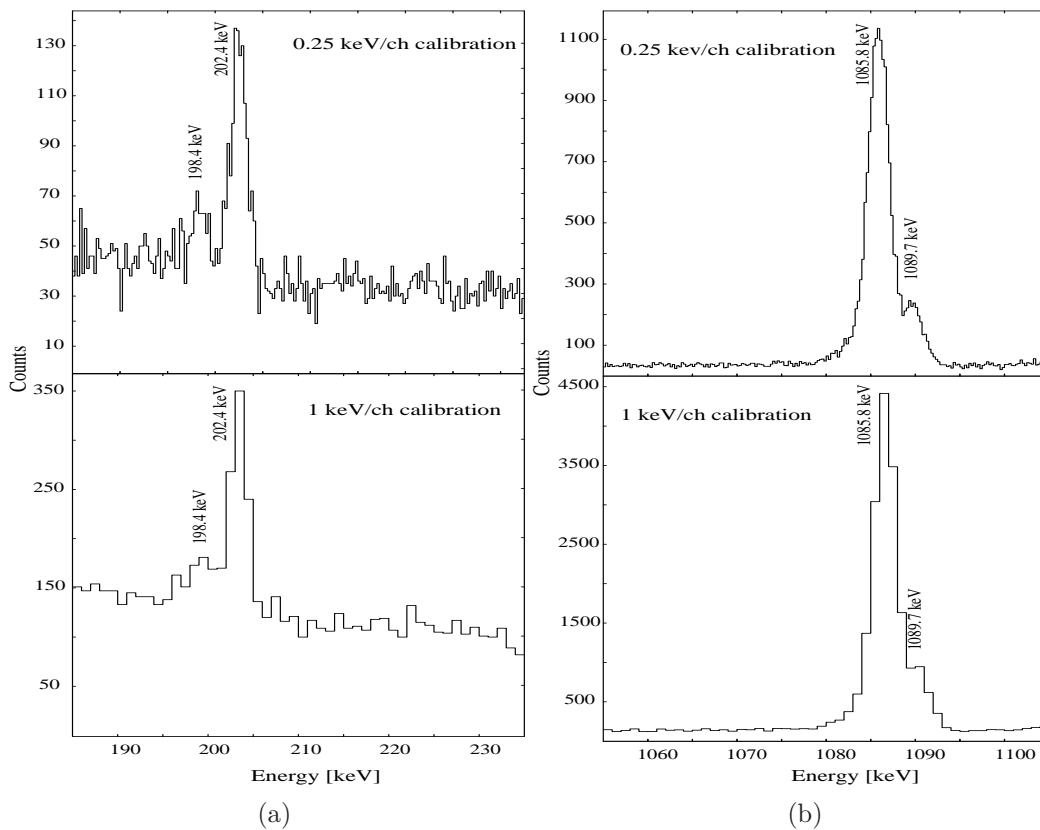


Figure 4.5: Left: The calibrated gamma spectrum of  $^{126}\text{In}$  for lower energies with 1 keV/ch and 0.25 keV/ch calibration factors. Right:  $^{152}\text{Eu}$  energy spectrum. The 0.25 keV/ch improves the resolution of doublets present at energies 1085.8 keV and 1089.7 keV considerably.

### 4.3.2 Add-back principle

To reduce the Compton continuum originating from the incomplete absorption of incoming  $\gamma$  rays scattered in the detector, many approaches can be adopted, for example optimizing the thickness and geometry of the detector volume allowing multiple scattering and hence total absorption or using anti-coincidence mode with an active shield etc. In an array like RISING, the geometry of a crystal is optimized to ensure maximum absorption of the gamma rays. Nevertheless, Compton scattering dominates the absorption process and to recover the full energy of the interacting gamma ray adding back of the energies deposited in different crystals is necessary. In the following section conditions for the  $\gamma$  rays to be considered for add back in the framework of this analysis are discussed.

1. Multiplicity condition

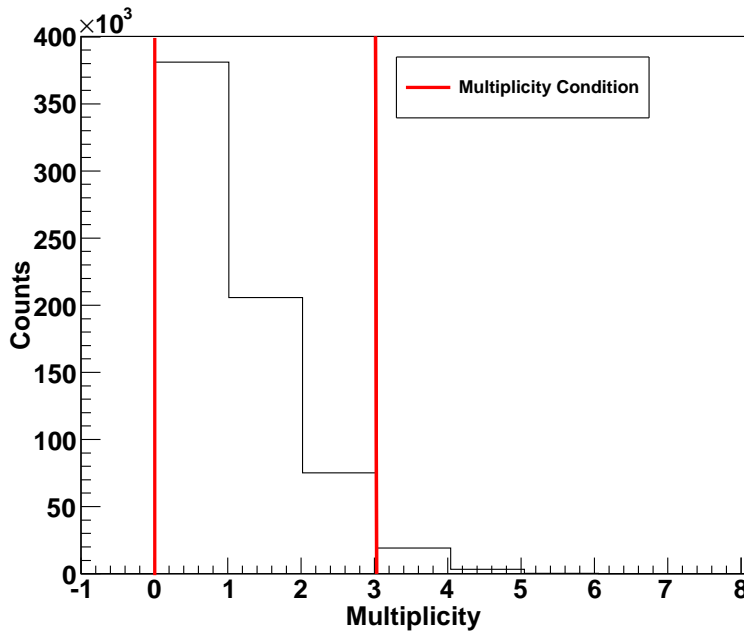


Figure 4.6: Multiplicity distribution of 7 crystals in a cluster obtained with  $^{152}\text{Eu}$  source. Majority of the events have multiplicity less than 4.

Multiplicity is defined as the number of individual crystals participating in one Compton scattering event within a cluster. In the present analysis add back within a RISING cluster of seven crystals was performed. In Fig. 4.6 the multiplicity distribution of the crystals in a

cluster obtained with a  $^{152}\text{Eu}$  source is shown. Multiplicity one events dominate the spectra and the events with multiplicity greater than three are negligible. The distribution clearly indicates that to recover the full energy of most of the Compton-scattered gamma rays adding of the gamma energies up to multiplicity three is necessary.

## 2. Energy condition

As mentioned above, the low energy gamma rays mainly lose their full energy in one interaction, predominantly by photoelectric effect. This property limits the energy below which the add back should not be done otherwise the photoelectrically absorbed gamma rays get added back to another random-coincident gamma giving a wrong total energy. In this analysis, the energies of scattered  $\gamma$  rays were added only if the sum of their energies was above 250 keV.

In some cases, the add back of energies in the region of a less intense low-energy gamma transition was avoided for example, the 132.5 keV gamma transition in  $^{125}\text{Cd}$  is a very weak transition (see Fig. 4.9) and was hidden in the background. To avoid the loss of events in the photopeak of this transition, add back was not performed if one of the two coincident gamma rays were less than 135 keV. Same conditions for energy add back were considered while analyzing the relative efficiencies of the gamma transitions.

## 3. Timing condition

A Compton-scattered gamma ray takes few nanoseconds to reach the adjacent crystals. Therefore, an appropriate timing condition should be employed while adding the energies of the  $\gamma$  rays from two adjacent crystals. Fig. 4.7 illustrates the dependence of the time delay to the energy difference of  $\gamma$  rays registered in neighbouring crystals. The optimum time to scatter was kept below 100 ns to obtain reasonable statistics with less background.

The intensity of a low energy gamma at 121.8 keV after and before add-back procedure remains comparable (see Fig. 4.8(a)) because the low energy  $\gamma$  rays are mostly absorbed via photoelectric absorption. The slight differences in the area under the two peaks are due to the energy sum condition which makes few of the  $\gamma$  rays to get added back to the background  $\gamma$  rays when their sum exceeds 250 keV. In Fig. 4.8(b) the gain in the intensities due to add back at higher energies is shown. The intensity of a 963.8 keV  $\gamma$  transition in  $^{152}\text{Eu}$  with add back is 15% higher than the intensity without add back. The intensity of the 963.8 keV transition, relative to the 121.8 keV

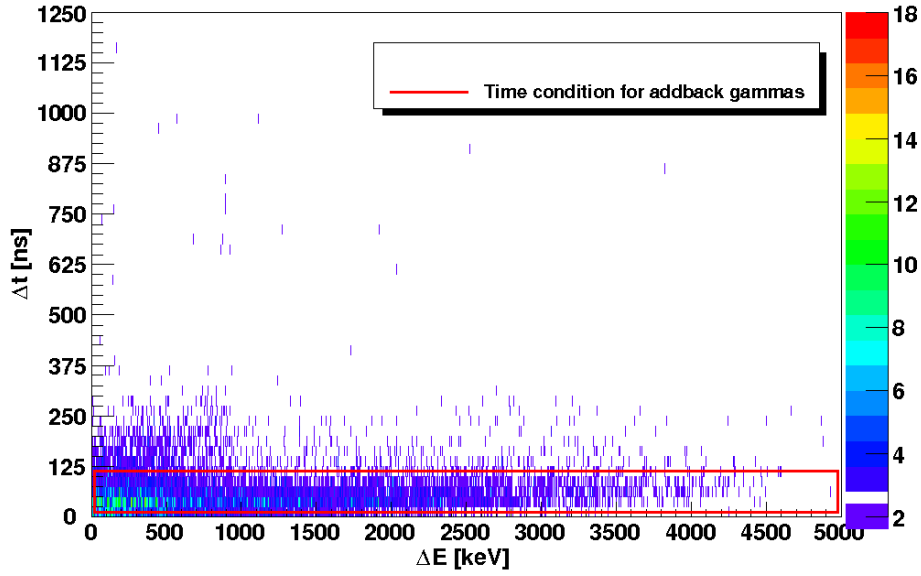
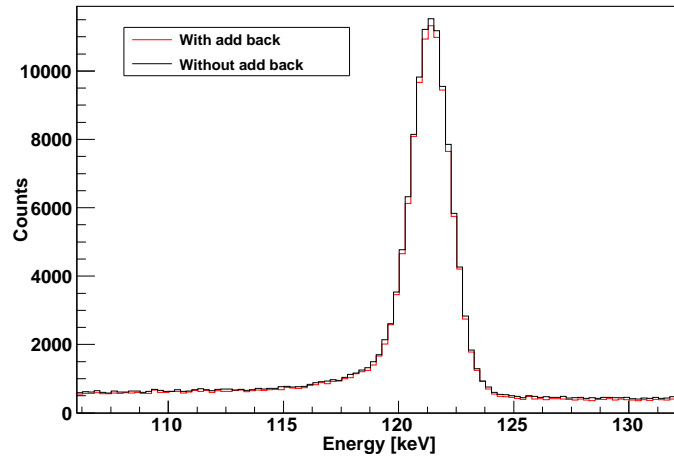


Figure 4.7: Difference in time as a function of difference in energies of gamma radiations recorded in two neighbouring crystals. Shown gate corresponds to the condition introduced in the analysis to consider gamma rays for add back.

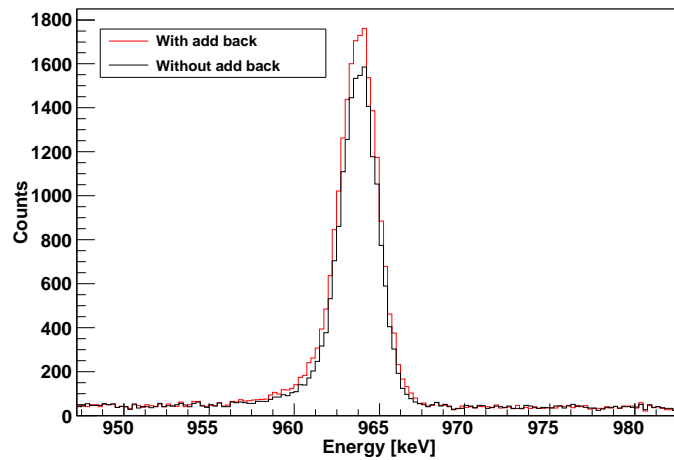
transition before and after add back amounts to 41.9(32)% and 50.3(31)%, respectively. The corresponding value quoted in the literature is 51.57(22)% [50], emphasizing the significance of the add-back procedure.

### 4.3.3 Lifetime analysis

The intensity distribution of  $\gamma$  transitions as a function of time was extracted by gating on the desired energy in the energy versus time matrix from the DGF electronics and projecting it on time axis. To account for the background contribution, the regions in the vicinity of the energy peak were selected and a normalized fraction of the resulting projection on the time axis was subtracted from the primary gated projection. Intensity of a  $\gamma$  transition originating from a single isomeric state varies exponentially according to eq. (3.32). Therefore, a single component exponential decay function given in



(a) Comparison of add-back efficiency to the singles efficiency for lower energies.



(b) Comparison of add-back efficiency to the singles efficiency for higher energies.

*Figure 4.8:* (a): The comparison between the intensity of a 121.8 keV  $\gamma$  transition before and after add back. (b): The spectrum showing the increase in the intensity of 963.8 keV transition after add back.

eq. (4.1) was used to fit the corresponding spectra to extract the half-life of the involved state.

$$\left(-\frac{dN}{dt}\right) = N_0 \frac{\ln 2}{T_{1/2}} e^{-(\ln 2)t/T_{1/2}}. \quad (4.1)$$

In this expression  $N$  and  $N_0$  represent the population of state in question at time  $t$  and  $t = 0$  respectively, and  $T_{1/2}$  is the half-life of the isomeric state.

If there are multiple isomeric states present in the decay, due to the complicated feeding patterns, intensity distributions of the  $\gamma$  transitions are governed by the combined decay of the states.

In the present data, gamma lines having a side feeding from a second isomer were seen and thus, eq. (4.4) was derived to describe a two component exponential decay behaviour as follows: Assuming two states  $a$  and  $b$  in a nucleus decaying in such a way that  $a$  feeds  $b$  with decay constants,  $\lambda_a$  and  $\lambda_b$ , respectively. The rate of decay of the parent state  $a$  can then be written as

$$-\frac{dN_a}{dt} = N_a \lambda_a. \quad (4.2)$$

The population of the state  $b$  in time increases as a result of decays of the parent state  $a$  and decreases because of its own decay. The activity of state  $b$  is expressed as

$$\left(\frac{dN_b}{dt}\right)_{Total} = -\frac{dN_a}{dt} + \frac{dN_b}{dt} = N_a \lambda_a - N_b \lambda_b. \quad (4.3)$$

At  $t = 0$ , both the isomeric states  $a$  and  $b$  have initial populations of  $N_0$  and  $N'_0$ , respectively. Solving the equation with an initial condition,  $N_a(0) = N_0$  and  $N_b(0) = N'_0$ , the observed decay rate  $\frac{dN_b}{dt}$  is

$$\left(\frac{dN_b}{dt}\right)_{Total} = -\lambda_b(N'_0 e^{-\lambda_b t}) - \lambda_a^2 \frac{N_0 e^{-\lambda_a t}}{\lambda_b - \lambda_a} + \lambda_a \lambda_b \frac{N_0 e^{-\lambda_b t}}{\lambda_b - \lambda_a}. \quad (4.4)$$

The intensity distribution of  $\gamma$  transitions originating from a secondary isomer as a function of time strongly depends on the difference in the decay constants of the primary and secondary isomers and their population ratio  $N_0/N'_0$  in the reaction.

#### 4.3.4 Building level schemes

The following rules and assumptions were considered while constructing level schemes for the nuclei. The intensities and branching ratios of all the transitions in the level scheme including the respective conversion coefficients

should balance each other. Due to the unavailability of spins and parities of the levels through the experiment, the spins and parities were assigned to the energy levels based on half-lives, branching ratios of the  $\gamma$  transitions and a comparison to the systematics of neighbouring odd-mass Sn and Cd isotopes. This topic is dealt with in chapter 5, where the spin and parity assignments of the levels in individual nucleus are discussed in details. Only the increasing values of spins with increasing level energies were assumed.

#### 4.3.4.1 Relative gamma intensities

To build the level schemes of the nucleus unambiguously, it is important to determine the intensities of gamma transitions accurately. There are mainly two ways of doing this:

1. Fitting the energy peaks in the singles gamma-ray spectrum and calculating the intensities using its relation with the efficiency of the detector

$$I_{\gamma} = \frac{N_{\gamma}^{(s)}}{\epsilon_{\gamma}^{(rel)}}, \quad (4.5)$$

where  $I_{\gamma}$  is the intensity of the  $\gamma$  ray,  $N_{\gamma}^{(s)}$  is the area under the photopeak in the singles gamma spectrum and  $\epsilon_{\gamma}^{(rel)}$  is the relative photopeak efficiency of the detector.

2. Fitting the energy peaks in the  $\gamma\gamma$ -coincidence spectra and using a similar relation

$$I_{\gamma} = \frac{N_{\gamma}^{(coin)}}{\epsilon_{\gamma}^{(rel)} \epsilon_{coin}^{(rel)}}. \quad (4.6)$$

In this expression,  $N_{\gamma}^{(coin)}$  represents the area under the photopeak in the coincidence spectrum of the gated  $\gamma$  ray,  $\epsilon_{coin}^{(rel)}$  is the corresponding relative photopeak efficiency and  $\epsilon_{\gamma}^{rel}$  is the relative efficiency for the gated  $\gamma$  ray. In this analysis the background is rather low as compared to the singles spectrum because of the coincidences between the  $\gamma$  transitions. Hence, the method is useful to determine the intensities of the weak transitions which are barely visible above background in the singles spectrum.

The gamma intensities calculated using relative photopeak efficiencies in both the methods have to be normalized to a gamma line. The aforementioned methods of extracting relative gamma intensities make sense only if the time of measurement is equal for all the  $\gamma$  transitions. However, in

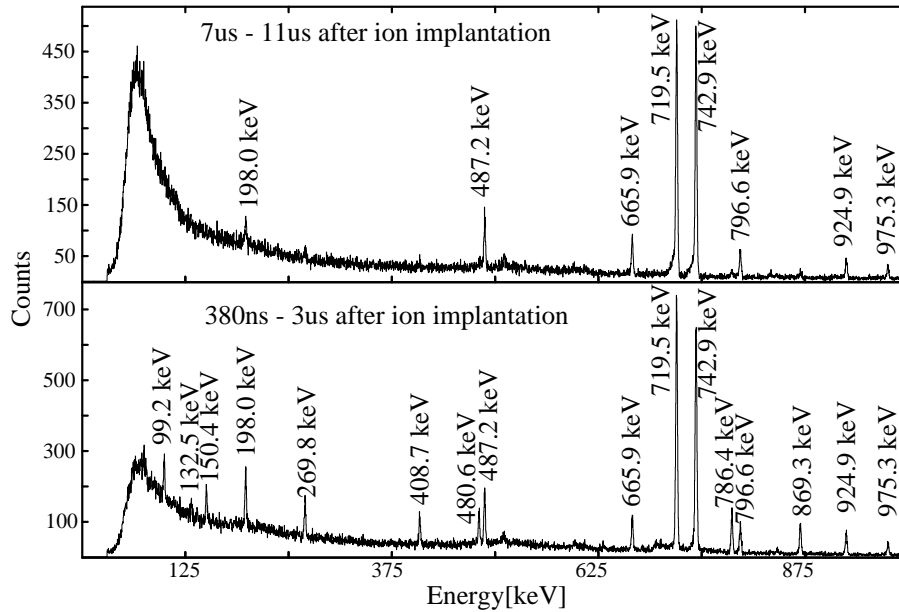


Figure 4.9: Energy spectra for  $^{125}\text{Cd}$  with time windows of 380 ns to 3  $\mu\text{s}$  and 7  $\mu\text{s}$  to 11  $\mu\text{s}$  after implantation. The absence of 99.2 keV, 132.5 keV, 150.4 keV, 269.8 keV, 408.7 keV, 480.6 keV, 786.4 keV and 869.3 keV transitions in the latter spectrum (top panel) indicates that they are emitted by a shorter living isomer.

the present analysis the condition applied on the energy versus time matrix shown in Fig. 3.19 was used to separate out the prompt flash, which evidently results in a lower intensity for the  $\gamma$  transitions with energies less than 400 keV. The missing intensities of the low-energy transitions were recovered by extrapolating their time distributions with characteristic half-lives to the time of ion implantation. The ratio of area under the curve starting from the time of implantation to the time of start of gating condition and area corresponding to the total time spanned by the gate was added to the experimentally measured number of counts under the peak. The relative gamma intensities obtained in this way are relevant to establish the presence of more than one isomeric state in the decay of a nucleus. For example, in Fig. 4.9, the singles gamma energy spectra of  $^{125}\text{Cd}$  with two different time ranges after the ion implantation are shown. The energy spectrum obtained by imposing a condition on the time of emission of the  $\gamma$  transitions to be within 380 ns to 3  $\mu\text{s}$  after implantation, consists of a set of  $\gamma$  transitions which are not visible in the spectrum with time range of 7  $\mu\text{s}$  - 11  $\mu\text{s}$ . This difference in the relative intensities of transitions for two time ranges revealed the presence of at least two isomeric states in  $^{125}\text{Cd}$ , one decaying with a half-life

of less than  $7 \mu\text{s}$  and the other living for a comparatively longer time. The results are presented in details in chapter 5.

#### 4.3.4.2 $\gamma\gamma$ -coincidence spectra

The  $\gamma\gamma$ -coincidence matrices were constructed for different time delay,  $\Delta t$  expressed as in expression (4.7). To obtain the prompt coincidences, a narrow time window with  $\Delta t < 100 \text{ ns}$  was employed and an open time condition yielded the delayed coincidences.

$$\Delta t = T_{\gamma_1} - T_{\gamma_2}, \quad (4.7)$$

where  $T_{\gamma_1}$  and  $T_{\gamma_2}$  represent the time of emission of the  $\gamma$  transitions,  $\gamma_1$  and  $\gamma_2$ , respectively.

The coincidence spectrum gated on a  $\gamma$  line was extracted by projecting the symmetrized  $\gamma\gamma$ -coincidence matrix on one of the axis.

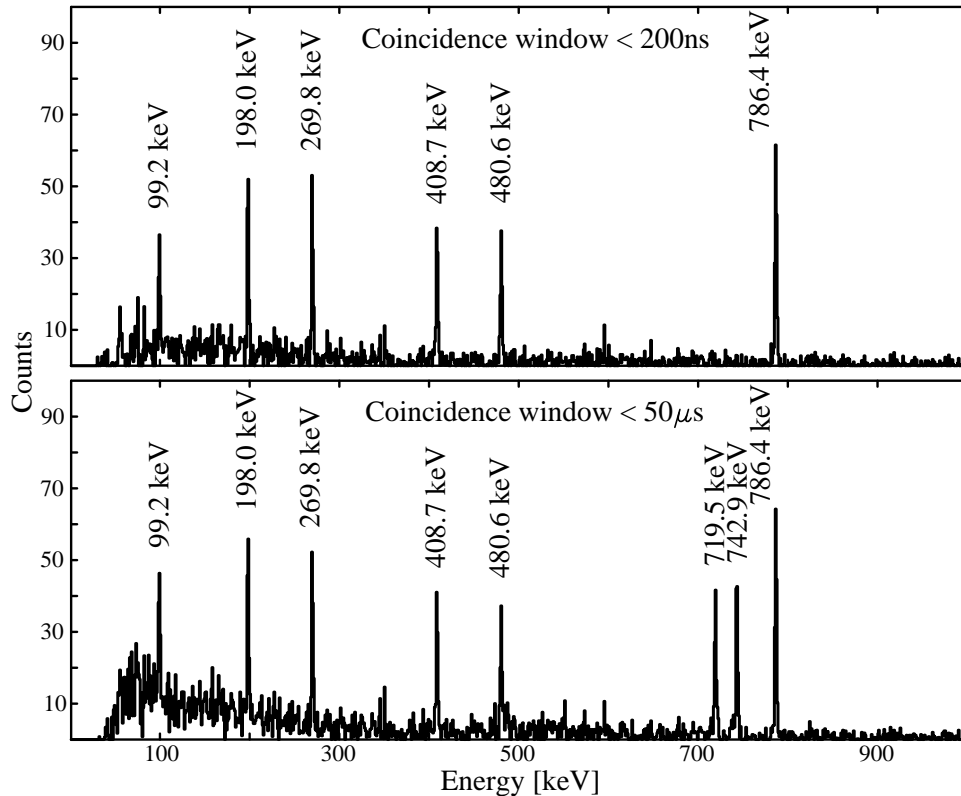


Figure 4.10: Coincidence  $\gamma$  spectra of 869.3 keV transition in  $^{125}\text{Cd}$  for two time windows of  $\Delta t < 200 \text{ ns}$  and  $\Delta t < 50 \mu\text{s}$ .

A  $\gamma$  transition  $\gamma_2$ , having different intensity in the spectra with same

primary gate  $\gamma_1$  but with different  $\Delta t$  gives an indication about the state fed or depopulated by one of these transitions being isomeric. In Fig. 4.10 the coincidence spectra of  $\gamma_1 = 869.3$  keV in  $^{125}\text{Cd}$  for  $\Delta t < 50 \mu\text{s}$  and  $\Delta t < 200$  ns respectively, are shown. The transitions at 719.5 keV and 742.9 keV are not present in the spectrum with a coincidence window of 200 ns. However they are in coincidence when  $\Delta t$  is increased to  $50 \mu\text{s}$  which indicates that the level fed by the 869.3 keV transition and depopulated by the 719.5 keV and 742.9 keV transitions has a half-life greater than 200 ns, thus the latter transitions are in delayed coincidence with the former ones.

#### 4.3.4.3 The $\gamma\gamma\Delta t$ matrix

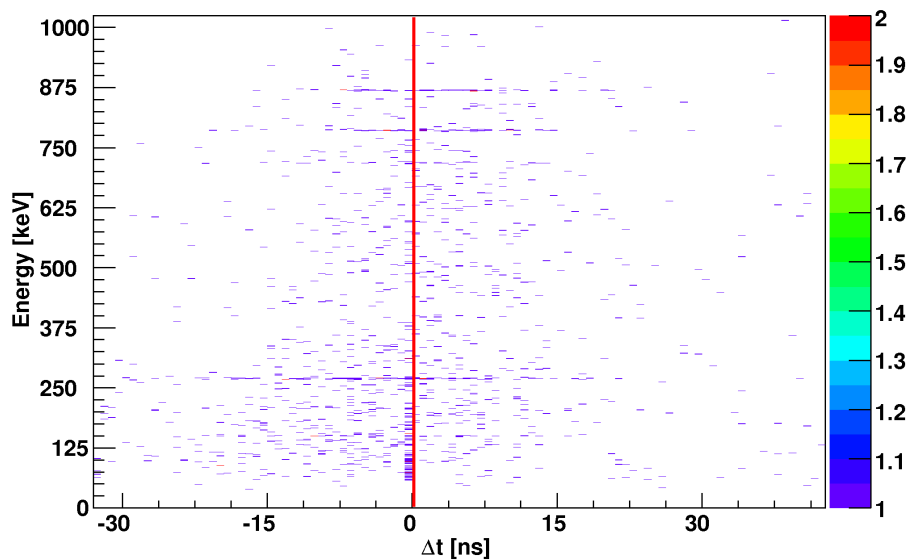
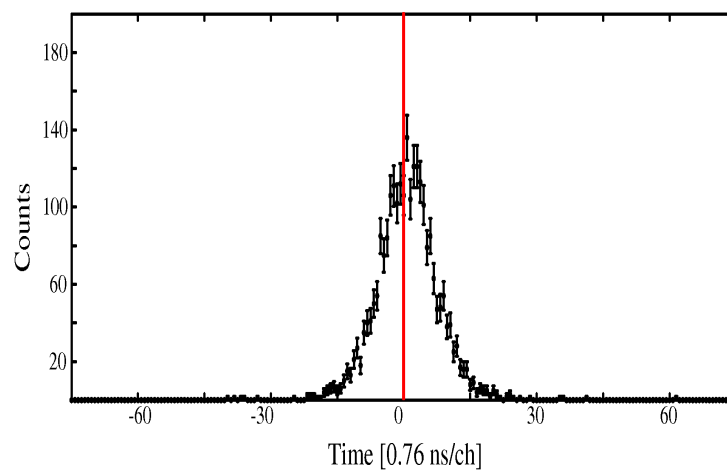


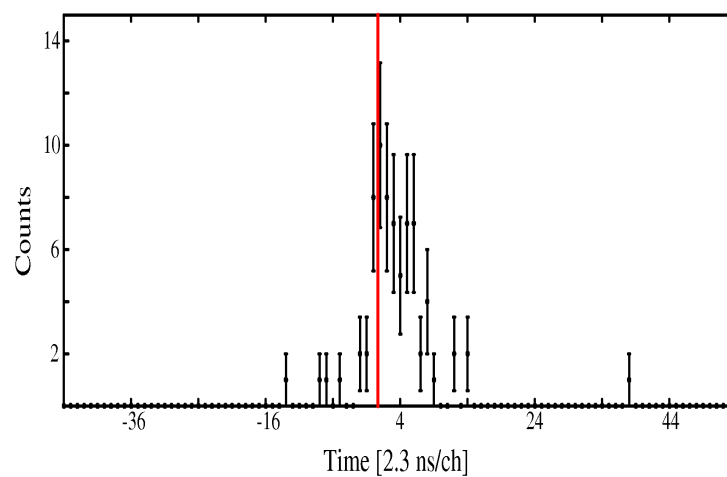
Figure 4.11: A typical  $\gamma\gamma\Delta t$  matrix gated on 198.0 keV transition in  $^{125}\text{Cd}$ . The red line indicates the zero time.

The  $\gamma\gamma\Delta t$  matrix is a two-dimensional matrix of the energy of  $\gamma$  transitions in coincidence with the gated  $\gamma$  line versus their relative time of emission,  $\Delta t$ . An example  $\gamma\gamma\Delta t$  matrix for the 198.0 keV transition in  $^{125}\text{Cd}$  is shown in Fig. 4.11. This matrix is useful to define the ordering of gamma transitions in the level schemes. The one-dimensional projection of relative time distributions of the coincident  $\gamma$  transitions have a symmetric Gaussian distribution if the level associated with the two gamma rays has a half-life

smaller than the resolution of timing electronics. In Fig. 4.12(a), the relative time distribution of  $\gamma$  transitions in prompt coincidence is shown. The zero time was marked by the implantation of ions and was extracted from the centroid of time distribution of the prompt flash. A delayed coincidence between two  $\gamma$  transitions creates an asymmetry in their relative time distribution and shifts its centroid away from the zero time line. Measure of this shift in the centroid determines the half-life of the isomeric state associated with the two transitions. The ordering of transitions in the level schemes is fixed in accordance with the direction of the centroid shift. Data from the long-range TDC was used to obtain the relative time between two coincident  $\gamma$  rays. A resolution of 0.76 ns/ch of the TDC implies that half-lives of the order of few ns can be detected by this method [51].



(a)



(b)

Figure 4.12: (a): The symmetric Gaussian distribution of relative time between two prompt-coincident  $\gamma$  transitions. The red line is the zero time. (b): Relative time distribution of two delayed  $\gamma$  rays with a shift in the centroid with respect to zero time.

# Chapter 5

## Results

The experimental findings on  $^{127,125,129}\text{Cd}$  are presented in this chapter.  $^{127}\text{Cd}$  is discussed prior to  $^{125,129}\text{Cd}$  in accordance with their impact on the conclusion made in chapter 6.

### 5.1 $^{127}\text{Cd}$

So far gamma transitions in  $^{127}\text{Cd}$  were identified in two previous experiments. Hellström *et al.* [52] assigned four gamma transitions at energies 710, 738, 820 and 342 keV to the isomeric decay. In the work of Hoteling *et al.* [53], apart from the two previously observed 738 and 820 keV gamma rays, two new gamma transitions at energies 770.9 and 908.9 keV were identified. A level scheme for  $^{127}\text{Cd}$  based on the systematics of known neighbouring odd mass Cd isotopes was constructed in the latter paper. However, no lifetime information could be extracted from the data. In the present experiment the previously reported  $\gamma$  transitions at energies 739, 821 and 711 keV were affirmed and two new gamma rays at energies 110.4 and 848.9 keV were identified. However, the 771 and 909 keV transitions reported in Ref. [53] and 342 keV transition reported in Ref. [52] could not be confirmed in the present work. The reason for such a discrepancy in the three data sets could be attributed to the poor statistics in [52] and the lack of time correlation of the gamma rays with ions and gamma-gamma events in [53], resulting in contributions from the neighbouring In and Sn isotopes in the assigned  $\gamma$  spectrum of  $^{127}\text{Cd}$ . The reaction mechanism to produce the  $^{127}\text{Cd}$  isotope in the three experiments was same, namely the fragmentation of  $^{136}\text{Xe}$  on a  $^9\text{Be}$  target with a difference in the energies of the incident beam. The reaction kinematics in different energy regimes could vary the resulting population of the isomeric states. It has been observed in multiple experiments involving

high energy fragmentation reaction that with increasing spin the population of the levels drops. Considering the increase in statistics by three orders of magnitude in the present data compared to the previous data sets, it is rather impossible to miss additional gamma rays at 771 keV and 909 keV assigned to depopulate the levels with spins  $23/2^-$  and  $27/2^-$ , respectively with intensities above 1% of the most intense transition in Ref. [53].

The  $^{127}\text{Cd}$  isotope was produced in two different settings of the FRS, one optimized for the maximum transmission of  $^{130}\text{Cd}$  and the other one tuned to predominantly transmit  $^{126}\text{Cd}$ . The specifications of the experiment are discussed in chapter 3. Stringent conditions imposed on the selection procedure of the FRS along with a clean identification of the particles shown on page 47-50 of chapter 4, enabled the observation of  $7.2 \times 10^5$   $^{127}\text{Cd}$  ions in total from the two settings. A singles  $\gamma$ -ray spectrum containing five  $\gamma$  transitions assigned to the decay of the isomer in  $^{127}\text{Cd}$  obtained from the energy versus time matrix with a condition to remove the prompt flash is shown in Fig. 5.1.

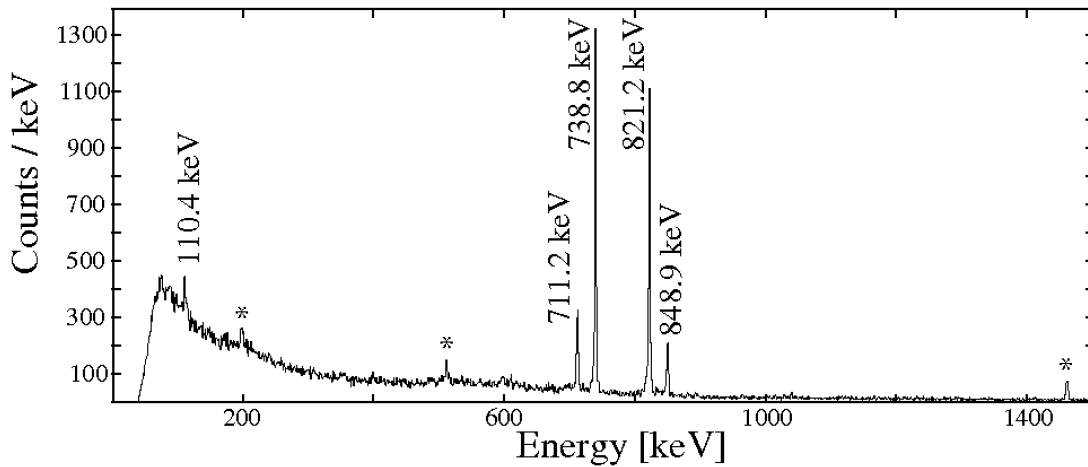


Figure 5.1: Singles gamma-ray energy spectrum of  $^{127}\text{Cd}$  with a time window of 380 ns - 50  $\mu\text{s}$  after the ion implantation. Background lines are marked with asterisk (\*).

The singles  $\gamma$  spectrum was constructed for a time range of 380 ns - 50  $\mu\text{s}$  after the ion implantation. The relative intensities of observed transitions are summarized in Table 5.1. The observed  $\gamma\gamma$ -coincidence relations of the five transitions associated with the isomeric decay in  $^{127}\text{Cd}$  are shown in Fig. 5.2. Coincidences were also investigated for two different coincidence time windows of 100 ns and 50  $\mu\text{s}$ .

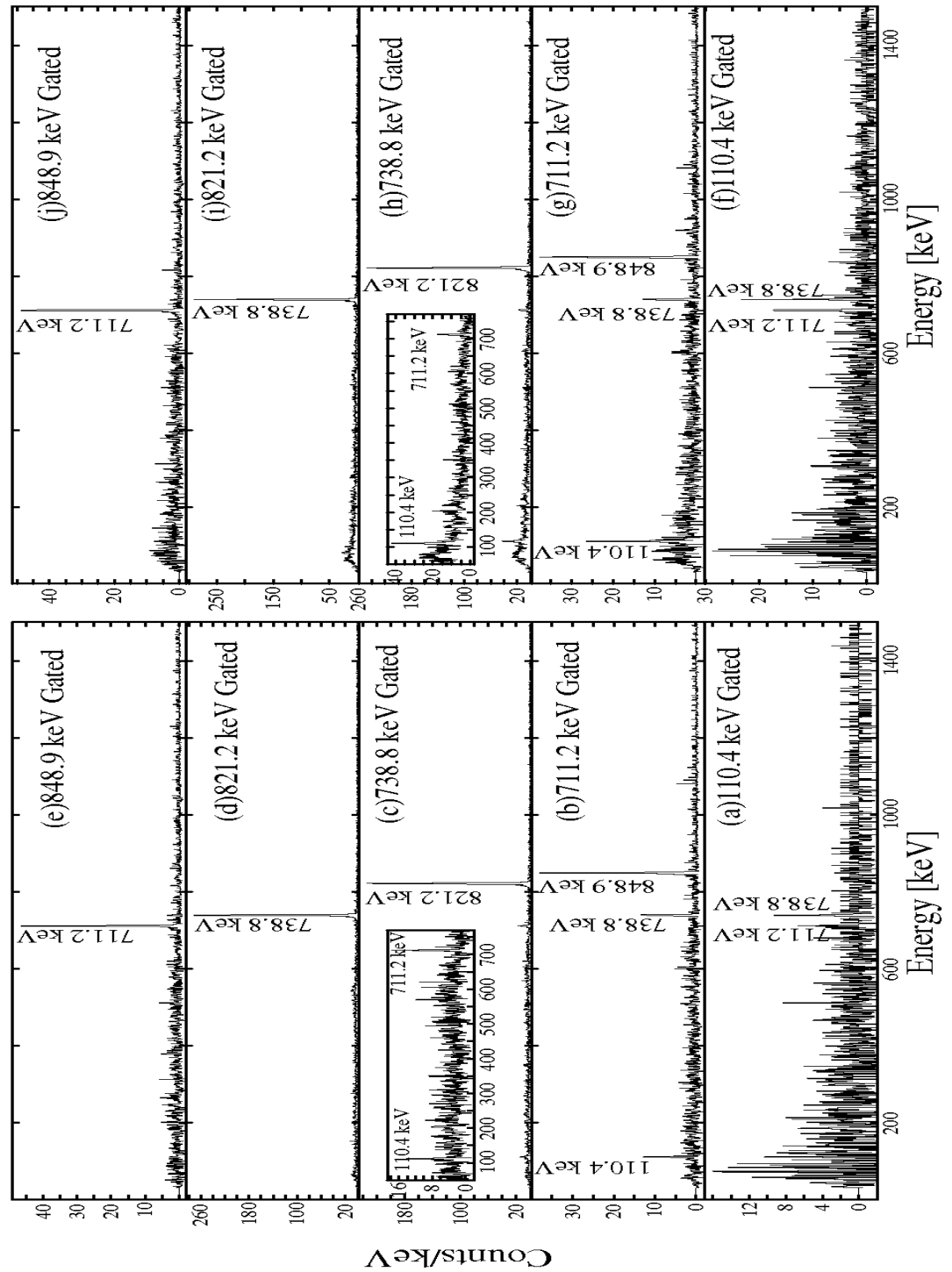


Figure 5.2:  $\gamma\gamma$ -coincidence spectra of five gamma transitions assigned to the decay of  $^{127}\text{Cd}$  with a coincidence window of 100 ns (a,b,c,d,e) and 50  $\mu\text{s}$  (f,g,h,i,j).

*Table 5.1:* Summary of the measured relative gamma intensities and the half-lives of isomeric states in  $^{127}\text{Cd}$ . Level energies are given with respect to the  $(11/2^-)$   $\beta^-$  decaying isomer. The gamma intensities are normalised to the 738.8 keV transition.

$E_i + x$	$T_{1/2}$	$E_\gamma$	$T_{1/2}$	$I_\gamma$
[keV]	[ $\mu\text{s}$ ]	[keV]	[ $\mu\text{s}$ ]	[%]
711		711.2(2)	17.1(8) <sup>b</sup>	23.0(9)
821		821.2(2)	17.7(4) <sup>b</sup>	91.8(30)
		110.4(2)	17.5(12) <sup>b</sup>	6.2(6)
1560	17.5(3) <sup>a</sup>	738.8(2)	17.6(4) <sup>b</sup>	100.0(31)
		848.9(2)	17.9(6) <sup>b</sup>	17.3(7)

<sup>a</sup> Extracted from the fit of the sum of time distributions of the 711.2, 738.8, 821.2 and 848.9 keV transitions with a single exponential decay function.

<sup>b</sup> Extracted from the fit of the time distribution of corresponding individual gamma transition with a single exponential decay function.

The relative intensities of all the  $\gamma$  lines in the aforementioned conditions are similar and it confirmed the presence of only one isomer in the decay. Placement of the  $\gamma$  transitions in the level scheme was based on the following arguments. The two most intense  $\gamma$  rays of energies 738.8 and 821.2 keV most likely form a single cascade due to intensity balance. The mutual coincidence of these two  $\gamma$  lines shown in Fig. 5.2(c) and Fig. 5.2(d) confirms their placement as one feeding the other. Similarly the other two high energy  $\gamma$  lines at 711.2 keV and 848.9 keV have comparable relative intensities and are in mutual coincidence, thus were assigned to form a single cascade. As the sum of energies of the 738.8 and 821.2 keV lines is equal to that of the 848.9 and 711.2 keV lines, they form parallel competing branches originating from the same level. The absence of coincidence between these two cascades supports the above argument. Observation of a 110.4 keV transition coinciding with the differences in energies of the 848.9, 738.8 and 711.2, 821.2 keV lines suggests that an intermediate level is present, fed by the 110.4 keV transition. Coincidence of 110.4 keV transition with 711.2 and 738.8 keV lines supports the argument of an intermediate level connecting the two cascades via the 110.4 keV transition.

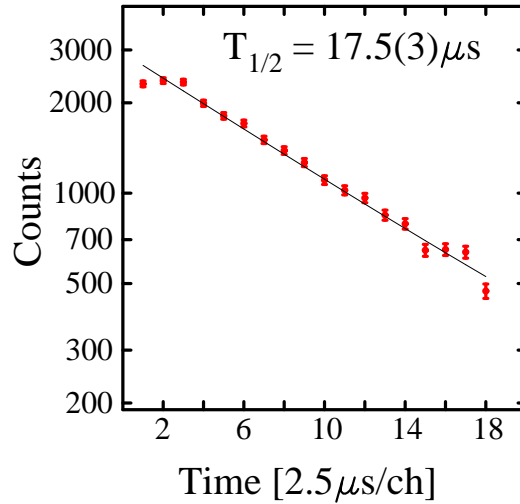


Figure 5.3: The sum of time distributions of the 711.2, 738.8, 821.2 and 848.9 keV transitions with a single exponential decay fit.

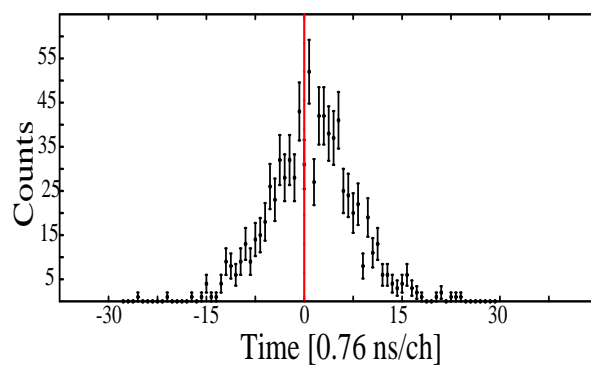
The half-life of the decaying isomer was extracted by fitting the sum of time distributions of the 711.2, 738.8, 821.2 and 848.9 keV transitions with a single exponential decay function as in Fig. 5.3. A half-life of  $17.5(3) \mu\text{s}$  was obtained for the isomeric state. The fit of the time distributions of individual gamma lines with the same function as described above was also performed and the results are listed in Table 5.1.

From the half-life information and the inferred electromagnetic transition probabilities, the multipolarity of the  $\gamma$  transitions is determined. Due to the similar values of the half-life extracted from the time distributions of the 711.2, 738.8, 821.2 and 848.9 keV transitions (see Table 5.1), all four of them qualify to depopulate the isomeric state. Considering their energies, a multipolarity of  $M2$  or  $E3$  for all of them supports the existence of a half-life of  $17.5(3) \mu\text{s}$  for the decaying state. Any other multipolarity, example  $M1$  or  $E2$  would result in a half-life of less than 1 ns, alternatively an  $M3$  or  $E4$  character would require a longer half-life of  $\sim 0.1$  s for the isomer. The relative time difference between the 738.8 and 821.2 keV and the 848.9 and 711.2 keV transitions obtained from the long-range TDC (with a time resolution of 0.76 ns/ch) of Ge clusters show symmetric Gaussian distributions with no centroid shift (see Fig. 5.4). This implies that the two intermediate levels populated by the 738.8 and 848.9 keV transitions and depopulated by the 821.2 keV and 711.2 keV transitions or viceversa have a half-life of less than 10 ns. A longer lifetime would lead to clear asymmetries in the respective

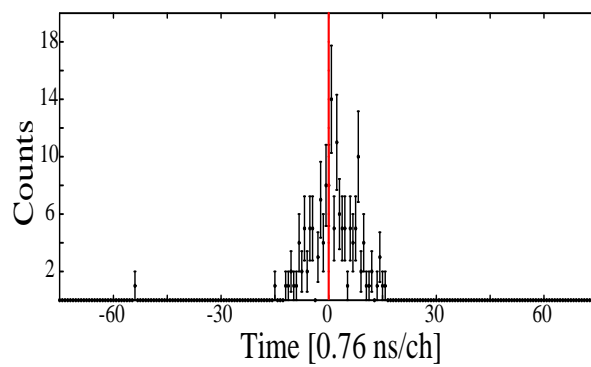
relative time distributions as observed in the case of  $^{128}\text{Cd}$  [6]. Hence, the ordering of the 738.8 keV  $\gamma$  line with respect to the 821.2 keV transition and that of the 848.9 keV  $\gamma$  line with respect to the 711.2 keV transition could not be determined based on the experimental data. Therefore, two scenarios (EXP-I and EXP-II) shown in Fig. 5.5 are proposed for the placement of these four  $\gamma$  lines in the level scheme. A 110.4 KeV transition decaying from a level which is believed to have a half-life of less than 10 ns can be best described to have an  $M1$  character.

The assignment of spins and parities to the excited states was not possible with the experimental data and hence is based on the reduced transition probabilities and the experimental information on the level scheme of the  $^{129}\text{Sn}$  isotone [54] (see Fig. 5.5). Since  $^{129}\text{Sn}$  has the same number of neutron holes in the  $^{132}\text{Sn}$  core as  $^{127}\text{Cd}$ , it provides the best case for comparison. According to the  $\beta^-$  decay studies of  $^{127}\text{Cd}$ ,  $(3/2^+)$  is assigned to the  $\beta^-$  decaying ground state [55]. The systematics of odd mass Cd and Sn isotopes [53, 54] confirms that the  $\gamma$ -decaying isomer is built on a  $(11/2^-)$  state with an energy of around 300 keV above the  $(3/2^+)$  ground state estimated from the systematics of  $^{121,123}\text{Cd}$  [56]. Due to the large spin difference and long partial lifetime, a  $\gamma$  transition between the  $(11/2^-)$  and  $(3/2^+)$  states is not observed and thus the former decays by a  $\beta^-$  emission. In the absence of any information about the exact energy of the  $(11/2^-)$  state, the following discussion always refers to the energies of levels, relative to the  $(11/2^-)$  ground state.

Since in  $^{129}\text{Sn}$  isomerism is mainly caused by  $E2$  transitions of very low energies or a hindered  $M2$   $(19/2^+) \rightarrow (15/2^-)$  transition (see Fig. 5.5), a similar explanation was assumed to be the reason of isomer formation in  $^{127}\text{Cd}$  by Hellström *et al.* [52]. While in the present work the observed half-life of the isomer was attributed to a competition between an  $M2$  and an  $E3$  transition. The basis of this conclusion is explained below. In  $^{127}\text{Cd}$ , a  $(19/2^+) \rightarrow (15/2^+)$   $E2$  spin trap analogous to the one observed in  $^{129}\text{Sn}$  would require an observation of a low-energy gamma ray along with the two competing  $E1$  transitions,  $(15/2^+) \rightarrow (15/2^-)$  and  $(15/2^+) \rightarrow (13/2^-)$  with similar intensities. Combination of a half-life of 17.5  $\mu\text{s}$  for the isomeric state and a reduced transition probability of 1.0 W.u (estimated from the  $B(E2)$  value adopted for the  $(19/2^+) \rightarrow (15/2^+)$   $E2$  transition in  $^{129}\text{Sn}$ ) limits the energy of the analog  $E2$  transition in  $^{127}\text{Cd}$  to  $< 30$  keV. Due to the experimental constraint, a 30 keV gamma ray cannot be observed in the present data. However, the encountered branching ratios for the 738.8 keV and 848.9 keV transitions considering that both of them decay from the same state are 85.3 % and 14.7 %, respectively. If the reversed ordering of the cascades is taken into account, the two competing  $\gamma$  transitions at



(a) Relative time distribution between the 738.8 keV and 821.2 keV transitions.



(b) Relative time distribution between the 848.9 keV and 711.2 keV transitions.

*Figure 5.4:* The two relative time spectra showing symmetric distribution with respect to the zero time denoted by red line.

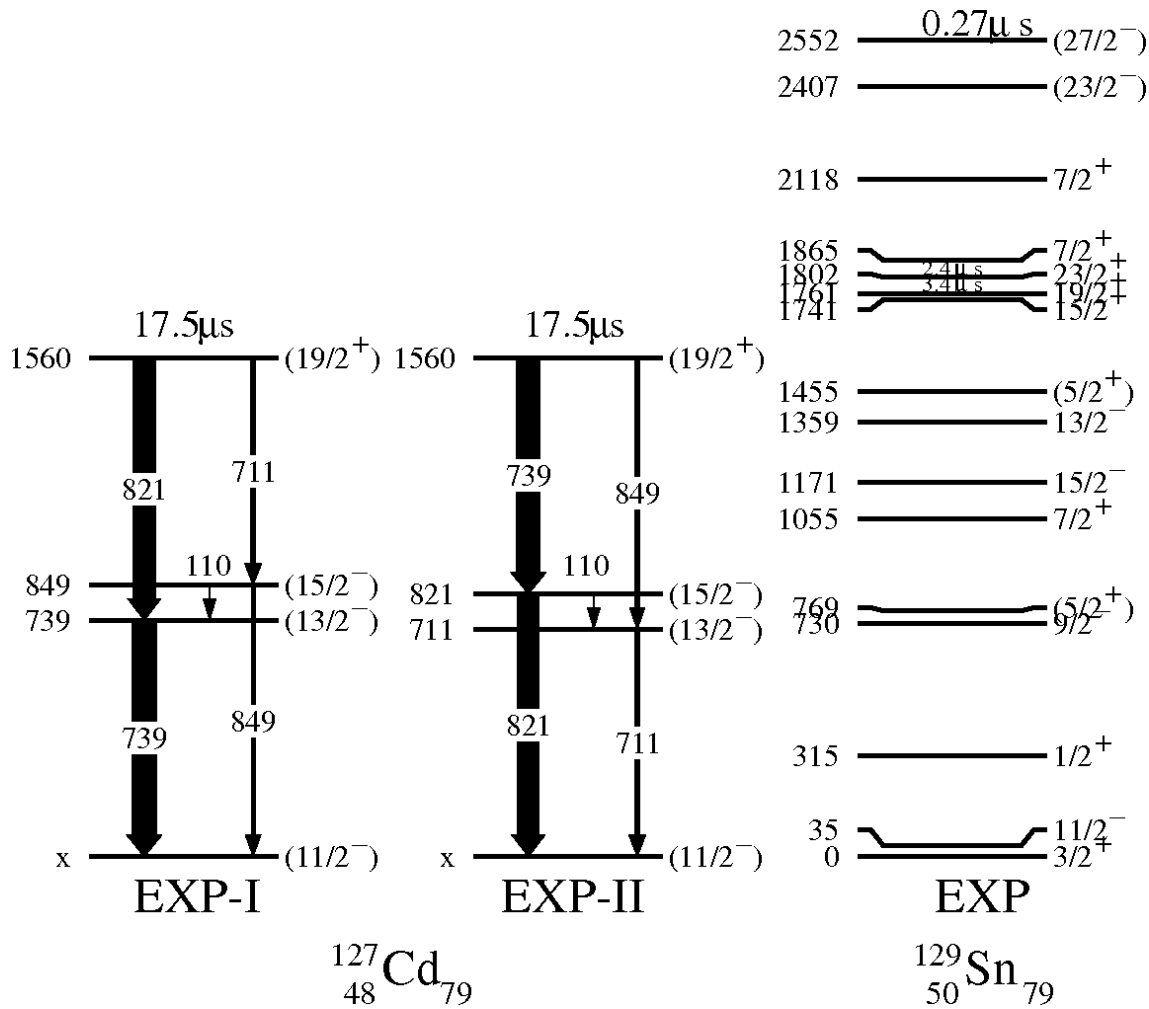


Figure 5.5: The proposed level schemes for  $^{127}\text{Cd}$ . The two possible arrangements of  $\gamma$  transitions are labeled as EXP-I and EXP-II. The energies of the excited levels are with respect to the  $(11/2^-)$  state. Experimental level structure of  $^{129}\text{Sn}$  is shown for comparison.

energy 711.2 keV and 821.2 keV have branching ratios of 20.0 % and 80.0 %, respectively. This considerable difference in the branching ratios of the two transitions in both the scenarios rules out the possibility that both of them have an  $E1$  character and decay from the state with spin and parity of  $(15/2^+)$ .

Alternatively, if a  $(15/2^+)$  state happens to lie above the  $(19/2^+)$  state causing an isomer, the fast  $(15/2^+) \rightarrow (15/2^-)$  and  $(15/2^+) \rightarrow (13/2^-)$  transitions would not let the corresponding state to be isomeric with a half

life of 17.5  $\mu\text{s}$ . Hence we can conclude that an  $M2$  transition from  $(19/2^+)$  to  $(15/2^-)$  in competition with an  $E3$  transition from  $(19/2^+)$  to  $(13/2^-)$  is responsible for the measured half-life of the isomer. This argument allowed us to assign a spin of  $(19/2^+)$  to the decaying isomeric state. The decay of intermediate state at 849 keV in scenario (EXP-I) and 821 keV in scenario (EXP-II) (see Fig. 5.5) is governed by a competition between the 110.4 and 848.9 keV or 821.2 transitions, respectively. The experimental branching ratio of 110.4 keV gamma line in the two cases is 26% and  $\sim 6\%$ , respectively (see Table 5.2). The expected value of this ratio for an  $M1$  transition at 110.4 keV energy and the 848.9 keV or 821.2 keV transitions having  $M1$  multipolarity and equal reduced strength is  $\sim 0.5\%$ . The difference of an order of magnitude between the experimental branching ratio and the value obtained from the energy scaling suggests that the observed competition between the 110.4 keV transition and the 848.9 keV or 821.2 keV transitions is only possible if one of them has a higher multipolarity. From the discussion on page 67-68,  $M1$  character for the 110.4 keV transition is established. Therefore, this intermediate state was assigned to have spin-parity  $(15/2^-)$ , depopulated by a competition of a 110.4 keV  $M1$  transition and a 821.2 or 848.9 keV  $E2$  transition. The proposed spin and parity assignments of the excited levels in  $^{127}\text{Cd}$  are shown in Fig. 5.5 along with the experimental level scheme of  $^{129}\text{Sn}$  isotone. In Table 5.2 the experimentally obtained reduced transition strengths and the branching ratios for the primary transitions in the two scenarios are summarized.

Table 5.2: Experimental transition strengths and  $\gamma$ -branching ratios. Separate values are given for the two alternative experimental level schemes EXP-I and EXP-II of  $^{127}\text{Cd}$ .

Transition	$\sigma L$ $J \rightarrow I$	B( $\sigma L$ ) (W.u)	
		EXP-I	EXP-II
$(19/2^+) \rightarrow (13/2^-)$	$E3^a$	$2.30(30) \times 10^{-1}$	$3.40(18) \times 10^{-2}$
$(19/2^+) \rightarrow (15/2^-)$	$M2^a$	$7.71(16) \times 10^{-5}$	$2.71(14) \times 10^{-4}$
$(15/2^-) \rightarrow (13/2^-)$	$M1^b$	26(3)%	6.3(6)%
$(15/2^-) \rightarrow (11/2^-)$	$E2^b$	74(3)%	94(4)%

<sup>a</sup> Pure transition assumed.

<sup>b</sup> Only  $\gamma$ -branching ratio known.

## 5.2 $^{125}\text{Cd}$

The previous experiments at LOHENGRIN mass separator at ILL in Grenoble [57], the NSCL at Michigan State University [53] and the FRS at GSI, Germany [52] report on the decay structure of isomers in  $^{125}\text{Cd}$ . Hellström *et al.* [52] observed four  $\gamma$  transitions associated with the isomeric decay of this nucleus. A half-life of 14(2)  $\mu\text{s}$  for the isomer was measured in their work, however due to poor statistics no further information could be extracted from the experimental data. The work of Scherillo *et al.* [58] extended the studies on  $^{125}\text{Cd}$  in a separate measurement and confirmed the 720 keV and 743 keV gamma transitions with a half-life of 19(2)  $\mu\text{s}$  for the decaying isomer. In the absence of any  $\gamma\gamma$ -coincidence measurement, a tentative placement of these two gamma lines in the level scheme was made and the isomeric state was assigned a spin and parity of  $19/2^+$  based on the known level structure of  $^{123}\text{Cd}$ . Later in Ref. [53], five additional gamma transitions were observed and the existing level scheme was extended up to the spin of  $33/2^-$ . No information on the half-life of isomeric state was provided and due to the lack of  $\gamma\gamma$ -coincidence, the proposed level structure was based on the systematics of neighbouring odd-mass Cd isotopes. Thanks to the new experimental information on this nucleus, the previously proposed level scheme [53] is extended up to the level having a spin around  $35/2\hbar$  and two new isomers have been observed along with the previously known ( $19/2^+$ ) isomer [52, 58].

$^{125}\text{Cd}$  being less neutron rich, is produced in higher abundance comparative to the neighbouring neutron-rich isotopes. Experimentally,  $^{125}\text{Cd}$  was also produced in both the FRS settings, however only the setting centered at  $^{126}\text{Cd}$  could be used to do the isomer spectroscopy of  $^{125}\text{Cd}$  because in the  $^{130}\text{Cd}$  setting, the  $^{125}\text{Cd}$  isotope was not transmitted through the FRS due to its magnetic rigidity being beyond the maximum momentum acceptance of the spectrometer. The observed large density of states in  $^{125}\text{Cd}$  is a consequence of the coupling of 5 neutron and 2 proton valence holes in the closed  $N = 82$ ,  $Z = 50$  shell giving rise to a large number of closely spaced energy levels. The obtained singles gamma-ray spectrum for the full time range of 50  $\mu\text{s}$  excluding the prompt flash after implantation of  $^{125}\text{Cd}$  is shown in Fig. 5.6. In total 19  $\gamma$  transitions were observed for this nucleus confirming all the previously assigned transitions [52, 53, 57].

The singles gamma-ray spectra with time windows of 7-11  $\mu\text{s}$  and 380 ns-3  $\mu\text{s}$  after the implantation of  $^{125}\text{Cd}$  were constructed to look for indications of more than one isomeric state in the decay. Relative intensities of all the observed transitions originating from the levels populated in the decay of same isomeric state are expected to be similar during any time interval

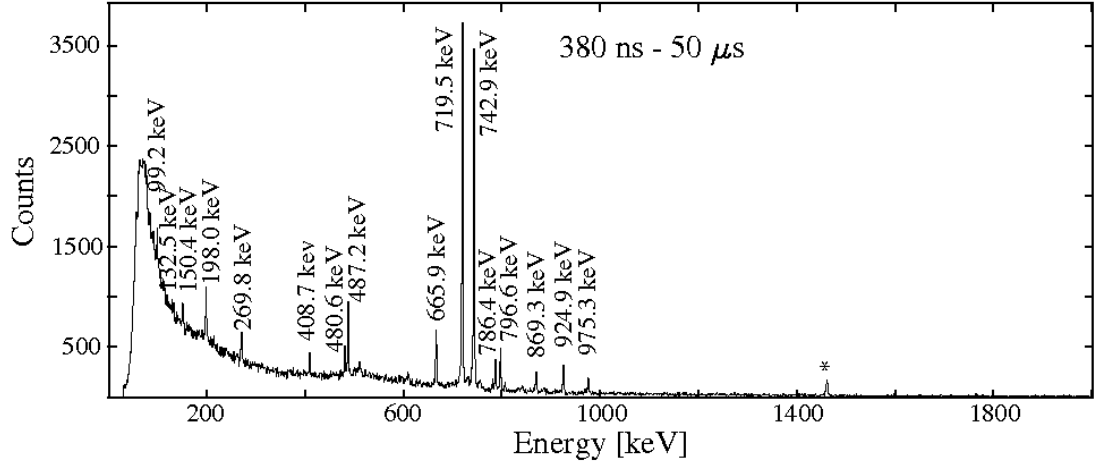


Figure 5.6: Singles gamma-ray energy spectrum of  $^{125}\text{Cd}$  for the full time range of  $50\ \mu\text{s}$  excluding the prompt flash.

of the measurement. A difference in the intensities of the 99.2 keV, 132.5 keV, 150.4 keV, 198.0 keV, 269.8 keV, 408.7 keV, 480.6 keV, 786.4 keV and 869.3 keV relative to the 742.9 keV gamma line in two spectra with different time windows (see Fig. 5.7) indicates that these gamma lines have different isomeric feeding as compared to the ones shown in Fig. 5.7(top). In addition, this analysis gives an estimate of the lifetime of isomeric states present in the decay. The transitions at energy 99.2 keV, 132.5 keV, 150.4 keV, 198.0 keV, 269.8 keV, 408.7 keV, 480.6 keV, 786.4 keV and 869.3 keV are most likely to be fed by an isomer having a lifetime of less than  $7\ \mu\text{s}$ , whereas the transitions at 487.2 keV, 665.9 keV, 719.5 keV, 742.9 keV, 924.9 keV and 975.3 keV originate from a state with a lifetime greater than  $11\ \mu\text{s}$ . The possibility of more isomeric states with similar lifetimes can not be excluded at this point. The relative intensities of all the observed  $\gamma$  transitions in time window of  $50\ \mu\text{s}$ , normalized to the 742.9 keV line are summarized in Table 5.3. The 77.2 keV transition was barely visible above background in the singles spectrum and hence to extract its relative intensity the  $\gamma\gamma$ -coincidence spectrum gated on 665.9 keV was used. The ratio of intensities of the 796.6 keV and 77.2 keV transitions in the aforementioned coincidence spectrum, corrected for their respective efficiencies was normalized to the intensity of 796.6 keV line obtained from the singles spectrum. Same procedure was repeated in the case of 587.2 keV transition observed in coincidence with 132.5 keV and 150.4 keV

transitions and the 719.0 keV transition in coincidence with the intense 719.5 keV gamma line. The two most intense  $\gamma$  lines at 719.5 keV and 742.9 keV were assigned to feed the ground state.

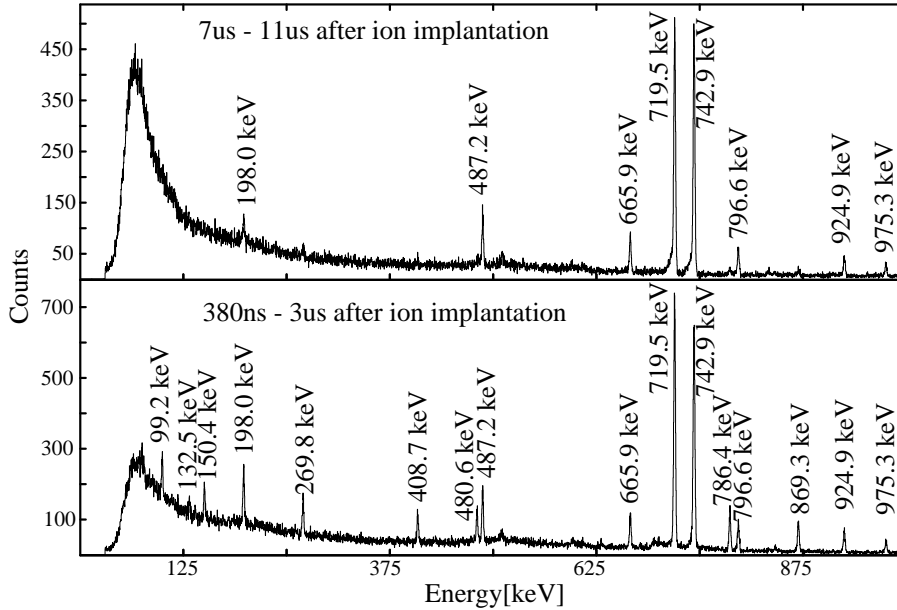


Figure 5.7: The singles gamma-ray energy spectra for  $^{125}\text{Cd}$  with time windows of 7 to 11  $\mu\text{s}$  (top) and 380 ns to 3  $\mu\text{s}$  (bottom) after the ion implantation.

The decay structure of intermediate spin levels in  $^{125}\text{Cd}$  is very similar to that of  $^{127}\text{Cd}$ . The 796.6 - 665.9 keV cascade is placed parallel to the 719.5 - 742.9 keV cascade due to its similarity with the two parallel competing branches in  $^{127}\text{Cd}$ . The argument is strongly supported by the intensity balance and experimental observation of mutual prompt coincidences with  $\Delta t < 200$  ns between the 796.6 keV and 665.9 keV transitions (see Fig. 5.8) and the 719.5 keV and 742.9 keV transitions (see Fig. 5.9). Similarity of the sum of energies of 796.6 - 665.9 keV lines to that of 719.5 - 742.9 keV lines seconds the above assignment.

The 77.2 keV transition observed in prompt coincidence with the 719.5 keV and 665.9 keV transition connects the two parallel cascades, with the difference of energies of 796.6 keV and 719.5 keV transitions and 742.9 keV and 665.9 keV transitions being 77.2 keV. The ordering of 719.5 keV transition with respect to 742.9 keV transition and of 796.6 keV transition with respect to the 665.9 keV transition could not be determined from the experimental data. Therefore, the level at an energy of 797 keV shown in Fig. 5.19

*Table 5.3:* Summary of the relative gamma intensities and half-lives of isomeric states in  $^{125}\text{Cd}$ , obtained by fitting the time distributions of individual gamma transitions. The gamma intensities are obtained for an open time condition and are normalised to the 742.9 keV transition. Low statistics of 77.2 keV, 132.5 keV, 587.2 keV and 719.0 keV gamma lines did not allow to extract their time distributions.

$E_\gamma$ [keV]	$T_{1/2}$ [ $\mu\text{s}$ ]	$I_\gamma$ [%]
77.2(2)	-	1.6(3)
99.2(2)	2.7(2)	8.0(9)
132.5(2)	-	1.6(4)
150.4(1)	3.1(2)	2.8(3)
198.0(8)	-	3.5(2)
269.8(1)	3.1(2)	3.9(3)
408.7(1)	3.0(2)	4.0(3)
480.6(1)	3.1(2)	5.0(3)
487.2(1)	13.6(6)	15.8(6)
587.2(2)	-	1.2(3)
665.9(1)	13.7(6)	13.6(6)
719.0(10)	-	0.8(4)
719.5(1)	13.6(3)	103.6(32)
742.9(1)	13.6(3)	100(31)
786.4(1)	3.1(1)	8.4(4)
796.6(1)	13.8(7)	11.5(5)
869.3(1)	3.1(2)	6.6(4)
924.9(1)	14.2(8)	9.9(4)
975.3(1)	14.0(12)	5.4(3)

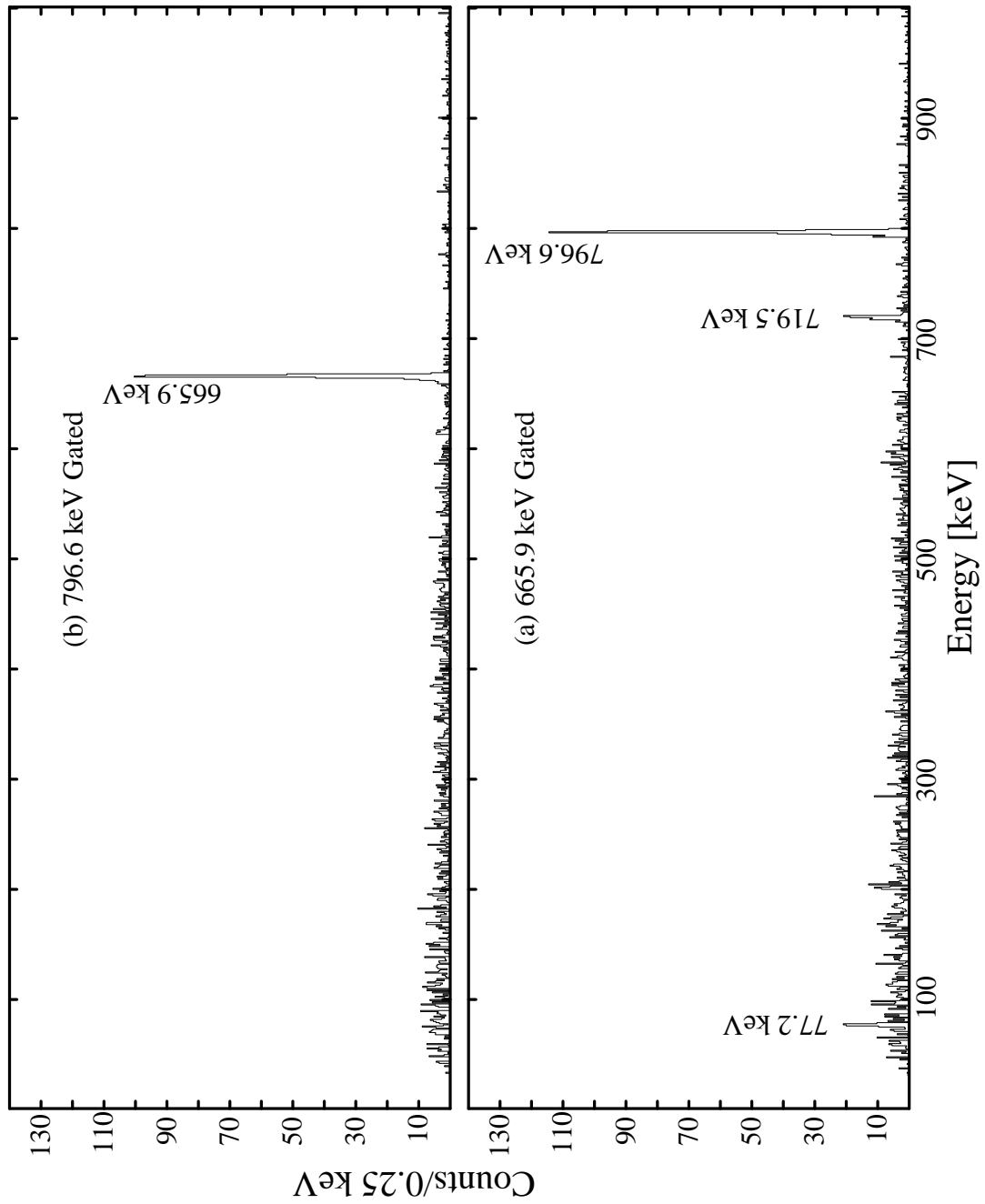


Figure 5.8:  $\gamma\gamma$ -coincidence relations of 665.9 keV (a) and 796.6 keV (b) transitions. The coincidence time condition is  $\Delta t < 200$  ns.

can be at 666 keV and the one at 743 keV can be at 720 keV instead. This uncertainty is similar to the ambiguity in the energy of  $(15/2)^-$  and  $(13/2)^-$  states in  $^{127}\text{Cd}$ . For clarity of discussion, the referred level energies in  $^{125}\text{Cd}$  are with respect to  $(11/2)^-$  state (see Fig. 5.19) which is at an energy of  $\sim 300$  keV above the ground state. A third cascade formed by the 487.2 keV, 975.3 keV and 924.9 keV transitions parallel to the main 719.5 - 742.9 keV branch is observed additionally. The prompt  $\gamma\gamma$ -coincidence spectrum of 487.2 keV  $\gamma$  transition is shown in Fig. 5.10(a). Strong coincidence of 487.2 keV gamma ray with 975.3 keV and the 924.9 keV transitions allowed to place them in sequence. However, no coincidence between the 975.3 keV and 924.9 keV transitions (see Fig. 5.10) suggests that they are parallel to each other. Therefore, an intermediate level at 975 keV fed by the 487.2 keV  $\gamma$  line and decaying through a competition between the 975.3 keV transition and a nonobserved 50 keV transition is proposed (see Fig. 5.19). The 487.2 keV transition was assigned to decay from the level at 1462 keV, same as 719.5 keV gamma ray (see Fig. 5.19) because of their similar time distributions and due to the sum of energies of 487.2 - 975.3 keV branch being equal to that of the 719.5 keV and 742.9 keV cascade. The placement of states at 975 keV and 925 keV is fixed based on the fact that a low-lying first excited state at 487.2 keV is not expected in this nucleus according to the systematics of neighbouring  $^{127,128}\text{Cd}$  isotopes [59, 6].

The delayed  $\gamma\gamma$ -coincidence relations of 719.5 keV and 742.9 keV transitions with no limit on the coincidence time are shown in Fig. 5.11. Weak coincidences with 99.2 keV, 132.5 keV, 150.4 keV, 198.0 keV, 269.8 keV, 408.7 keV, 480.6 keV, 786.4 keV and 869.3 keV gamma lines are visible in both of the spectra.

However, prompt coincidences of 719.5 keV and 742.9 keV transitions (see Fig. 5.9) show no signs of the above mentioned  $\gamma$  rays. Thus, the isomeric states feeding the two sets of transitions were concluded to be different. To place the 99.2 keV, 132.5 keV, 150.4 keV, 198.0 keV, 269.8 keV, 408.7 keV, 480.6 keV, 587.2 keV, 719.0 keV, 869.3 keV and the 786.4 keV transitions in the decay scheme, their coincidence relations were analysed for two coincidence time conditions of  $\leq 200$  ns and  $\leq 50$   $\mu\text{s}$ . The 99.2 keV and 786.4 keV transitions are in coincidence with all other  $\gamma$  lines shown in Fig. 5.12 and thus form a single cascade, with 99.2 keV being the primary transition, depopulating the isomer. Rest of the  $\gamma$  lines were placed in parallel branches based on the following arguments:

Absence of coincidence of the 269.8 - 408.7 keV cascade with the 198.0 - 480.6 keV cascade indicated that they form two parallel branches (see Fig. 5.13). This assignment was supported by the fact that the energies of 269.8 keV and 408.7 keV  $\gamma$  lines add to the same sum as 198.0 keV and 480.6 keV

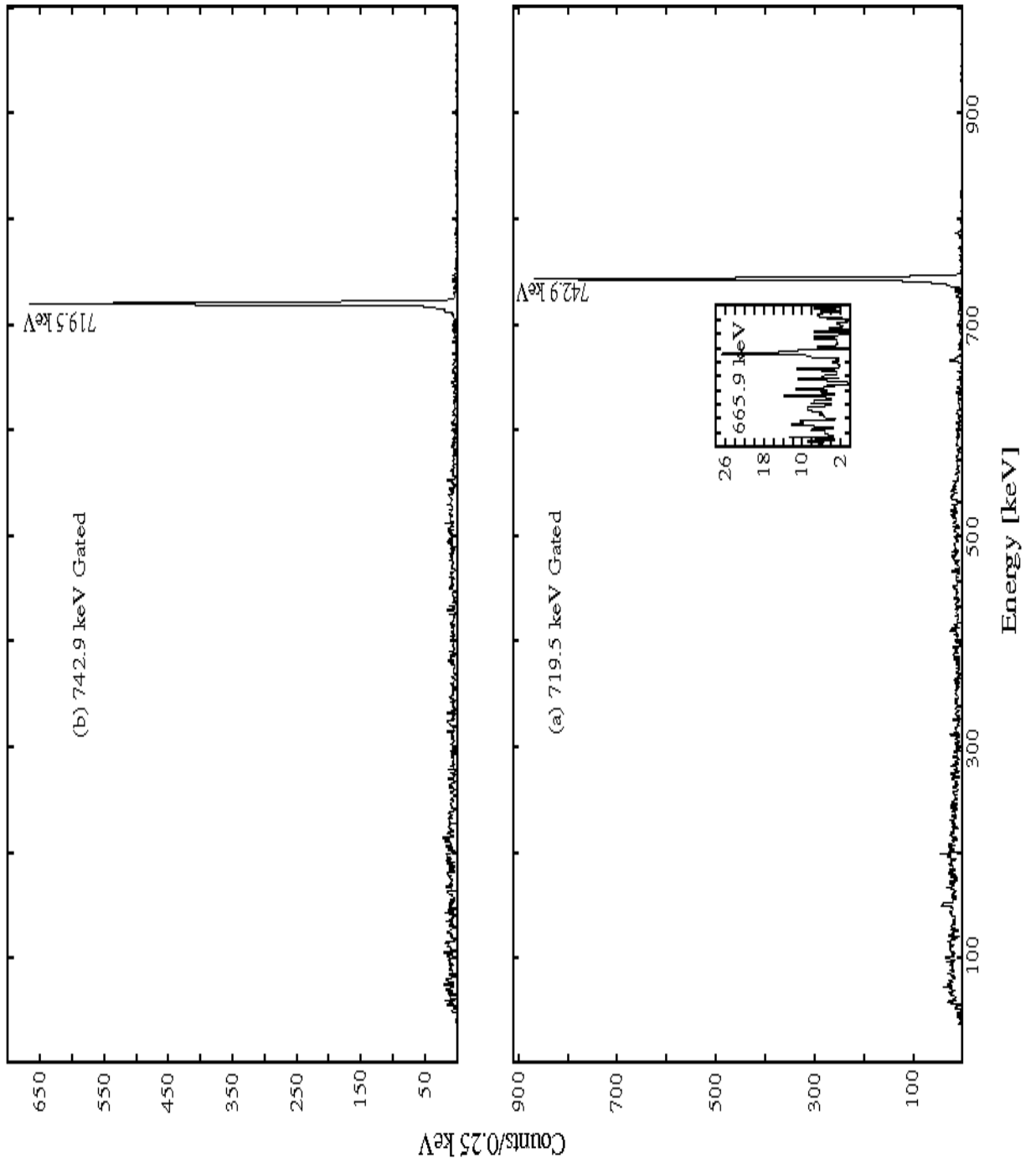


Figure 5.9: Prompt  $\gamma\gamma$ -coincidence spectra gated on 719.5 keV (a) and 742.9 keV (b) transitions. Weak lines are shown in inset.

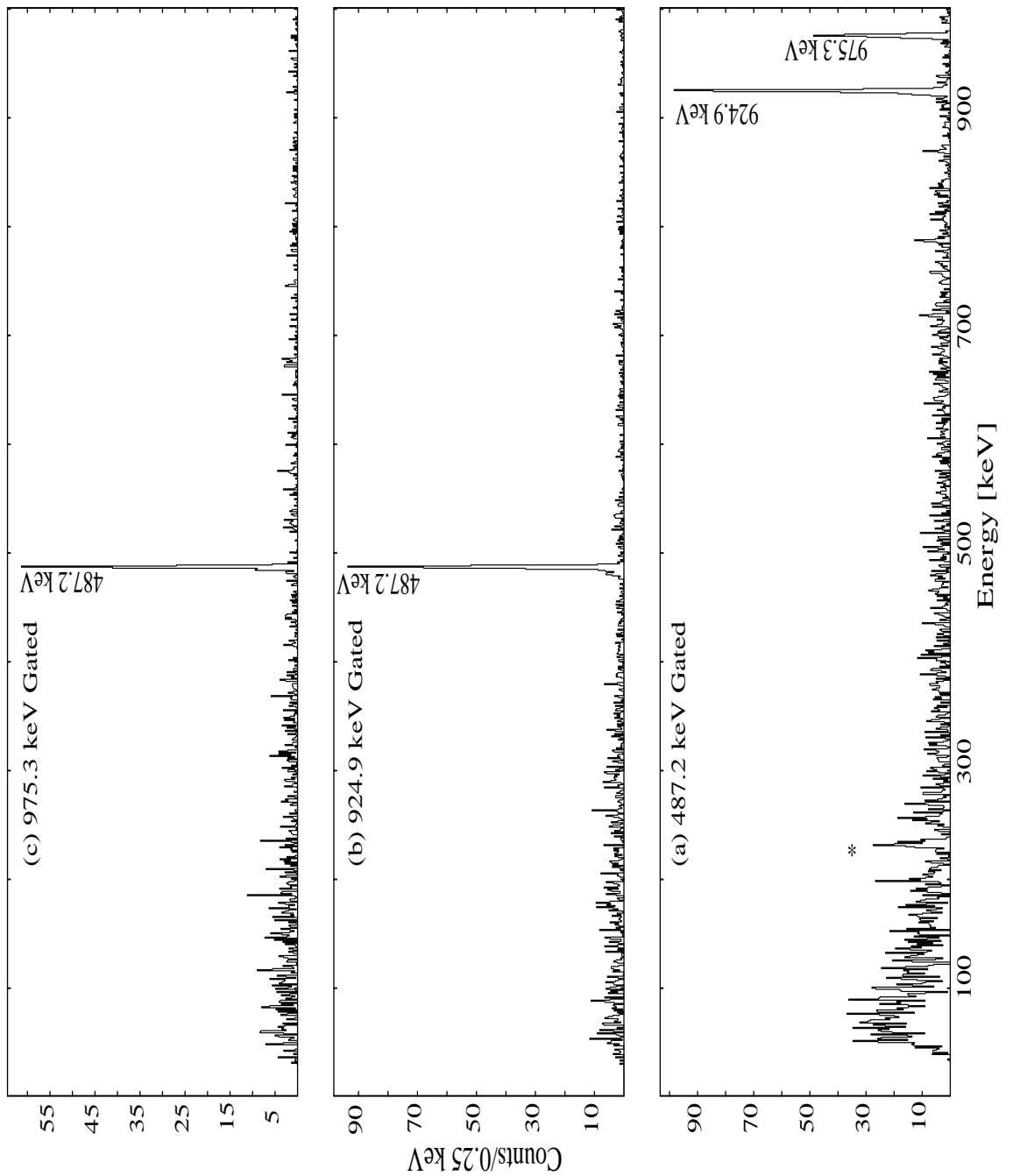


Figure 5.10:  $\gamma$ - $\gamma$ -coincidence spectra gated on 487.2 keV (a), 924.9 keV (b) and 975.3 keV (c). The coincidence window is less than 200 ns.

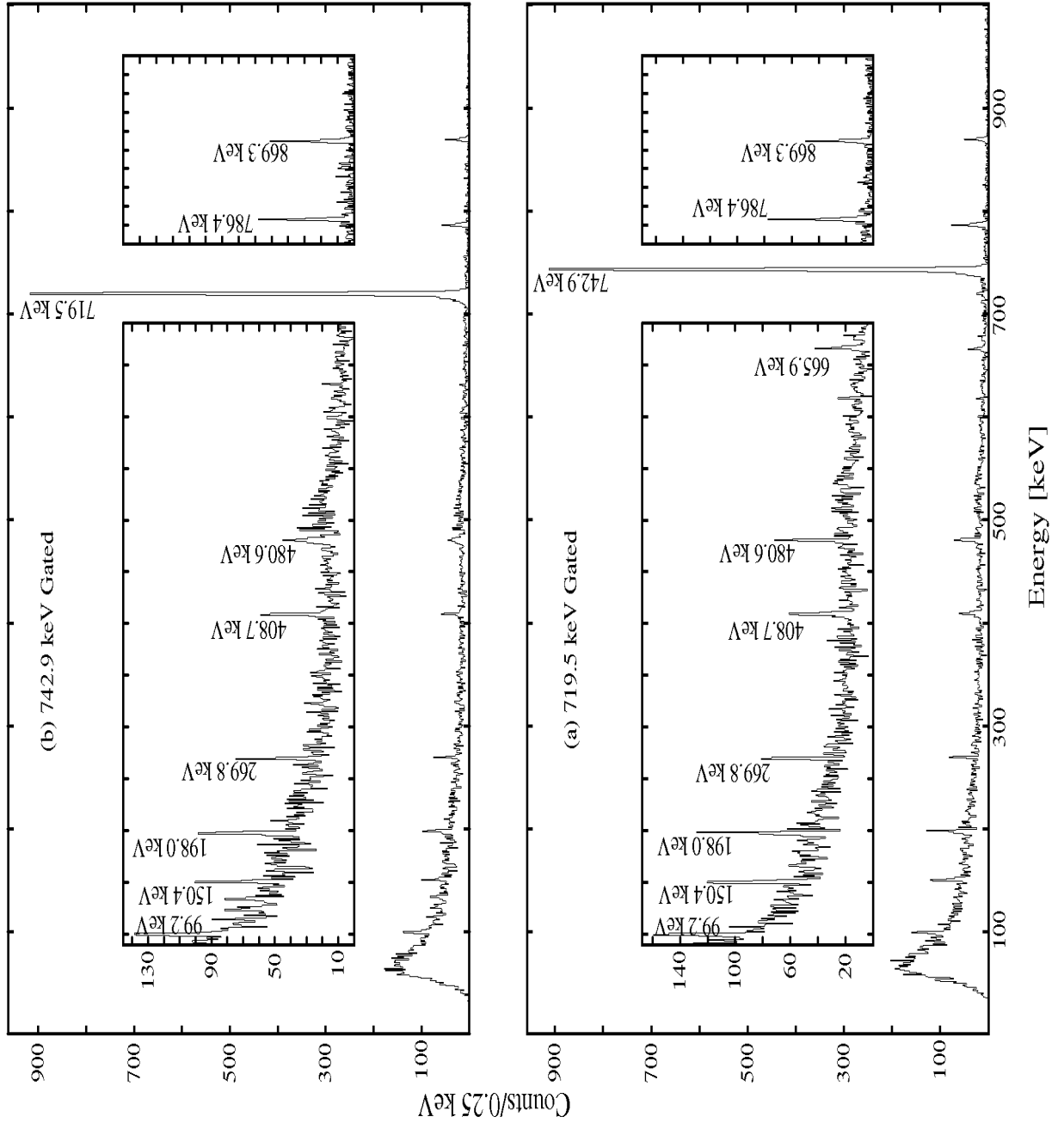


Figure 5.11:  $\gamma\gamma$ -coincidence spectra gated on 719.5 keV (a) and 742.9 keV (b) with an open coincidence time condition.

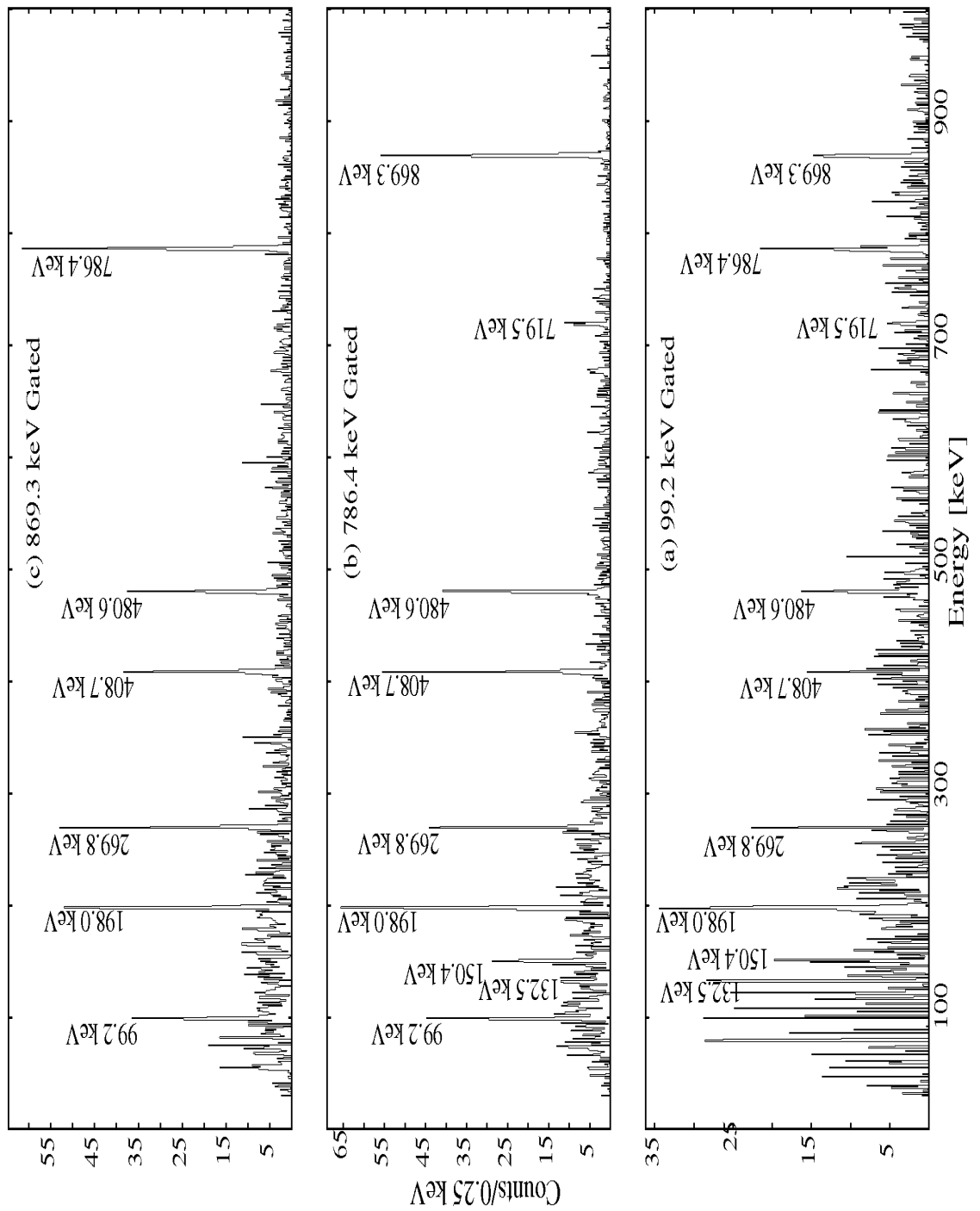


Figure 5.12:  $\gamma\gamma$ -coincidence spectra gated on 99.2 keV (a), 786.4 keV (b) and 869.3 keV (c) transitions. The coincidence window is less than 200 ns.

transitions. Similarly the energies of 587.2, 132.5 and 150.4 keV transitions add up to 870 and hence, were placed parallel to the 869.3 keV line.

The ordering of 786.4 keV transition with respect to 869.3 keV and its parallel transitions could not be affirmed, which again results in the ambiguous energies of three levels between 2141 keV and 3796 keV (see Fig. 5.19). The ordering of 269.8 - 408.7 keV gamma cascade and 198.0 - 480.6 keV cascade with respect to the 99.2 - 786.4 - 869.3 keV branch is based on asymmetry observed in the relative time distributions of 198.0 keV and 269.8 keV transitions with respect to 786.4 keV and 869.3 keV gamma lines as shown in Fig. 5.14. Although the statistics in each of the spectra is very low to make any firm conclusions, the direction of centroid shift forward in time for all the distributions indicate that the latter two transitions were emitted before. In addition, this indicates towards the presence of a state associated with these transitions having a half-life small enough to show no noticeable differences in the relative intensities of  $\gamma$  transitions shown in Fig. 5.7. To extract this half-life, the centroid shift analysis explained in section 4.3.4.3 on page 60-62 was adopted.

The reference zero time of  $\gamma$ -ray emission was set by the centroids of the distribution of prompt flash with gates on energies lying in the range of 100 keV to 1000 keV. Obtained dependence of the zero time on  $\gamma$ -ray energy is shown in Fig. 5.15(a). The shift in centroids of prompt gamma transitions below the energies of 400 keV is the consequence of walk effect. As the 719.5 keV and 742.9 keV  $\gamma$  transitions are in prompt coincidence, the centroid of their relative time distribution lies on the reference zero time line (see Fig. 5.15(a)). Relative time distributions of 198.0 keV, 269.8 keV, 408.7 keV and 480.6 keV transitions with respect to 786.4 keV  $\gamma$  line were added to the analog distributions with respect to 869.3 keV  $\gamma$  line to increase the statistics. The centroids of all the four distributions show a shift with respect to the zero time line (see Fig. 5.16). The observed shifts in the centroids in time units are listed in Table 5.4 .

To look more precisely into this issue, the relative time distributions of 269.8 keV line with 408.7 keV and of 198.0 keV with 480.6 keV transition were constructed. The respective shift in both of the centroids were of the same order. The spectra are shown in Fig. 5.17. This observation is believed to be a consequence of walk between the 198.0 keV, 480.6 keV transitions and the 269.8 keV, 408.7 keV transitions, respectively because it is less likely for an isomeric state with a half-life of the order of few nanoseconds to decay via the transitions with energies around 400 keV. Hence, it was concluded that the state decaying by a competition between the 269.8 keV and 198.0 keV transitions possesses a lifetime of 2.5(15) ns and is the cause of the asymmetry in the relative time distributions of the 269.8 keV, 408.7 keV,

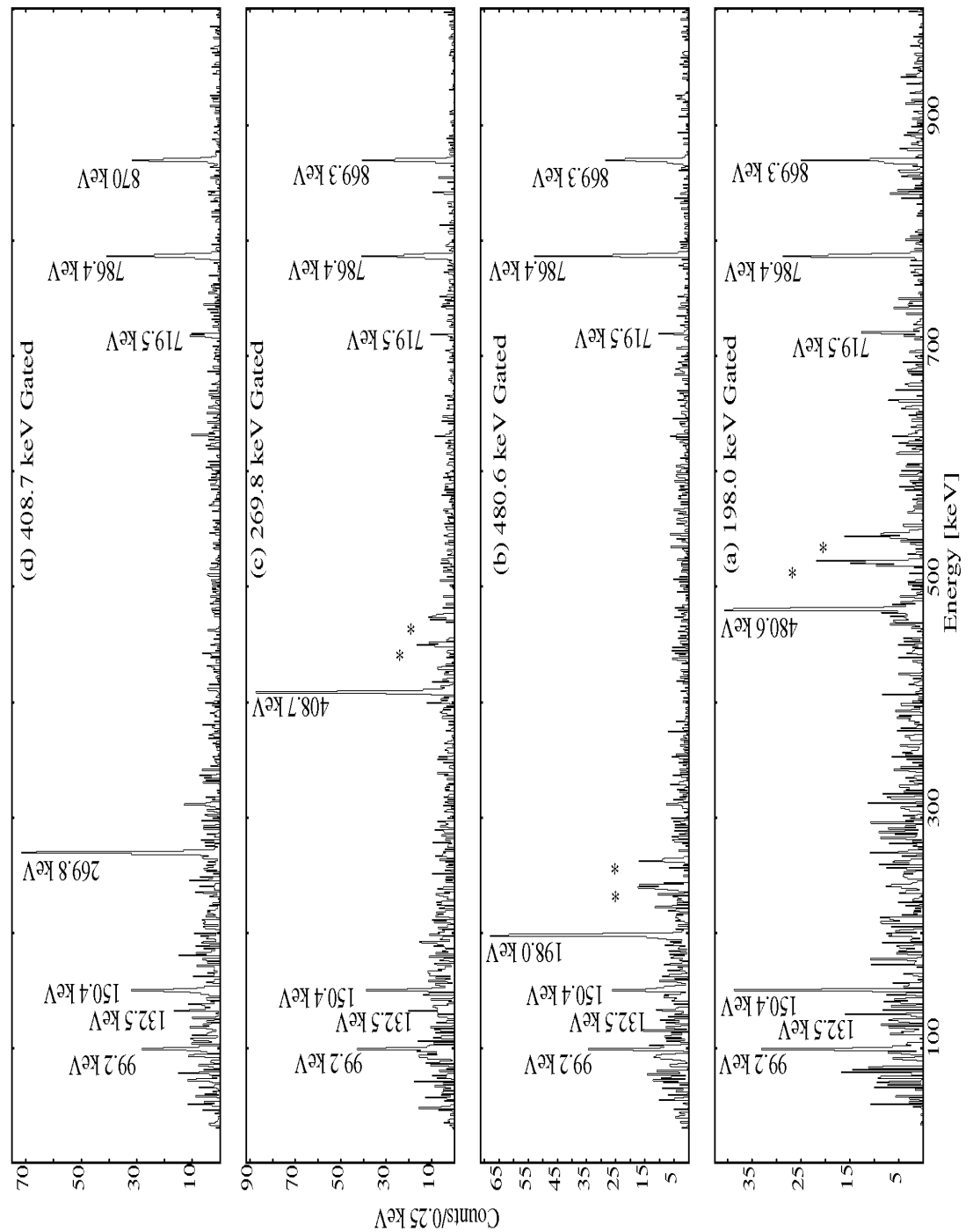


Figure 5.13: Prompt  $\gamma$ - $\gamma$ -coincidence spectra gated on 198.0 keV (a), 480.6 keV (b), 269.8 keV (c) and 408.7 keV (d) transitions.

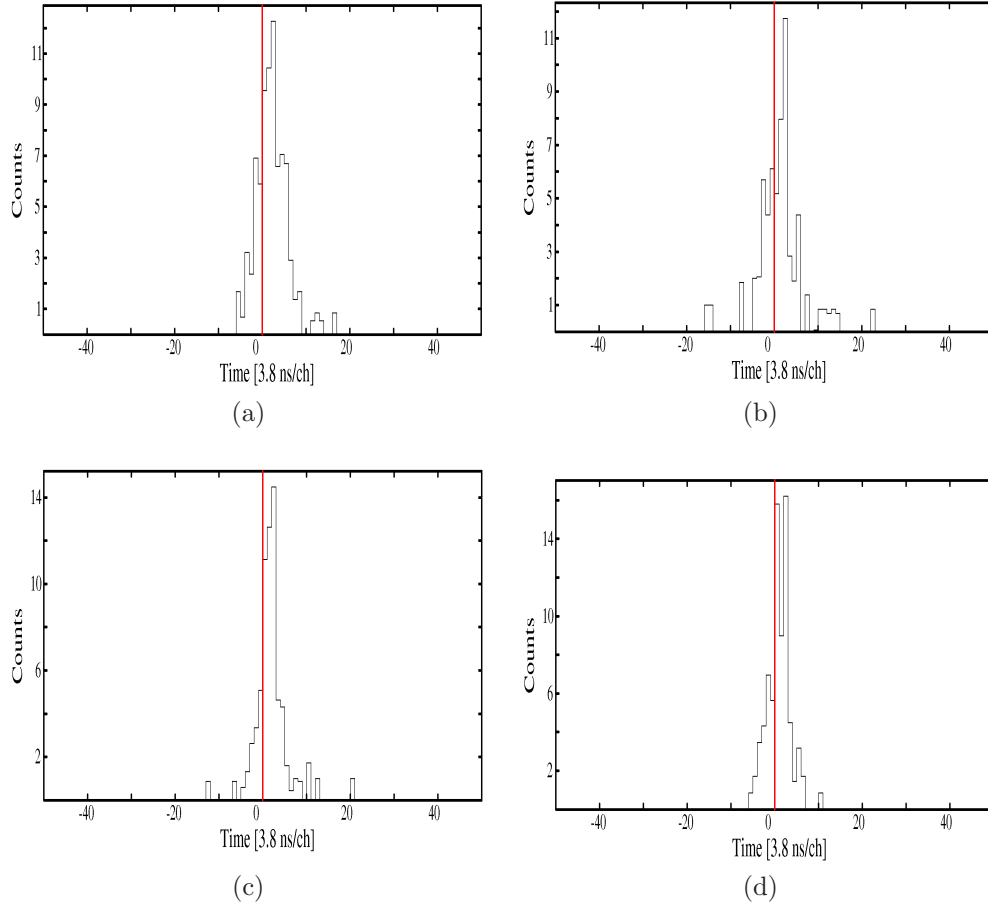
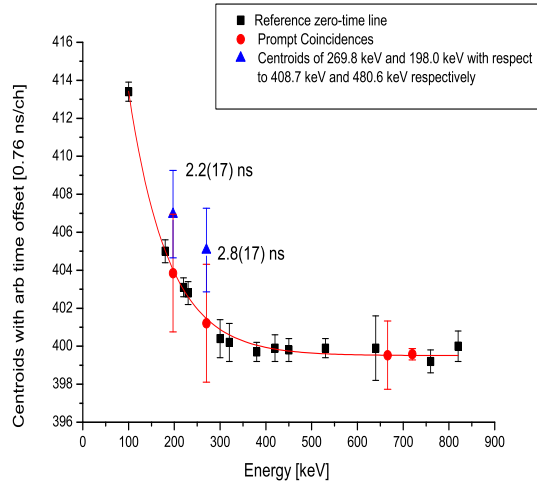


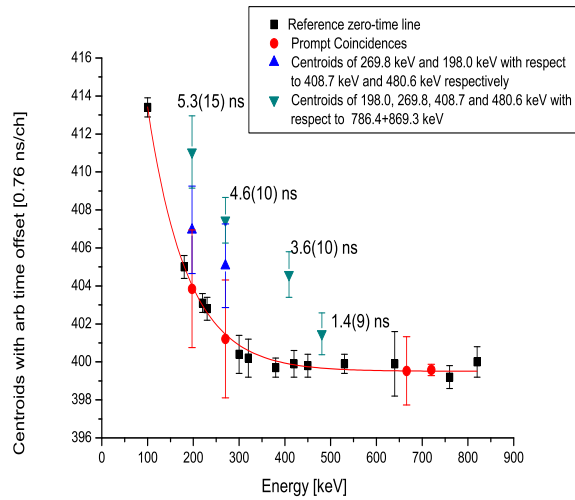
Figure 5.14: (a) and (b): Time distribution of 198.0 keV transition relative to the 786.4 keV  $\gamma$  line and the 869.3 keV  $\gamma$  line, respectively. (c) and (d): Time distribution of 269.8 keV transition relative to the 786.4 keV  $\gamma$  line and the 869.3 keV transition, respectively. The red line represents the zero time. Centroids of all the distributions are shifted forward in time indicating the emission of 786.4 keV and 869.3 keV  $\gamma$  lines before the 198.0 keV and 269.8 keV transitions.

198.0 keV and 480.6 keV transitions with respect to 786.4 keV and 869.3 keV transitions.

Based on all the arguments above and the mentioned uncertainties in the ordering of gamma transitions, three possible scenarios (EXP-I, EXP-II and EXP-III) are proposed for the level scheme of  $^{125}\text{Cd}$  as shown in Fig. 5.19. To obtain the half-life values of other two longer living isomers, the intensity distributions of observed  $\gamma$  transitions (wherever possible) were extracted as



(a)



(b)

Figure 5.15: (a): The reference zero time line (in red) and the shifts in centroids of relative time distributions of 198.0 keV and 269.8 keV transitions with respect to the 408.7 keV and 480.6 keV transitions, respectively, in time units. (b) is similar to (a) with an addition of centroid shifts of relative time distribution between the 198.0 keV, 269.8 keV, 408.7 keV and 480.6 keV transitions and 786.4 keV and 869.3 keV transitions.

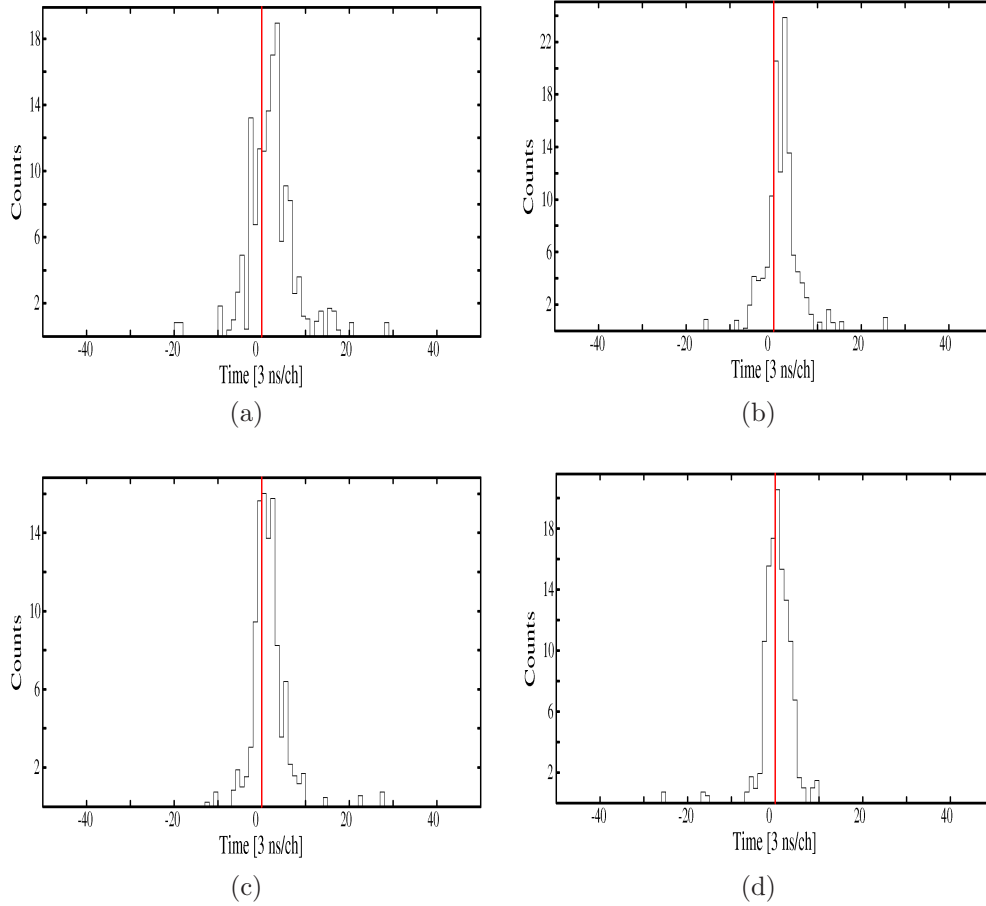


Figure 5.16: The time distribution of 198.0 keV transition (a), 269.8 keV transition (b), 408.7 keV transition (c) and 480.6 keV transition (d) relative to 786.4 keV  $\gamma$  line added to the analog distributions relative to 869.3 keV  $\gamma$  line.

a function of time. A single exponential decay fit was performed on the time distributions of 99.2 keV, 150.4 keV, 269.8 keV, 408.7 keV, 480.6 keV, 786.4 keV and 869.3 keV lines. Due to lower statistics, lifetime analysis could not be done for 132.5 keV, 587.2 keV and the 719.0 keV transitions. Proximity of the 197.1 keV background line forbid to obtain a reasonable background free time distribution of 198.0 keV which in turn did not allow to extract the half-life from the time distribution of this transition. Values of the half-life of decaying isomer obtained from the fit of time distributions of individual  $\gamma$  lines are listed in Table 5.3. The adopted value of the half-life for the level at 3896 keV is  $3.1(1) \mu\text{s}$ , extracted from the sum of the time distributions of 99.2

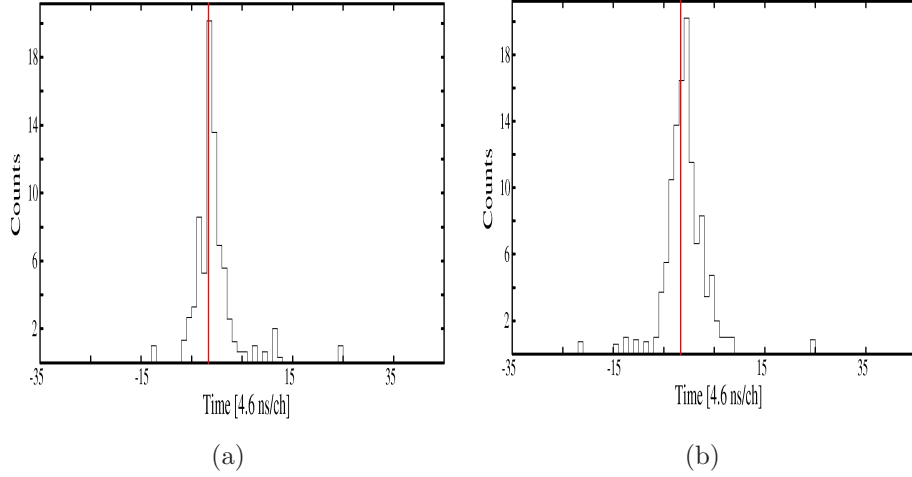


Figure 5.17: (a): Time distribution of 198.0 keV transition relative to 480.8 keV  $\gamma$  line. (b): Time distribution of 269.8 keV transition relative to 408.7 keV  $\gamma$  line.

keV, 150.4 keV, 269.8 keV, 408.7 keV, 480.6 keV, 786.4 keV and 869.3 keV lines. This value was introduced as a constant in two component exponential decay function to explain the decay curves of  $\gamma$  lines originating from the lower isomer. The fit of time distributions of the 719.5 keV, 742.9 keV, 796.6 keV, 665.9 keV, 497 keV, 924.9 keV and 975.3 keV transitions with this two component exponential decay function yielded comparable half-lives for the isomeric state at 1462 keV (see Table 5.3). The adopted value is  $13.6(2) \mu\text{s}$ .

The assignment of spins and parities to the excited states and multiplicities to the observed  $\gamma$  transitions was based on the lifetime information, the reduced transition probabilities and the systematics of neighbouring odd-mass Cd and Sn isotopes [59, 54]. Both gamma-decaying isomers in  $^{125}\text{Cd}$  are built on the  $(11/2^-)$  state. Similar to  $^{127}\text{Cd}$  [59], the  $(11/2^-)$  state in  $^{125}\text{Cd}$  is also a  $\beta^-$  decaying isomer at about an estimated energy of 300 keV above the known  $(3/2^+)$  ground state [55]. Due to the large spin difference between  $(11/2^-)$  and  $(3/2^+)$  states, the gamma cascade ends at  $(11/2^-)$  state which is therefore considered as the reference level in this work and the energies of all the excited states are quoted with respect to it. The observed decay of the state at 1462 keV energy in  $^{125}\text{Cd}$  corresponds to the decay pattern of  $(19/2^+)$  isomer in  $^{127}\text{Cd}$  with two additional states at 925 keV and 975 keV, respectively in the former nucleus. Therefore, the isomeric state at 1462 keV in  $^{125}\text{Cd}$  was assigned to a spin-parity of  $(19/2^+)$ . This level de-

Table 5.4: The shift in the centroid of relative time distributions from the reference zero time.

$E_\gamma$ [keV]	Centroid shift		
	[ns]		
198.0(8)	5.3(15) <sup>a</sup>	2.2(17) <sup>b</sup>	-
269.8(1)	4.6(10) <sup>a</sup>	-	2.8(17) <sup>c</sup>
408.7(1)	3.6(10) <sup>a</sup>	-	-
480.6(1)	1.4(9) <sup>a</sup>	-	-

<sup>a</sup> With respect to the 786.4 and 869.3 keV transitions.

<sup>b</sup> With respect to the 408.7 keV gamma line.

<sup>c</sup> With respect to the 480.6 keV gamma line.

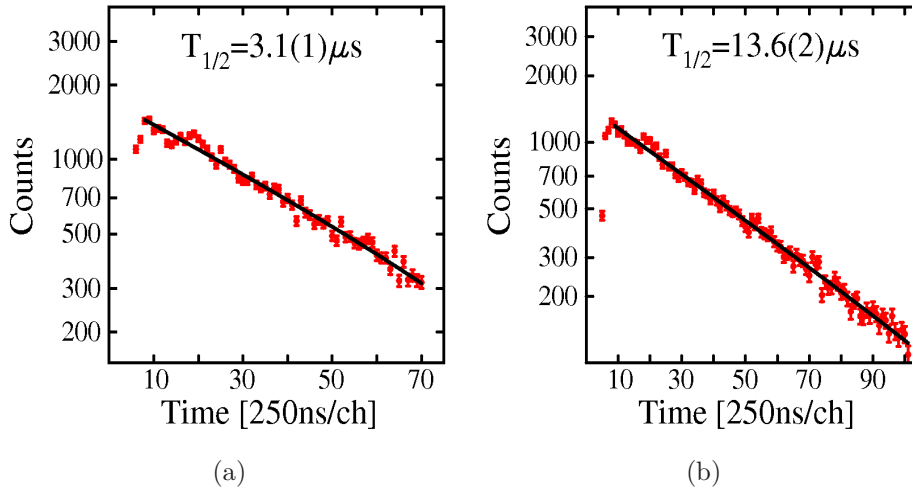


Figure 5.18: (a): Sum of time distributions of the 269.8, 408.7, 480.6, 786.4 and 869.3 keV transitions with a single exponential decay fit. (b): Sum of time distributions of the 719.5 keV and the 742.9 keV transitions originating from the isomeric state at 1462 keV with a two-component exponential decay fit.

Table 5.5: Experimental reduced transition strengths for  $\gamma$  rays decaying from the state at 1462 keV. Separate values are given for the alternative placements of the 719.5/742.9 keV and 796.6/665.9 keV transitions. The 487.2 keV transitions can possess either an  $E3$  or an  $M2$  character, values for both the multiplicities are listed.

$E_\gamma$	Transition	$\sigma L$	B( $\sigma L$ ) (W.u)
[keV]	$J \rightarrow I$		EXP
487.2(1)	$(19/2^+) \rightarrow (15/2^-)_2$	$M2^a$	$3.91(25) \times 10^{-4}$
	$(19/2^+) \rightarrow (13/2^-)_2$	$E3^a$	1.75(11)
719.5(1)	$(19/2^+) \rightarrow (15/2^-)_1$	$M2^a$	$3.72(7) \times 10^{-4}$
796.6(1)	$(19/2^+) \rightarrow (13/2^-)_1$	$E3^a$	$4.26(27) \times 10^{-2}$
742.9(1)	$(19/2^+) \rightarrow (15/2^-)_1$	$M2^a$	$3.09(20) \times 10^{-4}$
665.9(1)	$(19/2^+) \rightarrow (13/2^-)_1$	$E3^a$	$1.82(11) \times 10^{-1}$

<sup>a</sup> Pure transition assumed.

cays by a competition between three transitions at energies 719.5(742.9) keV, 796.6(665.9) keV and 487.2 keV. In analogy to <sup>127</sup>Cd, the observed half-life of the  $(19/2^+)$  state in <sup>125</sup>Cd can be well explained by an  $M2$  and  $E3$  character of the 719.5(742.9) keV and 796.6(665.9) keV transitions, respectively. Similarity of the energies of these four transitions with  $\gamma$  rays depopulating the  $(19/2^+)$  isomer in <sup>127</sup>Cd, supports the above multipolarity assignment. The third competing gamma transition at 487.2 keV can have either  $M2$  or  $E3$  character in order to retain the isomerism with observed half-life of 13.6  $\mu$ s. The lower multiplicities would make this transition faster with a characteristic half-life of the decaying level less than 1 ns and higher multiplicities of  $M3$  or  $E4$  would make it so slow ( $T_{1/2} \sim 7$  s) that it would not be able to compete with the other two  $M2$  and  $E3$  transitions.

Hence, the spins and parities of  $(15/2^-)$  and  $(13/2^-)$  were assigned to the states at 797(666) keV and 720(743) keV. The reduced transition strengths extracted for three transitions depopulating the  $(19/2^+)$  state are listed in Table 5.5. The state at 975 keV was assigned to a spin and parity of  $(15/2^-)$  or  $(13/2^-)$  due to the discussed ambiguity in the multipolarity of 487.2 keV transition populating it. The 77.2 keV transition and the nonobserved 50 keV

transition should have  $M1$  character because any other multipolarity would result in a noticeable half-lives of the states depopulated by the emission of these low-energy transitions. This supports the spin and parity assignments of the levels at 743 or 720 keV and at 666 or 796 keV and results in  $(13/2^-, 11/2^{+,-})$  spins of the level at 925 keV. The presence of a lifetime of 2.5(15) ns for the level at 2141 keV indicated the most probable  $E2$  characters of both of the transitions depopulating it or a competition between an  $M1$  and an  $E1$  transition. The reduced  $E2$  transition strengths of 13.6(82) W.u for the 198.0 keV line and of 2.8(17) W.u for the 269.8 keV line were obtained, which agree well with the  $E2$  strengths observed in the similar energy range for nuclei in this region [54, 6]. If both the 198.0 keV and 269.8 keV transitions are parity conserving ( $E2$ ) transitions, the 480.6 keV and the 408.7 keV transitions should both be either of parity conserving or non-conserving nature in order to obtain a spin and parity of  $(19/2^+)$  for the lower isomer. With the experimental evidence of the states depopulated by both of them possessing no considerable half-life, they can be either two  $M1$ ,  $E1$  or  $E2$  transitions. Therefore, an ambiguity in spin and parity of the states above the  $(19/2^+)$  isomer remains. For the 786.4 keV transition the assumption of its multipolarity was based on its energy and the fact that its time distribution does not exhibit any distinct half-life. An  $M1$ ,  $E1$  or  $E2$  character explains such a behaviour. The 150.4 keV and 132.5 keV transitions are more likely to be two  $M1$  transitions due to their low energies combined with no noticeable half-lives of the two decaying states. Similarly, the energies of the 869.3 keV, 587.2 keV and 719.0 keV transitions limit the maximum multipolarity which they can possess to  $E2$ . In addition, as the parallel 719.0 keV and 587.2 keV transitions in EXP-II and EXP-III populate the states depopulated by 150.4 keV and 132.5 keV  $M1$  transitions, respectively, the parity change introduced ( $\Delta\pi = 0, 1$ ) by the decay of 869.3 keV, 719.0 keV and 587.2 keV transitions should be of the same nature. Same argument holds in EXP-I where the level at 3646 keV is fed by an  $M1$   $\gamma$  line at 150.4 keV. The observed branching ratios of the 869.3 keV, 587.2 keV and 719.0 keV competing transitions in EXP-II and EXP-III (Fig. 5.19) can be explained only if all of them have same multiplicities. The isomer at 3896 keV decays by a transition of 99.2 keV and a half-life of 3.1(1)  $\mu$ s. Only two possible multiplicities of  $E1$  or  $E2$  for the decaying transition can result in the measured half-life. An assumption of the  $E2$  character for this transition, results in a reduced transition strength of 0.20(1) W.u. The  $E2$  transitions with comparable energies forming isomers in the neighbouring neutron-rich Sn isotopes [54] have strengths of two orders of magnitude more than in  $^{125}\text{Cd}$ . However, the observation of a 69 keV  $E2$  transition in  $^{128}\text{Cd}$  with a reduced transition probability of 0.39(1) W.u [6] did not allow to exclude this

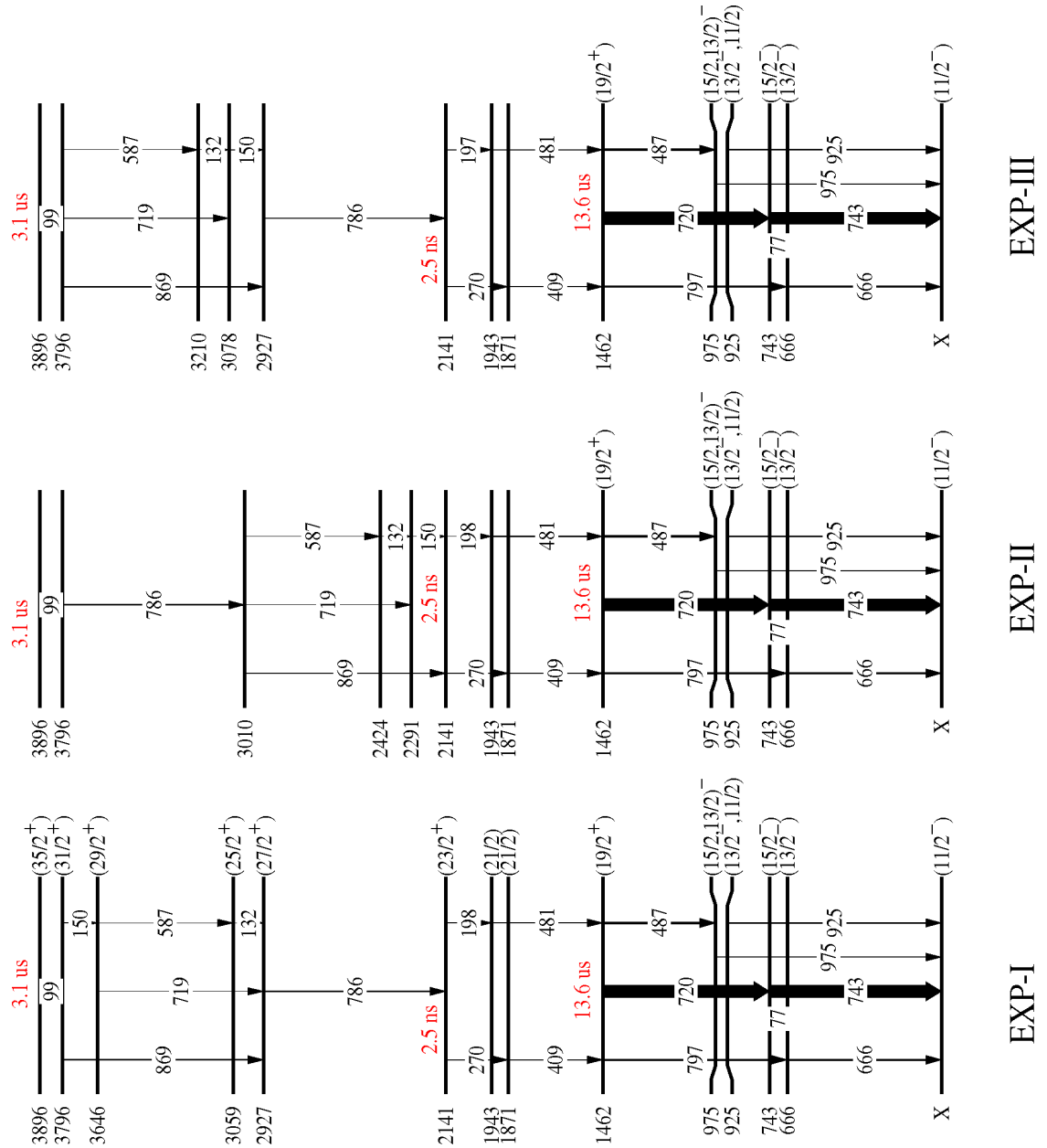


Figure 5.19: The proposed decay schemes for  $^{125}\text{Cd}$  with tentative spin and parity assignments of the excited states. The energies of the excited levels are with respect to the  $(11/2^-)$  state and the ordering of the states at 797 keV and 743 keV can be interchanged with 666 keV and 720 keV, respectively.

possibility. An alternate  $E1$  character for the 99.2 keV transition resulted in a  $B(E1)$  of  $7.58(25) \times 10^{-8}$  W.u. A tentative spin and parity assignments of the excited levels upto an energy of 1462 keV are shown in Fig. 5.19. Based on all the above mentioned arguments, a spin range of  $(33/2 - 43/2)$  was obtained for the higher-lying isomeric state at 3896 keV.

### 5.3 Isomeric ratios

Isomeric ratio is the fraction of population of an isomeric state during the production of a particular nucleus. Experimentally the isomeric ratio,  $R$  is calculated using the expression [60]

$$R = \frac{Y}{N_{imp}FG}, \quad (5.1)$$

where,  $Y$  is the number of gamma decays observed depopulating the isomer,  $N_{imp}$  is the number of implanted nuclei,  $F$  and  $G$  are correction factors for the decay losses during the flight path and limitation due to the finite detection time of gamma radiations, respectively. Total  $\gamma$ -decay yield,  $Y$  is given by

$$Y = \frac{N_\gamma(1 + \alpha_{tot})}{\epsilon_{eff}b_\gamma}, \quad (5.2)$$

where,  $N_\gamma$  represents the total number of counts in the photo peak of  $\gamma$  transition depopulating the isomeric state,  $\alpha_{tot}$  is the total internal conversion factor for this transition,  $\epsilon_{eff}$  is the absolute efficiency of the detector and  $b_\gamma$  is the branching ratio of the transition. The factors  $F$  and  $G$  are computed as

$$F = \exp \left[ - \left( \lambda^{q_1} \frac{TOF_1}{\gamma_1} + \lambda^{q_2} \frac{TOF_2}{\gamma_2} \right) \right], \quad (5.3)$$

$$G = \exp(-\lambda t_i) - \exp(\lambda t_f). \quad (5.4)$$

$\lambda^{q_1}$  and  $\lambda^{q_2}$  in expression (5.3) are the decay constants of ions in charge states  $q_1$  and  $q_2$ , respectively and  $t_i$  and  $t_f$  in (5.4) are the initial and final time of  $\gamma$ -acceptance window with  $t = 0$  defined by ion implantation excluding the prompt flash. In the present experiment the ions passing through the FRS were mainly fully stripped, hence the decay constant  $\lambda^0$  for neutralized nucleus was obtained using the experimentally measured decay constant as

$$\lambda^0 = \lambda \sum \frac{b_{\gamma i}}{1 + \alpha_{tot}}. \quad (5.5)$$

Table 5.6: Experimentally measured fraction of population of the isomeric states in <sup>125</sup>Cd and <sup>127</sup>Cd.

Nucleus	$I^\pi$	$E_i + x$	$E_\gamma$	$T_{1/2}$	$R_{exp}$
		[keV]	[keV]	[ $\mu s$ ]	
<sup>125</sup> Cd	(33/2 – 43/2) <sup>+, -</sup>	3896	99.2(2)	3.1(1)	0.010(4)
	(19/2 <sup>+</sup> )	1462	719.5(1)	13.6(2)	0.19(5)
<sup>127</sup> Cd	(19/2 <sup>+</sup> )	1560	738.8(2)	17.5(3)	0.15(4)

The index  $i$  here represents number of decay branches of the isomeric state.

$TOF_1$  and  $\gamma_1$  in eq. (5.3) are the time of flight and the corresponding Lorentz factor for ions in the first half of FRS (till S2), respectively and  $TOF_2$  and  $\gamma_2$  are similar quantities from S2 to S4.  $TOF_1$  and  $\gamma_1$  were calculated using the code MOCADI [61] and  $TOF_2$  and  $\gamma_2$  were determined experimentally.

When more than one isomeric state is populated in a nucleus with one partly fed by the other, the isomeric ratio of lower isomeric state is calculated using the expression [60]

$$R_L = \frac{Y_L}{N_{imp} F_L G_L} - b_{UL} \frac{R_U}{F_L G_L} \left[ \frac{\lambda_L G_U - \lambda_U G_L}{\lambda_L - \lambda_U} F_U + \frac{\lambda_U^0}{\lambda_L^0 - \lambda_U^0} G_L (F_U - F_L) \right], \quad (5.6)$$

where the indices  $L$  and  $U$  refer to the lower and upper states, respectively.

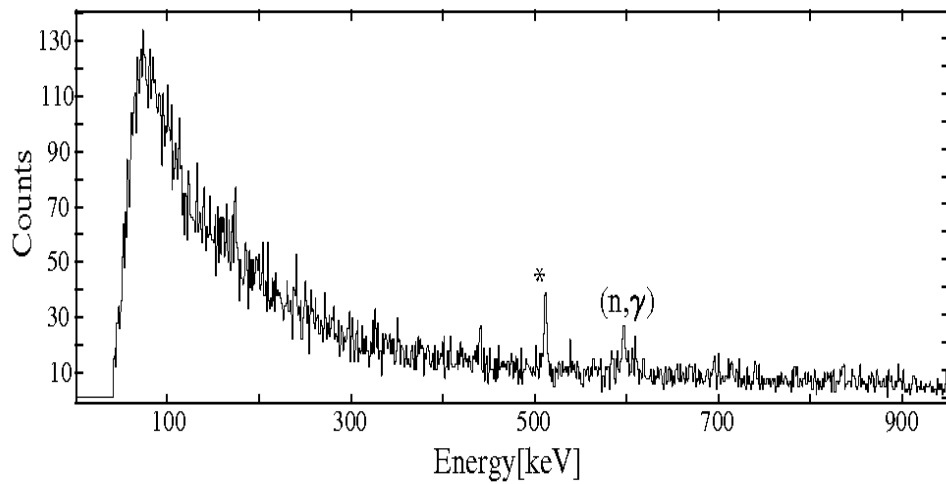
The experimental data on isomeric ratios obtained for <sup>125</sup>Cd and <sup>127</sup>Cd are given in Table 5.6. In both cases, statistics in the photo peak of the primary gamma transitions was good, hence main contribution in the quoted error is from the uncertainty in determining the number of implanted ions. For gamma transitions with energies < 400 keV,  $N_\gamma$  was corrected for the missing intensity due to the selection condition introduced to exclude prompt flash following the method described in section 4.3.4.1.

## 5.4 <sup>129</sup>Cd

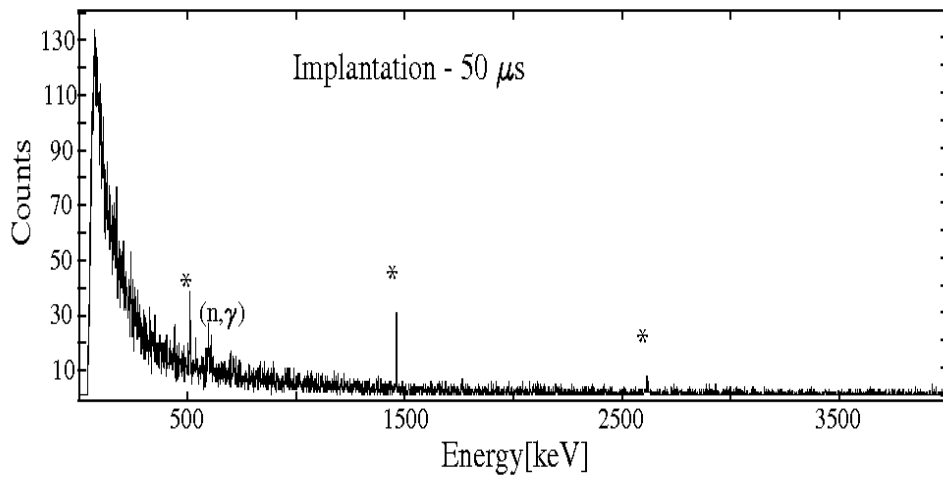
The  $\gamma$  decays in <sup>129</sup>Cd were not observed in the present experiment. Up to date only the spin-parity and the  $\beta^-$  decaying half-life of the ground state of

this nucleus is available [55]. In total,  $\sim 5 \times 10^4$   $^{129}\text{Cd}$  ions were identified at the FRS and a singles  $\gamma$ -ray spectrum containing only the background  $\gamma$  rays is shown in Fig. 5.20. As mentioned in chapter 3, ions with isomeric states living longer than few hundred nanoseconds can be further studied for isomer spectroscopy at the final focal plane of the FRS. However, if the number of implanted ions and the ratio of population of an isomeric state is high enough, isomers with half-lives smaller than 100 ns can also survive the flight path through the FRS and have been studied in previous experiments [62]. Other factors like hindered electronic conversion due to fully stripped ions and the isomeric cascades can lead to the observation of isomers with half-life values at the limit of electronic resolution. The shell-model calculations on  $^{129}\text{Cd}$  (explained in chapter 6, page 98-99) predict a  $\beta^-$  decaying spin-trap. The  $E3$  transition ( $27/2^- \rightarrow 21/2^+$ ) is strongly hindered due to the near-degeneracy of the  $27/2^-$  and  $21/2^+$  levels. Therefore, the isomer decays primarily by  $\beta^-$  emission and the  $\gamma$  decays are not observed experimentally for this nucleus. However, the systematics of neighbouring Cd ions suggest that the  $19/2^+$  state is isomeric. To set an upper limit on the half-life of such an isomeric state if present in  $^{129}\text{Cd}$ , an isomeric ratio of less than 17 % was considered. This value is the average of isomeric ratios obtained experimentally in  $^{125,127}\text{Cd}$  for the  $19/2^+$  state. According to the shell-model calculations competing transitions at  $\sim 300$  keV from ( $19/2^+ \rightarrow 15/2^-$ ) and at  $\sim 600$  keV from ( $19/2^+ \rightarrow 13/2^-$ ) depopulate the  $19/2^+$  state in  $^{129}\text{Cd}$ . The branching ratios obtained from energy scaling of such an  $M2$  transition of strength  $10^{-4}$  W.u and an  $E3$  transition of strength  $10^{-1}$  W.u are 67% and 33%, respectively.

A requirement of minimum 140 counts was set to distinguish the gamma peak at 300 keV depending on the background level in corresponding energy range in the singles  $\gamma$ -ray spectrum of  $^{129}\text{Cd}$ . With all these conditions and the expression (5.1) to calculate the isomeric ratio, an upper limit of  $\sim 93$  ns was set on the half-life of  $19/2^+$  state. This value depends on the isomeric ratio and the number of counts in the gamma peak. Varying the number of counts required to distinguish the gamma peak above background by 50 % also changes the half-life value of the state by 50%. Therefore, only if the energy of the decaying gamma transition decreases to around 50 keV, the high background levels would require more than 140 counts to identify the peak thereby increasing the half-life. In addition, a half-life of less than 93 ns cannot be supported by a decay of a  $\gamma$  transition with an  $M2$  character.



(a)



(b)

Figure 5.20: Singles  $\gamma$ -ray energy spectrum of  $^{129}\text{Cd}$  for an energy up to 1000 keV (a) and the full energy range of 4000 keV (b). Both of the spectra do not contain any characteristic  $\gamma$  lines from the decay of this nucleus. Background lines are marked with an asterisk (\*).



# Chapter 6

## Discussion

This chapter details the interpretation of the experimental spectroscopic data on odd Cd isotopes using the shell-model approach. The first section describes shell-model interaction used for the calculations. The theoretically obtained results are discussed in section 6.2. In the last section, the role of proton-neutron interaction in  $^{132}\text{Sn}$  region is summarized based on experimental and theoretical results.

### 6.1 Shell-model interaction

A model space of  $\pi(p_{1/2}, g_{9/2}) \nu(d_{5/2}, g_{7/2}, s_{1/2}, d_{3/2}, h_{11/2})$  outside a  $^{88}\text{Sr}$  core was chosen implying that the core excitations across the  $Z = 50$  and  $N = 82$  shells were not considered. The residual interaction is based on the G-matrix derived from the realistic CD-Bonn nucleon-nucleon interaction [63]. The core polarization corrections were incorporated for a  $^{88}\text{Sr}$  inert core following the many-body approach outlined in Ref. [29]. The resulting interaction was scaled by a factor of  $(88/132)^{-1/3}$  to adapt it to the  $^{132}\text{Sn}$  region. Monopole tuning of the two-body matrix elements (TBME) was performed to reproduce the single hole energies (SHE) in  $^{132}\text{Sn}$ . To increase the collectivity in the proton-neutron ( $\pi\nu$ ) shells, the dominating binding (negative) diagonal  $\pi\nu$  TBME  $\pi g_{9/2}\nu h_{11/2}$  and  $\pi p_{1/2}\nu h_{11/2}$  were enhanced by a monopole shift of -100 keV. To maintain the SHE for  $^{132}\text{Sn}$ , further tuning of the interaction was done to improve the agreement in the even Sn isotopes [64]. With these modifications, the calculated level schemes are referred to as SM for all the three isotopes. Effective charges  $e_\pi = 1.5e$  and  $e_\nu = 0.7e$  for protons and neutrons and spin  $g$ -factor of  $g_s = 0.7g_s^{free}$  for magnetic transitions were used [17, 54]. Calculations were performed with the OXBASH code [65].

For the special case of  $^{127}\text{Cd}$ , the results given by SM were also compared to a large-scale shell-model (LSSM) calculation using an extended model space of  $\pi(p_{3/2}, p_{1/2}, f_{5/2}, g_{9/2}) \nu(d_{5/2}, g_{7/2}, s_{1/2}, d_{3/2}, h_{11/2})$  outside  $^{78}\text{Ni}$  with an interaction derived from the CD-Bonn nucleon-nucleon potential using the same method as described above, but for an inert  $^{78}\text{Ni}$  core [6]. Monopole tuning was performed to reproduce the experimental SHE for  $^{132}\text{Sn}$  and levels in neighbouring Sn isotopes, the  $N = 82$  isotone,  $^{130}\text{Cd}$  and the  $\pi^{-1}\nu^{-1}$  neighbour,  $^{130}\text{In}$ . Effective charges of  $1.5e$  for protons and  $0.5e$  for neutrons were used for electric transitions and an effective spin  $g$ -factor of  $g_s = 0.75g_s^{free}$  for magnetic transitions were utilized. In addition orbital  $g$ -factors of  $g_l(p) = 1.1$  and  $g_l(n) = -0.1$  for protons and neutrons, respectively were used. Calculations were performed with the LSSM codes ANTOINE and NATHAN [66] and the results are denoted by LSSM in Fig. 6.2.

## 6.2 Structure of the odd Cd isotopes

### $^{129}\text{Cd}$

The shell-model calculations suggest that the  $27/2^-$  state in  $^{129}\text{Cd}$  is an isomeric spin trap (see Fig. 6.1). The  $E3$  transition ( $27/2^- \rightarrow 21/2^+$ ) is strongly hindered due to the predicted near-degeneracy of the  $27/2^-$  and  $21/2^+$  levels. For similar reasons the  $E3$  transition ( $21/2^+ \rightarrow 15/2^-$ ) is very slow. Therefore, the isomeric states  $27/2^-$  and  $21/2^+$  decay primarily by the  $\beta^-$  emission and the  $\gamma$  decays are not observed experimentally for this nucleus.

### $^{127}\text{Cd}$

The two experimental scenarios EXP-I and EXP-II along with the theoretically calculated level schemes of  $^{127}\text{Cd}$  are shown in Fig. 6.2. The reduced transition probabilities of the primary  $E3$  and  $M2$  transitions in both the cases are compared to SM and LSSM results in Table 6.1. The retarded  $B(E3; (19/2^+) \rightarrow (13/2^-))$  and  $B(M2; (19/2^+) \rightarrow (15/2^-))$  are under- and over-estimated, respectively for both experimental scenarios. In the model space used for the theoretical calculations they are stretched  $E3$ :  $\nu h_{11/2} \rightarrow d_{5/2}$  and  $M2$ :  $\nu h_{11/2} \rightarrow g_{7/2}$  transitions which might be enhanced. However, the respective SM calculated wave functions of the states involved in these two transitions have small components of the  $d_{5/2}$  and the  $g_{7/2}$  orbitals.

Moreover, since the  $E3$  and  $M2$  transitions in this case can be enhanced

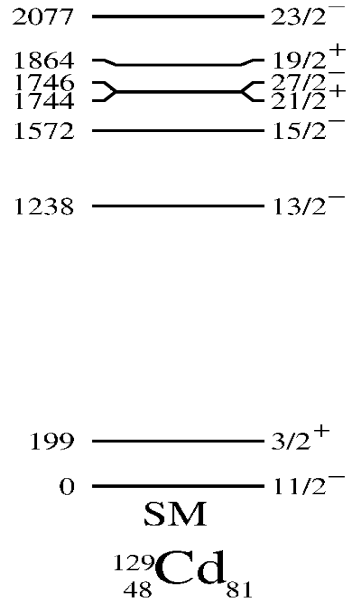


Figure 6.1: Theoretically calculated level scheme for  $^{129}\text{Cd}$ .

due to stretched configurations, the corresponding effective operators may be different from those for  $E2$  and  $M1$  transitions, respectively. A good agreement between experimental and theoretical branching ratio is observed for the  $((15/2^-) \rightarrow (11/2^-))$  821.2 keV  $E2$  and  $((15/2^-) \rightarrow (13/2^-))$  110.4 keV  $M1$  transitions in the scenario labeled as EXP-II. It should be noted that the SM and LSSM values agree as well. The drastic discrepancy for this branching in the alternative cascade assignment (see Table 6.1) establishes a preference for the order labeled as EXP-II.

## $^{125}\text{Cd}$

For  $^{125}\text{Cd}$ , the SM calculated level scheme consists of a large density of states with both positive and negative parities. However, the low-spin states are reproduced well by the theory considering the complex decay pattern of this nucleus. The theoretically calculated level schemes of  $^{125}\text{Cd}$  along with the three possible experimental scenarios (EXP-I, EXP-II, EXP-III) are shown in Fig. 6.3. The EXP-II and EXP-III have different ordering of the 786.4 keV gamma line with respect to the 869.3 keV and its parallel transitions. Whereas, EXP-I is similar to EXP-III with only the ordering of 587.2, 132.5 and 150.4 keV gamma transitions changed. All three possibilities

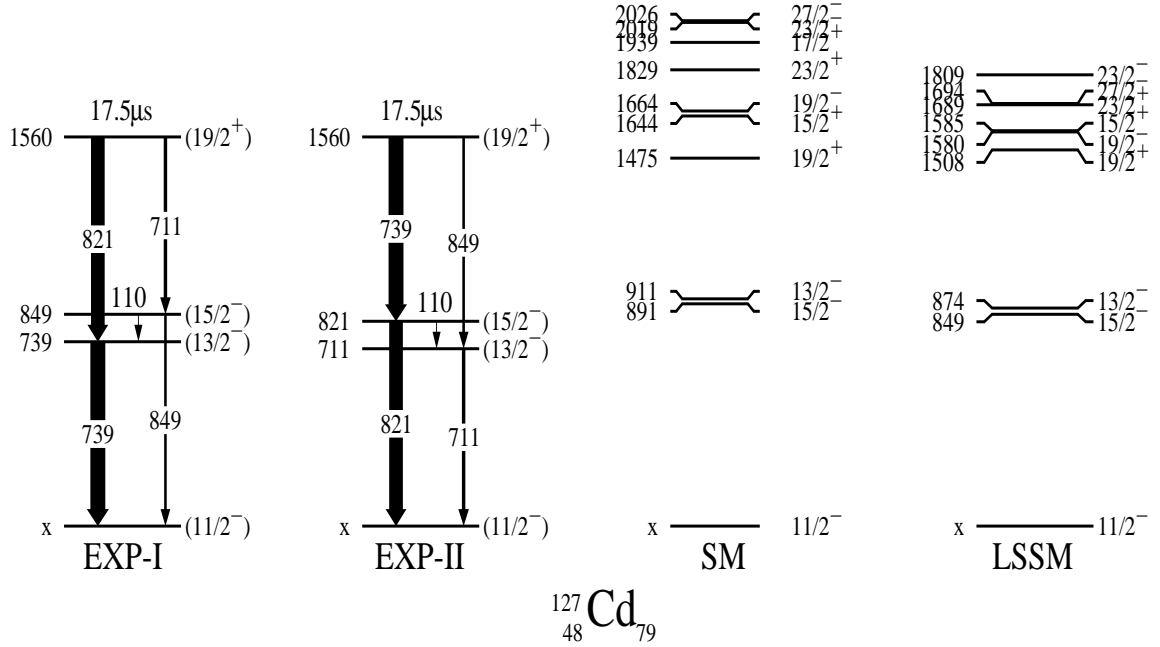


Figure 6.2: The proposed level schemes for  $^{127}\text{Cd}$  and the theoretically calculated spectra using SM and LSSM interactions.

Table 6.1: Experimental and shell-model transition strengths and branching ratios of gamma transitions in  $^{127}\text{Cd}$ . The values for the two alternative experimental level schemes, EXP-I and EXP-II are compared with the SM and LSSM calculations.

Transition	$\sigma L$ $J \rightarrow I$	B( $\sigma L$ ) (W.u)			
		EXP-I	EXP-II	SM	LSSM
$(19/2^+) \rightarrow (13/2^-)$	$E3^a$	$2.30(30) \times 10^{-1}$	$3.40(18) \times 10^{-2}$	$6.19 \times 10^{-3}$	$3.04 \times 10^{-3}$
$(19/2^+) \rightarrow (15/2^-)$	$M2^a$	$7.71(16) \times 10^{-5}$	$2.71(14) \times 10^{-4}$	$1.98 \times 10^{-3}$	$5.75 \times 10^{-3}$
$(15/2^-) \rightarrow (13/2^-)$	$M1^b$	26(3)%	6.3(6)%	5.8%	7.5%
$(15/2^-) \rightarrow (11/2^-)$	$E2^b$	74(3)%	94(4)%	94.2%	92.5%

<sup>a</sup> Pure transition assumed.

<sup>b</sup> Only  $\gamma$ -branching ratio known.

of the decay schemes shown in Fig. 6.3 have identical decay pattern of the  $(19/2^+)$  isomer. However, below this isomer two additional possibilities

Table 6.2: Experimental and shell-model calculated transition strengths and branching ratios of  $\gamma$  transitions below the  $(19/2)^+$  isomer in  $^{125}\text{Cd}$ . Separate values are given for the alternative placements of the 719.5/742.9 keV and 796.6/665.9 keV transitions.

Transition $J \rightarrow I$	$\sigma L$	B( $\sigma L$ ) (W.u)		
		EXP <sup>a</sup>	EXP <sup>b</sup>	SM
$(19/2^+) \rightarrow (15/2^-)_2$	$M2^c$	$3.91(25) \times 10^{-4}$	$3.91(25) \times 10^{-4}$	$4.36 \times 10^{-4}$
$(19/2^+) \rightarrow (13/2^-)_2$	$E3^c$	1.75(11)	1.75(11)	$6.59 \times 10^{-2}$
$(19/2^+) \rightarrow (15/2^-)_1$	$M2^c$	$3.72(7) \times 10^{-4}$	$3.09(20) \times 10^{-4}$	$6.15 \times 10^{-6}$
$(19/2^+) \rightarrow (13/2^-)_1$	$E3^c$	$4.26(27) \times 10^{-2}$	$1.82(11) \times 10^{-1}$	$1.11 \times 10^{-3}$
$(15/2^-)_1 \rightarrow (13/2^-)_1$	$M1^d$	1.6(4) %	12.2(24) %	1.1%
$(15/2^-)_1 \rightarrow (11/2^-)$	$E2^d$	98(5) %	89(6) %	98.9%

<sup>a</sup> The ordering of the cascades below  $(19/2^+)$  isomer as shown in Fig. 6.3.

<sup>b</sup> Reversed order of cascades below the  $(19/2^+)$  isomer.

<sup>c</sup> Pure transition assumed.

<sup>d</sup> Only  $\gamma$ -branching ratio known.

of the ordering of cascades exist with 666 keV level at 796 keV and the 743 keV state at 720 keV instead. The reduced transition probabilities of the primary  $E3$  and  $M2$  transitions in both of these cases are compared to SM results in Table 6.2. The retarded  $B(E3; (19/2^+) \rightarrow (13/2^-)_1)$  and  $B(M2; (19/2^+) \rightarrow (15/2^-)_1)$  are respectively under-estimated for both of the experimental scenarios. The theoretical branching ratio for the  $((15/2^-)_1 \rightarrow (11/2^-))$ , 742.9 keV  $E2$  and  $((15/2^-)_1 \rightarrow (13/2^-)_1)$ , 77.2 keV  $M1$  transitions agrees well with the experimental value in the scenario shown in Fig. 6.3 and labeled as EXP<sup>a</sup> in Table 6.2. The discrepancy for this branching in the alternative cascade assignment EXP<sup>b</sup> (see Table 6.2) establishes a preference for the order EXP<sup>a</sup> of the cascade below the  $(19/2^+)$  state as shown in all the three experimental scenarios (EXP-I, EXP-II, EXP-III) in Fig. 6.3.

Due to lack of experimental information on the ordering of gamma transitions, it is difficult to deduce any preference for the spins and parity of the states above the  $(19/2^+)$  isomer. Only for the case, EXP-I, a tentative assignment of the spins and parities to the excited states is made based on the SM calculations (see Fig. 6.3). If an  $E2$  multipolarity for the 99.2 keV transition is assumed, the calculated  $E2$  transition rates between the high-spin states show that the strengths for positive and negative parity states are very

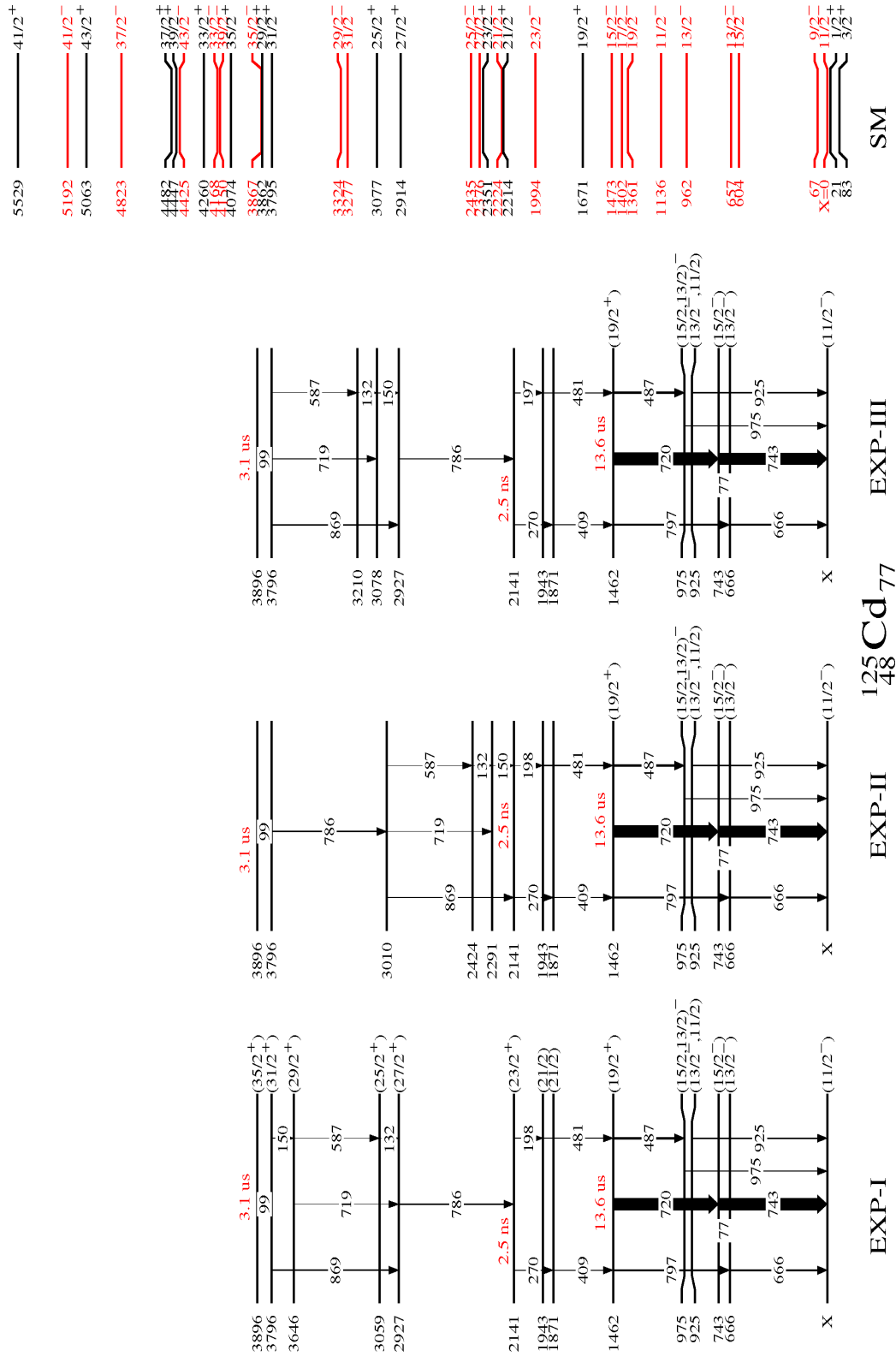


Figure 6.3: The proposed level scheme for  $^{125}\text{Cd}$  and the SM calculated energies of the excited levels.

*Table 6.3:*  $E2$  transition rates between the high-spin states calculated by shell model. The experimentally extracted  $B(E2)$  for 99.2 keV transition is 0.20(1) W.u.

Transition	$\sigma L$	$B(\sigma L)$ (W.u)
$J \rightarrow I$		
$(43/2^+) \rightarrow (39/2^+)$	$E2$	0.162
$(39/2^+) \rightarrow (35/2^+)$		0.153
$(35/2^+) \rightarrow (31/2^+)$		0.588
$(41/2^+) \rightarrow (37/2^+)$		2.855
$(37/2^+) \rightarrow (33/2^+)$		4.072
$(43/2^-) \rightarrow (39/2^-)$	$E2$	12.187
$(39/2^-) \rightarrow (35/2^-)$		16.830
$(35/2^-) \rightarrow (31/2^-)$		15.702
$(41/2^-) \rightarrow (37/2^-)$		7.150
$(37/2^-) \rightarrow (33/2^-)$		5.685

different and only the former agree with the experimental value of 0.20(1) W.u (see Table 6.3). Therefore, it is concluded that the high-spin isomer has positive parity. In addition, from the comparison to the SM calculation a spin-parity of  $(35/2^+)$  seems to be most likely for the state at 3896 keV.

### 6.3 The role of proton-neutron interaction in $^{132}\text{Sn}$ region.

The contribution of  $\pi\nu$  interaction in strong configuration mixing leading to deformations in nuclei has long been recognized [67] with a special case being the valence nucleons occupying the spin-orbit partner orbitals  $(l+1/2, l-1/2)$ . A strong radial overlap of such orbitals results in enhanced proton-neutron correlations which may dominate over the strong pairing interaction, leading to a deviation from the spherical behaviour. The defor-

mation in light nuclei in  $(2s, 1d)$  shell was attributed to the involvement of spin-flip partners  $1d_{5/2}, 1d_{3/2}$  by [68] based on the principle first introduced by [69]. It was already indicated in [68] that the gradual filling of one type of spin-flip partner orbital results in the lowering of its partner of the other type. Later, Heyde *et al.* stressed the multipole decomposition of  $\pi\nu$  interaction and proposed the shifting of single-particle energy states of one type of nucleon with filling of orbitals of the other type due to the monopole part of interaction [70]. The work of Otsuka *et al.* [71] provided a more specific perspective of the monopole interaction by introducing a tensor part favoring the  $j_>, j_<$  coupling more than the  $j_>, j_>$  or  $j_<, j_<$  coupling. The  $N = 20$  shell quenching and the emergence of  $N = 16$  as a new magic number in  $^{24}\text{O}$  was pointed to be the consequence of a strong  $\pi\nu$  tensor monopole between the spin-orbital partners  $\pi d_{5/2}, \nu d_{3/2}$ . Further extensions of the principle were done to explain migration of single-particle energy states in the region,  $Z = 40$  to  $Z = 50$  [72].

Because of all these and many other pioneering works, it is accepted that the interplay of strong  $T = 0$   $\pi\nu$  interaction drives the nuclei towards deformations and collectivity. In the  $^{132}\text{Sn}$  region the role of  $\pi\nu$  interaction in changing the single-particle shell structure is not apparent. The observation of a  $\pi g_{9/2}^{-2}$  seniority isomer in neighbouring  $^{130}\text{Cd}$  [17] along with the theoretical interpretation of a core-excited isomeric state in  $^{131}\text{In}$  [18] proves that the monopole component of  $\pi\nu$  interaction is not strong enough to cause the observed unexpected lowering of low-spin states in  $^{128}\text{Cd}$  [6].

The  $^{128}\text{Cd}$  is a two-proton, two-neutron hole neighbour of doubly-magic  $^{132}\text{Sn}$  and an analogy of this nucleus can be built with  $^{204}\text{Hg}$ . With only two-proton, two-neutron holes in the doubly magic core of  $^{208}\text{Pb}$ ,  $^{204}\text{Hg}$  also exhibits a collective structure. In the absence of any data to comment on the monopole migration of single-particle energy states in this region, the involvement of  $\pi(s, d)$  and  $\nu(p, f)$   $hh$  space was attributed to the onset of collectivity in  $^{204}\text{Hg}$  [74]. The low- $j$   $\pi(s_{1/2}, d_{3/2}, d_{5/2})$  and  $\nu(p_{1/2}, f_{5/2}, p_{3/2})$  orbitals couple to form low-spin states in  $^{204}\text{Hg}$ , thus the respective proton and neutron (holes) are anti-aligned, interacting strongly due to a maximum overlap. The low-spin states are therefore strongly bound. The  $hh$  valence space in  $^{208}\text{Pb}$  shown in Fig. 6.4 is similar to that of  $^{132}\text{Sn}$ . The energies of  $\pi(f_{5/2}, p_{3/2})$  orbitals are not known experimentally for  $^{132}\text{Sn}$  region, however, in  $^{100}\text{Sn}$  the  $\pi(f_{5/2}, p_{3/2})$  orbitals are predicted to lie at an energy of about 5.13 MeV and 2.85 MeV, respectively, below the  $\pi(p_{1/2})$  orbital [73]. Similarly, the energy predictions of  $\pi(f_{5/2}, p_{3/2})$  orbitals in  $^{132}\text{Sn}$  suggest that they are situated near to  $\pi(p_{1/2})$ . Therefore, the coupling of closely lying  $\pi(p_{1/2}, f_{5/2}, p_{3/2})$  and  $\nu(s_{1/2}, d_{3/2}, d_{5/2})$  single-particle orbitals can give ex-

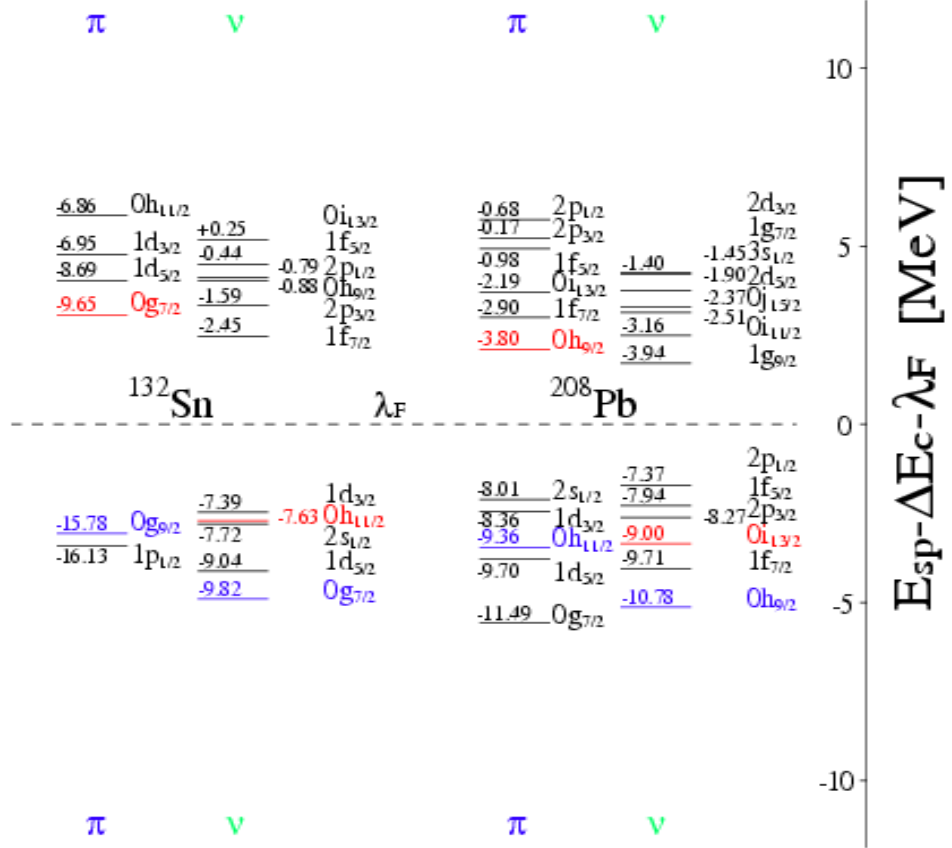


Figure 6.4: Single particle (hole) energy levels in  $^{132}\text{Sn}$  [73] (left) and  $^{208}\text{Pb}$  [73] (right). The quoted energy values are the absolute single-particle energies (SPE) including the Coulomb shift. To eliminate the Coulomb energy difference between the  $\pi$  and  $\nu$  SPE, they are plotted with respect to the middle of the shell gap ( $\lambda_F$ ).

tra binding energy to the low- $J$  excited states in  $^{128}\text{Cd}$ , giving rise to their observed collective structure.

Experimentally, a first indication of the enhanced  $\pi\nu$  interaction in the neutron-rich Cd isotopes is, the need to increase the diagonal TBME elements  $\pi g_{9/2}\nu h_{11/2}$  and  $\pi p_{1/2}\nu h_{11/2}$  by almost -100 keV in order to better describe the energy of  $15/2^-$  and  $13/2^-$  states in  $^{127}\text{Cd}$ . With the modified SM interaction, the low-lying  $13/2^-$ ,  $15/2^-$  doublet in  $^{127}\text{Cd}$  and the  $2_1^+$  state in  $^{128}\text{Cd}$  [64] are closer to the experimental results. From the good agreement between

the SM and the LSSM calculations (see Fig. 6.2) it can be concluded that the increased  $\pi\nu$  interaction (enhanced  $\pi g_{9/2}\nu h_{11/2}$  and  $\pi p_{1/2}\nu h_{11/2}$  TBME) in SM to a large extent accounts for the neglect of the  $\pi(p_{3/2}, f_{5/2})$  orbitals in the model space used. However, the excitation energies of the  $2_1^+$  and the  $13/2^-$  states in  $^{128}\text{Cd}$  and  $^{127}\text{Cd}$ , respectively, still remain  $\sim 150$  keV too large. These remaining deficiencies, with the high-spin isomers being well reproduced indicate a lack of collectivity in the low-spin states.

The systematics of the  $15/2^-$ ,  $13/2^-$  levels in  $^{125,127,129}\text{Cd}$  and their analogues,  $2_2^+$ ,  $2_1^+$  states in the neighboring even  $^{128}\text{Cd}$  are shown in Fig. 6.5. Evolution of energies of these two states when going from  $^{129}\text{Cd}$  to  $^{125}\text{Cd}$  gives another evidence of the enhanced  $\pi\nu$  interaction. The detailed analysis of the wave function partitions calculated by shell model gives the percentage contribution of a particular configuration in the structure of these states and only the dominating contributions are listed in Table 6.4. The  $13/2^-$  state in  $^{127}\text{Cd}$  is an analogue of the  $2_1^+$  state in neighbouring  $^{128}\text{Cd}$ . It has leading configurations  $\pi g_{9/2}^{-2}\nu h_{11/2}^{-3}$  (55%) and  $\pi g_{9/2}^{-2}\nu h_{11/2}^{-1}d_{3/2}^{-2}$  (16 %), which correspond to a  $\nu h_{11/2}$  hole coupled to the  $2_1^+$  state in the neighboring even-even  $^{128}\text{Cd}$ . Since, the  $13/2^-$  state in  $^{127}\text{Cd}$  has an additional  $\pi\nu$  hole interaction, the discrepancy in the SM calculated energy of this state is even larger than in  $^{128}\text{Cd}$ . In contrast, the  $15/2^-$  state contains besides these components (39% and 15%) a 13%  $\pi g_{9/2}^{-2}\nu h_{11/2}^{-1}d_{3/2}^{-1}s_{1/2}^{-1}$  configuration corresponding to the coupling of a  $\nu h_{11/2}$  hole to the  $2_2^+$  state in  $^{128}\text{Cd}$ . On the other hand in  $^{129}\text{Cd}$  both the  $13/2^-$  and the  $15/2^-$  states have pure configurations  $\pi g_{9/2}^{-2}\nu h_{11/2}^{-1}$  (99%). Hence, the absence of the coupling of an extra  $\nu h_{11/2}$  hole to the  $\pi$  levels results in higher energies of the  $13/2^-$  and  $15/2^-$  states in  $^{129}\text{Cd}$  (see Fig. 6.5).

The good description of the  $T = 1$   $\nu\nu$  case of the heavy  $^{124-130}\text{Sn}$  isotopes [54] and the  $\pi\pi$   $^{130}\text{Cd}$  [17], with a need to increase the  $\pi\nu$  interactions for the Cd isotope chain to yield a satisfactory description of the experimental level schemes indicates an enhanced proton-neutron interaction in the region.

*Table 6.4:* The wave function partitions of  $15/2^-$ ,  $13/2^-$  states in  $^{125,127,129}\text{Cd}$  and their analogue,  $2_2^+$  and  $2_1^+$  states in  $^{128}\text{Cd}$ . Only the dominating configurations are listed.

Nucleus	$J^\pi$	Configuration	(%)
$^{125}\text{Cd}$	$(15/2^-)_1$	$\pi g_{9/2}^{-2} \otimes \nu h_{11/2}^{-3} d_{3/2}^{-2}$	50%
		$\pi g_{9/2}^{-2} \otimes \nu h_{11/2}^{-3} d_{3/2}^{-1} s_{1/2}^{-1}$	11%
	$(13/2^-)_1$	$\pi g_{9/2}^{-2} \otimes \nu h_{11/2}^{-3} d_{3/2}^{-2}$	42%
$^{127}\text{Cd}$	$(15/2^-)$	$\pi g_{9/2}^{-2} \otimes \nu h_{11/2}^{-3}$	39%
		$\pi g_{9/2}^{-2} \otimes \nu h_{11/2}^{-1} d_{3/2}^{-2}$	15%
		$\pi g_{9/2}^{-2} \otimes \nu h_{11/2}^{-1} d_{3/2}^{-1} s_{1/2}^{-1}$	16%
	$(13/2^-)$	$\pi g_{9/2}^{-2} \otimes \nu h_{11/2}^{-3}$	55%
		$\pi g_{9/2}^{-2} \otimes \nu h_{11/2}^{-1} d_{3/2}^{-2}$	16%
$^{128}\text{Cd}$	$(2^+)_2$	$\pi g_{9/2}^{-2} \otimes \nu h_{11/2}^{-2}$	13%
		$\pi g_{9/2}^{-2} \otimes \nu d_{3/2}^{-2}$	28%
		$\pi g_{9/2}^{-2} \otimes \nu d_{3/2}^{-1} s_{1/2}^{-1}$	25%
	$(2^+)_1$	$\pi g_{9/2}^{-2} \otimes \nu h_{11/2}^{-2}$	71%
$^{129}\text{Cd}$	$(15/2^-)$	$\pi g_{9/2}^{-2} \otimes \nu h_{11/2}^{-1}$	100%
	$(13/2^-)$	$\pi g_{9/2}^{-2} \otimes \nu h_{11/2}^{-1}$	99%

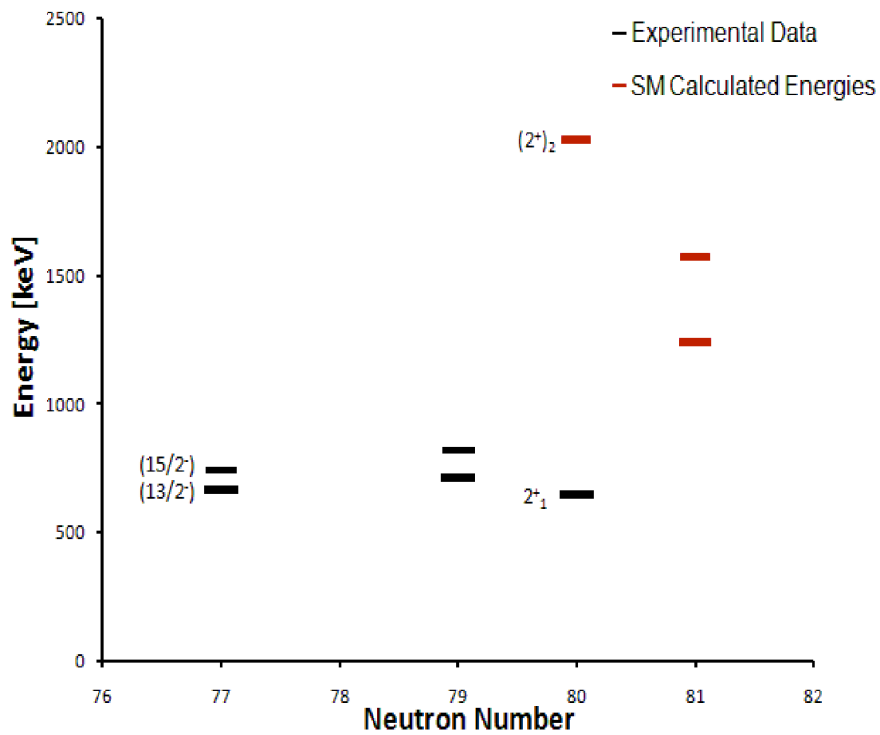


Figure 6.5: Systematics of the energy of  $15/2^-$ ,  $13/2^-$  levels in  $^{125,127,129}\text{Cd}$  and their analogue,  $2^+_2$  and  $2^+_1$  states in the neighboring even  $^{128}\text{Cd}$ . The level energies in odd-mass Cd isotopes are plotted with respect to the  $\beta^-$  decaying ( $11/2^-$ ) state, while in even-mass  $^{128}\text{Cd}$ , the energies are relative to the  $0^+$  ground state.

# Chapter 7

## Outlook

The flattening of the yrast  $2^+$  excitation energy for neutron-rich Cd isotopes is an interesting phenomenon to investigate. Two independent theories explaining its origin, one as a sudden onset of quadrupole deformation in  $^{128}\text{Cd}$  [20] and the other as the existence of enhanced proton-neutron interaction in the region, presented in this work [59] make it worth investigating the issue further. The measurement of transition strength  $B(E2)$  is the best tool to prove whether the spherical structure of low-energy excited states in even- $A$  Cd isotopes remains intact and the enhanced proton-neutron interaction drives the observed collectivity or the yrast  $2^+$  states are quadrupole deformed. Several experiments have been carried out to measure  $B(E2)$  values of  $^{122-126}\text{Cd}$  [75] via the low-energy Coulomb excitation in inverse kinematics at the Isotope Separation OnLine (ISOL) facility of CERN [7]. The systematics of the experimental  $B(E2)$  values for Cd chain along with shell-model calculations for  $^{126,128}\text{Cd}$  and beyond-mean-field predictions for  $^{126,128,130}\text{Cd}$  are shown in Fig. 7.1. The two predictions for  $^{126}\text{Cd}$  and  $^{128}\text{Cd}$  deviate from each other considerably which indicates the differences in the theoretical models. This makes it even more important to measure these quantities experimentally.

One of the major challenges to perform  $B(E2)$  measurements in the region of neutron-rich nuclei is the low reaction cross sections for production of exotic fragments. The intensity of secondary beams provided by the present day ISOL facilities are not sufficient enough to measure the transitions strengths at the extremes of nuclear landscape. The future research in this region should benefit from the intense beams provided by the forthcoming ISOL facilities like FRIB [76], SPIRAL2 [77] etc combined with the high gamma-detection efficiency of the next generation arrays like AGATA [78] and GREY [79]. Another direction towards the same goal would be to perform Coulomb excitation at the in-flight facilities with intermediate

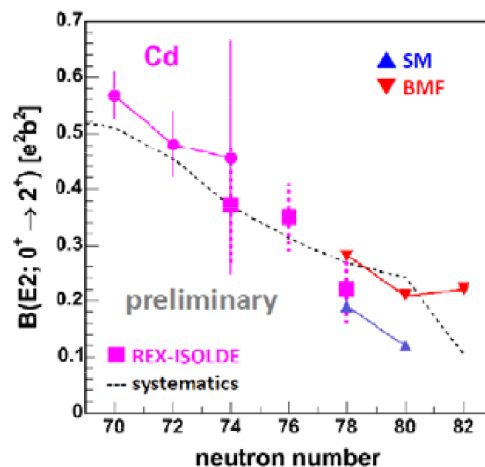


Figure 7.1:  $B(E2)$  values of the first excited  $2^+$  states in the even-even Cd isotopes [80, 81, 75] with the shell-model and beyond-mean-field predictions [75].

beam energies by selecting only the forward angle scatterings. Due to high projectile velocities thick secondary targets can be used enhancing the reaction yields. The future in-flight isotope separation facilities including FAIR [82] and RIKEN [11] would be the best places for such experiments.

However, there are some advantages and disadvantages of intermediate energy Coulomb excitation over the low-energy one which are discussed in section 7.1. The best solution would be a facility combining the positive points of both the approaches. Moving along the same lines, next sections of this outlook chapter summarize the advancements in the development of slowed down beams at GSI.

## 7.1 Slowed Down Beams at GSI : A test measurement

With the existing GSI accelerator complex, the Coulomb excitation experiments with intermediate beam energies ( $< 200$  MeV/u) can be performed. The electromagnetic interaction at these energies is so fast that the population of only the first excited states of projectile and target nuclei is possible.

Whereas, the advantage of performing such experiments with projectiles of energies around or below 5 MeV/u is that the comparatively slower interaction time allows multistep excitations resulting in the population of high- $J$  states [83]. In addition, Coulomb excitation at low energies suppresses the contribution of nuclear interactions because the projectile nuclei cannot penetrate through the Coulomb barrier of the target nuclei.

The advantage of building a slowed down beam facility at GSI coupled with FAIR is that the intense radioactive beams at Coulomb barrier energies can be produced. The high angular momentum transfer at these energies will open a new field of high-spin investigations at the in-flight separation facilities.

Secondary beams of radioactive nuclei can be produced by in-flight projectile fragmentation or fission. The radioactive beams planned at the final focal plane of the Super-FRS [84] are expected to have intensities sufficient for nuclear spectroscopy and reaction studies at energies around the Coulomb barrier. The low beam energy will be obtained by slowing down relativistic ions in a thick degrader. This has the following advantages as compared to an ISOL scheme with a post-acceleration stage widely used for the production of beams of unstable nuclei at low energies nowadays. The radioactive ions in an ISOL facility are produced in reaction targets at thermalized energies from where they are extracted and reaccelerated. However, depending on the chemical properties it is difficult to extract some elements from the production target and a very low extraction efficiency is obtained. In addition, the time scales of extraction and reacceleration limit the lifetime of the isotopes that can be studied afterwards to several tens of milliseconds. In contrast to the ISOL facilities, the experiments performed with beams slowed down in a thick homogeneous degrader, can access short lived fragments with high survival rate after the deceleration. To test this concept, an experiment was performed at the existing Fragment Separator (FRS) facility at GSI [31]. The experimental questions in realizing the idea were examined and the beam properties after slowing down process were characterized.

### 7.1.1 Experimental Problems

Relativistic fragments penetrating through and interacting with a thick piece of matter undergo energy and angular straggling. The simulated result for angular straggling obtained with the MOCADI code [61] for a primary  $^{64}\text{Ni}$  beam at an incident energy of 250 MeV/u, slowed down to 13 MeV/u in a homogeneous Al degrader of  $3.95 \text{ g/cm}^2$  is shown in Fig. 7.2. The considerable angular straggling makes it necessary to track the ions after the degrader on an event-by-event basis. During the deceleration, nuclear

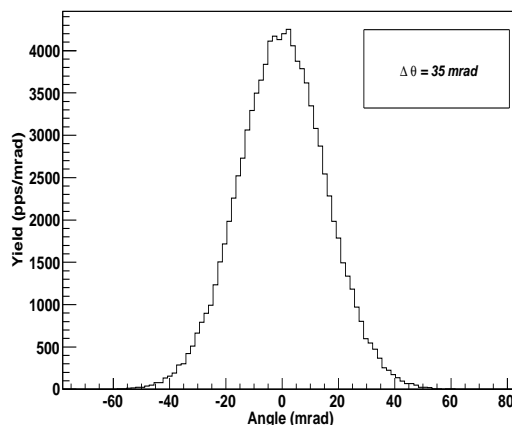


Figure 7.2: Simulated angular spread of a  $^{64}\text{Ni}$  beam after slowing down from 250 MeV/u to 13 MeV/u in a  $3.95 \text{ g/cm}^2$  Al degrader.

reactions also occur which lead to the production of unwanted isotopes. The simulated yields [87] of reaction products in the degrader are illustrated in Fig. 7.3 as a function of beam energy. The integrated background contribution amounts to  $\sim 0.1\%$  of the slowed down beam at 13 MeV/u. Since the predicted contamination due to nuclear reactions in the degrader is quite low, the identification of ions after deceleration is not necessary for the reactions in secondary target with high cross sections.

However, simulation indicates that the introduced energy straggling requires a measurement of the beam energy after slowing down (see Fig. 7.4). Since the beams have energies around 5-10 MeV/u, the employed detectors to track the trajectory and measure energy after the degrader should be as thin as possible to avoid any further energy and angular straggling of the beam. In addition, the tracking detectors should be large enough to cover the whole angular distribution of the slowed down beam.

In all the simulations discussed above, an initial energy spread ( $\Delta E/E$ ) of  $\sim 0.1\%$  for the incident beam was considered based on the experimentally measured time-of-flight between scintillators SC21 and SC41 kept before the degrader at final focal plane (S4) of fragment separator. The physical locations of these scintillator detectors are illustrated in Fig. 3.5 and the corresponding TOF distribution is shown in Fig. 7.5.

To track the trajectory of the beam and measure its energy after slowing down, a detector system consisting of a secondary electron emission foil coupled to the position sensitive microchannel plates (MCP) [86] was used. The

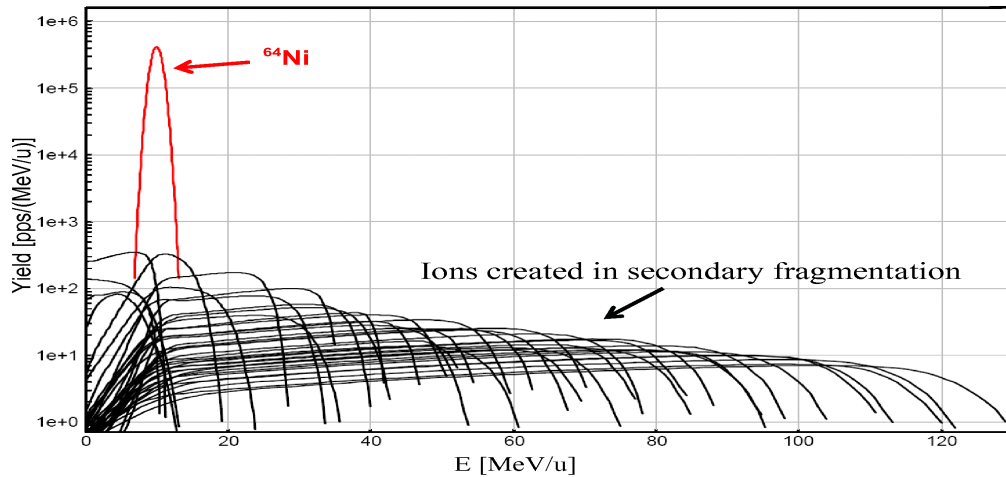


Figure 7.3: The dominant curve (red) represents slowed down  $^{64}\text{Ni}$  ions and the contaminants from nuclear reactions in Al degrader are shown in black curves.

following section deals with the working principle of MCP detectors used in the present experiment.

#### 7.1.1.1 Microchannel plates (MCP) as beam tracking and Time-Of-Flight detectors

The microchannel plates are made of a glass surface with micro-meter diameter channels on it [85]. Each channel acts as an independent electron multiplier. The collisions of incoming electrons with walls of the channels produce secondary electrons which are accelerated along the channel by an electric field and are finally collected at the ends. Typical gains of the order of  $10^4 - 10^7$  are achieved using these detectors. A cross sectional view of the MCP surface is shown in Fig. 7.6. To ensure that the incident electrons hit the walls, a chevron MCP can be used in which the channels are made at an angle to the MCP surface. A schematic layout of two microchannel plates with chevron configuration of the channels is shown in Fig. 7.7. The output electrons of one MCP initiate the cascade in the other, thereby giving higher gains. The total transit time of electrons through the channels is of the order of 0.1 ns and therefore, these detectors find their applications for fast timing purposes.

To have minimum matter in the beam path, the MCP detectors were

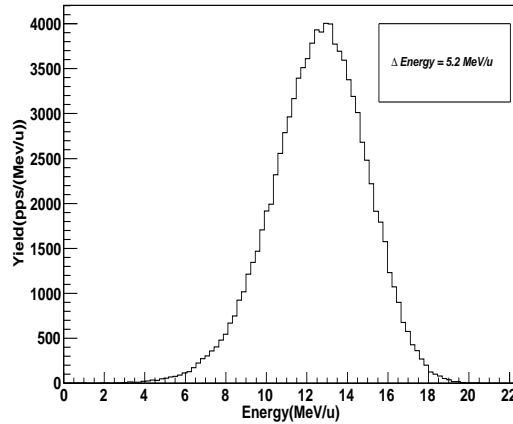


Figure 7.4: Simulated energy straggling of a  $^{64}\text{Ni}$  beam after slowing down from 250 MeV/u to 13 MeV/u in a  $3.95 \text{ g/cm}^2$  Al degrader.

kept at an angle of  $90^\circ$  to the beam direction and a thin metalized mylar foil of  $1.5 \mu\text{m}$  thickness was kept in the beam line. The ions hitting the thin conversion foil lead to the emission of secondary electrons which are then deflected towards the MCP using the electrostatic mirror [86]. A schematic layout of the working principle of secondary electron beam tracking MCP detector with the acceleration and the bending wire grids is shown in Fig. 7.8(left). The secondary electrons are accelerated by applying a negative voltage to the emissive foil. They then drift in a field free region defined by the triangular wire grids kept at ground potential. Bending of the electrons is realized by maintaining a negative voltage gradient between the triangular grids and bending wires kept at an angle of  $45^\circ$  to the microchannel plates (see Fig. 7.8(left)). A picture of MCP detector assembly with a mylar foil and electrostatic mirror used in the present experiment is shown in Fig. 7.8(right). The advantage of using such a geometry for the mirror is that the secondary electrons traverse equal distance irrespective of their vertical position of emission at the foil and thus, arrive approximately at the same time to the MCP surface. This combined with a fast timing signal from the MCP allows to obtain a good temporal resolution. The pre-amplifiers for the time signals were attached close to the MCP surface in order to minimize the noise pickup and thereby reducing the jitter to achieve a good time resolution. A signal with a rise time of  $\sim 2 \text{ ns}$  from MCP detectors of dimension  $5 \times 6 \text{ cm}^2$  coupled to the fast pre-amplifier was detected. A triple alpha source with characteristic alpha energies of  $^{239}\text{Pu}$ ,  $^{241}\text{Am}$  and  $^{244}\text{Cm}$  at 5.244, 5.49 and

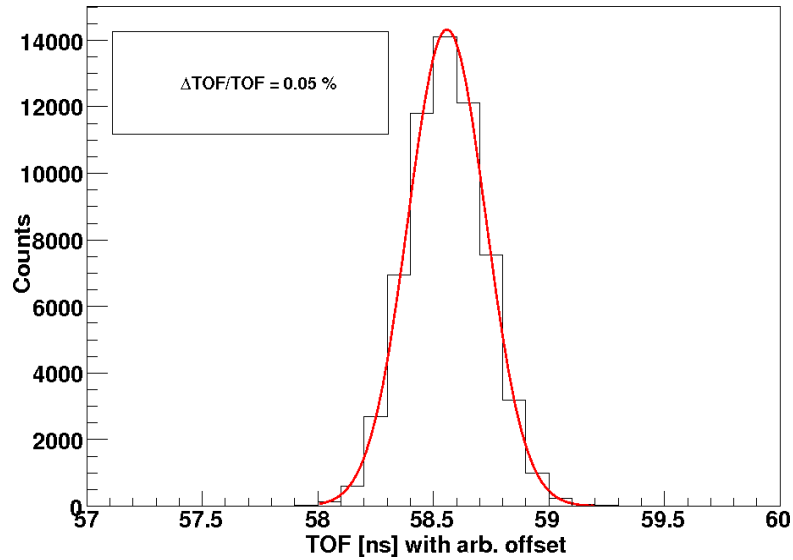


Figure 7.5: The time-of-flight spectrum between SC21 and SC41 at the FRS. A spread of ( $\Delta TOF/TOF$ ) of 0.05% for the incident  $^{64}\text{Ni}$  beam was measured.

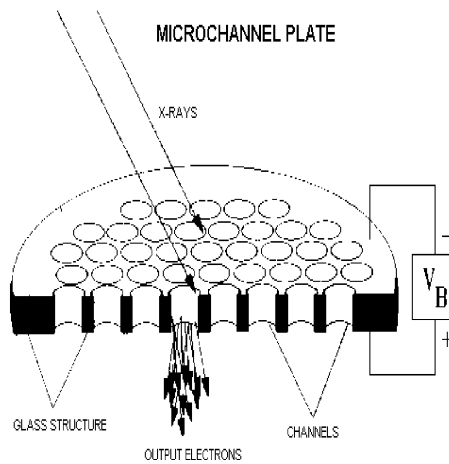


Figure 7.6: A cross sectional view of MCP surface with the micro-meter diameter channels acting as the secondary electron multipliers.

5.81 MeV, respectively was used to perform a TOF measurement between

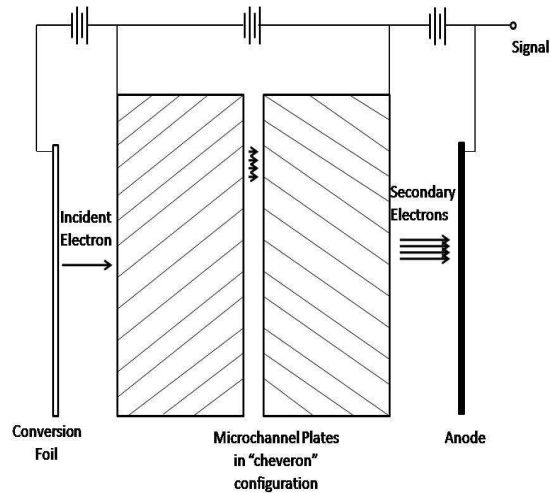


Figure 7.7: Two MCP detectors with chevron configuration of the channels to ensure that the incident electrons hit the channel walls. The figure is taken from Ref. [85]

the two MCP detectors with similar characteristics, separated by a distance of 10 cm. The obtained TOF spectra is illustrated in Fig. 7.9(left). A timing resolution of the order of 150 ps for the detectors was achieved.

A position signal can also be obtained by using a delay line readout. In particular, two delay lines perpendicular to each other provided X and Y position coordinates for reconstructing the trajectories of the beam particles. For the determination of position resolution of the detectors, a  $^{252}\text{Cf}$  fission fragment source was used. The high atomic number  $Z$  of the fission fragments results in an increased production of secondary electrons from the mylar foil. Therefore, a good position resolution was obtained. The mylar foil was covered with a mask made of plastic with slits. The obtained image of the mask from the Y versus X positions given by the MCP is shown in Fig. 7.9(right). A position resolution of 1.5 mm was obtained for both horizontal and vertical directions.

### 7.1.2 Experimental setup

The setup of the slowed down beam test experiment is shown in Fig. 7.10, which consists of a scintillator SC41, an Al degrader, two position sensitive microchannel plate (MCP) detectors and a Silicon (Si) detector of thickness

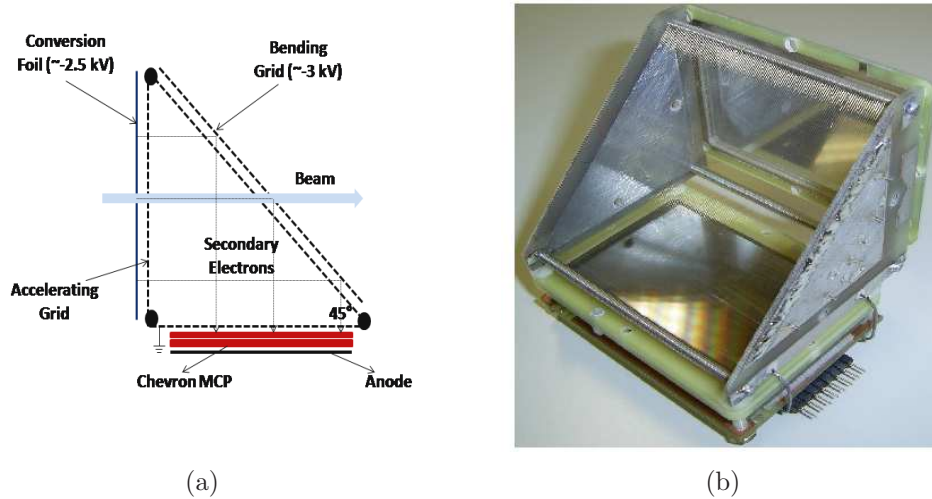


Figure 7.8: Left: A schematic layout of the secondary electron emission microchannel plate detector with electrostatic mirror taken from Ref. [86]. Right: A picture of the secondary electron detector based on microchannel plates used for beam tracking and TOF measurement in the present experiment.

300  $\mu\text{m}$  [88]. In this experiment, a primary  $^{64}\text{Ni}$  beam at 250 MeV/u was slowed down in a 3.95 g/cm<sup>2</sup> Al degrader at the final focal plane (S4) of FRS (see Fig. 3.1). Beam particles after the degrader entered a vacuum chamber in which the MCP and Si detectors were placed.

The microchannel plate detectors provided position coordinates of the beam after degrader, while its energy was extracted by the TOF measurement between SC41 and one of the two MCPs. The energy after slowing down was determined with an accuracy of 1% due to the MCP time resolution of 150 ps and a flight path of 1.5 m between the scintillator and MCP1. The Si detector registered energy loss of the beam. The energy of  $^{64}\text{Ni}$  beam when it starts punching through a 300  $\mu\text{m}$  thick Si detector was estimated by ATIMA [89] to be around 21 MeV/u. The  $\Delta E$  in Si versus the incident beam energy was compared to the corresponding plot given by the simulation [89] with input beam parameters as described in section 7.1.1 and an experimental setup resembling Fig. 7.10. The two spectra are shown in Fig. 7.11. From the simulated  $\Delta E$ -E distribution (see Fig. 7.11(right)), it is evident that the  $^{64}\text{Ni}$  ions at 13 MeV/u after the degrader are mostly stopped in the Si detector and the ions which are punching through are the contaminants produced

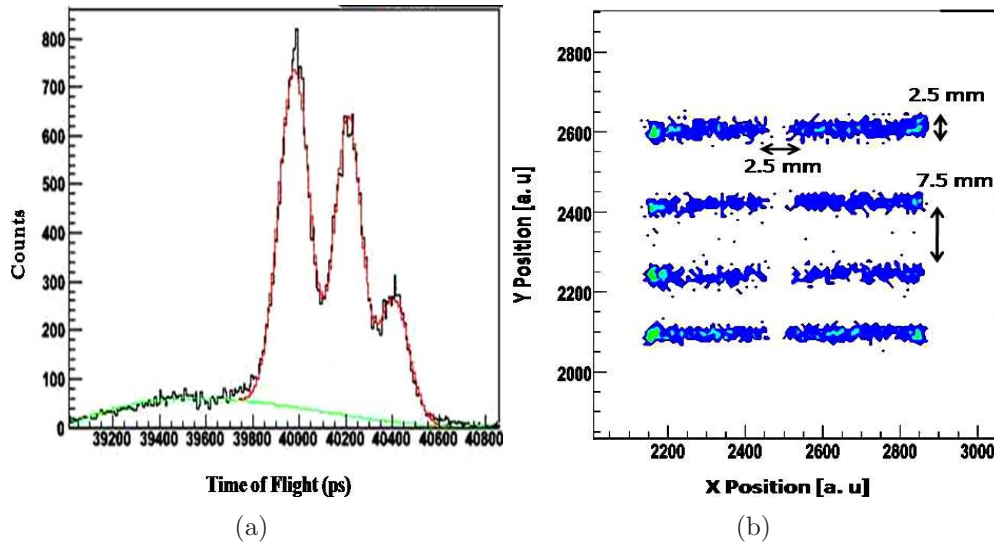


Figure 7.9: Left: Time-of-flight spectrum between the two MCP detectors separated by a distance of 10 cm. A triple alpha source was used for the measurement. Right: An image of mask placed in front of the Mylar foil of one of the MCP detectors. A position resolution of 1.5 mm was obtained for both horizontal and vertical directions of the MCP.

in nuclear reactions. Therefore, the energy peak in Fig. 7.13 corresponds predominantly to the slowed down  $^{64}\text{Ni}$  ions and the events in the range of 21 - 60 MeV/u are contributions from the reactions during deceleration in the degrader. The two distinct structures below the energy of 21 MeV/u in the experimental plot (see Fig. 7.11(left)) are due to the energy loss of beam particles at MCP wire grids. The beam particles scattered on the wires lose part of their energy due to interaction and thus reach the Si detector with lower energies as compared to the non-scattered particles. The ratio of number of particles scattered, to the ones not interacting with the MCP wire grids is of the order of  $\sim 0.16$ , which corresponds to the probability of hitting the wire grids of both of the MCP detectors with wires of  $25\ \mu\text{m}$  diameter separated by a distance of 1 mm.

### 7.1.3 Results

The extracted energy distribution (from TOF measurement between SC41 and MCP1) of the beam after slowing down in the degrader is shown in Fig. 7.13. To obtain a clean energy spectrum only the events having correlated X and Y position coordinates from MCP1 and MCP2 (see Fig. 7.12(left)) and

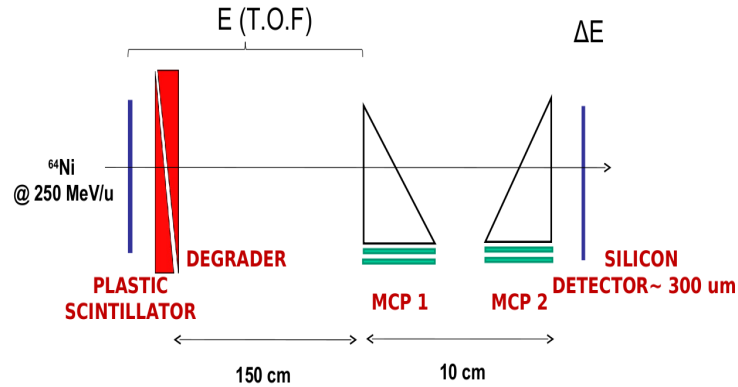


Figure 7.10: A schematic setup for the slowed down beam test experiment. The MCP and Si detectors were kept in a vacuum chamber.

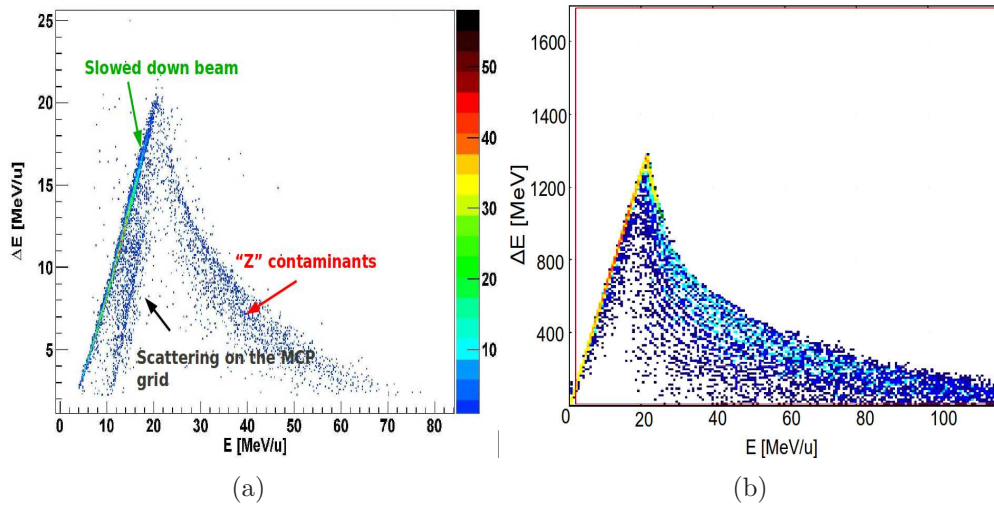


Figure 7.11: Left:  $\Delta E$  in Si detector versus the energy distribution of the slowed down  $^{64}\text{Ni}$  beam. The results were compared to simulations (right). The plot shows that the  $^{64}\text{Ni}$  ions are mostly stopped in Si detector whereas contaminants produced in the nuclear reactions in degrader punch through it. This gives an estimate of the range of energy of the background contaminants.

lying in the condition shown in red in Fig. 7.12(right) which was applied on the image of both MCPs, were further analysed.

An energy distribution of the beam with a width of 8 MeV/u (FWHM)

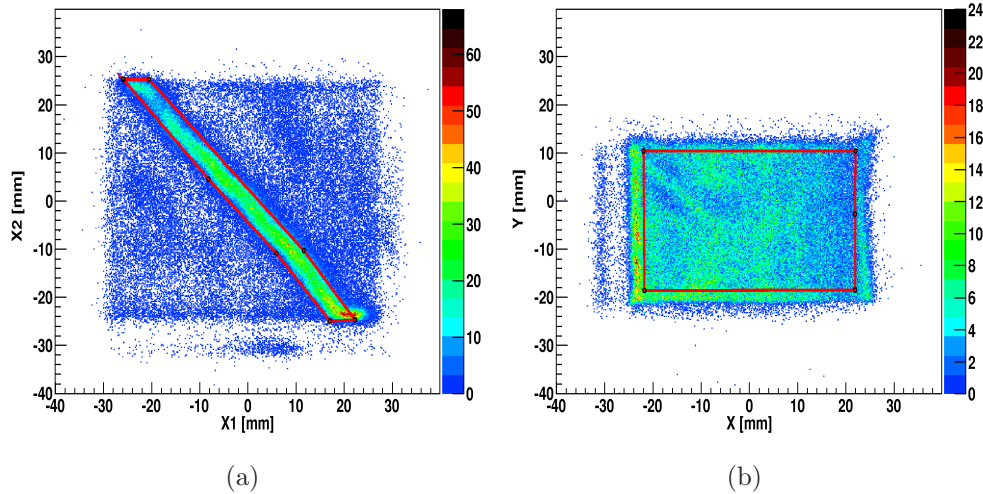


Figure 7.12: Left: The X coordinate from MCP1 versus the X coordinate from MCP2. Only the events lying in the straight cut are correlated. Right: The Y versus X image of MCP1. The events lying inside the gate shown in red were further analysed.

was obtained. In order to estimate the background underneath the dominant energy peak, the simulated background distribution (see Fig. 7.3) was integrated and scaled to the experimentally obtained energy distribution in the range of 21 - 60 MeV/u. This resulted in a peak-to-background ratio of 2% at an energy of 13 MeV/u. The difference of an order of magnitude between the simulated background ratio and the experimentally obtained value is due to the presence of an iron window of 0.2 mm thickness at the entrance of the vacuum chamber where the two MCP and Si detectors were placed. The energy and angular straggling of the slowed down beam caused by this additional iron window broadens the resulting energy distribution and henceforth reduces the peak-to-background ratio. Once the effects of this iron window were taken into account, a ratio of  $\sim 1\%$  was achieved with the simulation. The survival rate of the  $^{64}\text{Ni}$  ions after passing through the degrader was 80%. This number was obtained by comparing the number of events in SC41 and events in the dominant energy peak shown in Fig. 7.13. In reality this ratio is larger than the measured energy distribution of  $^{64}\text{Ni}$  ions in the MCP detectors covering only a part of the total beam distribution due to their limited dimensions. Unfortunately, the angular straggling could not be determined in the present experiment due to the limited size

of tracking detectors which were positioned at a distance of 1.5 m from the degrader.

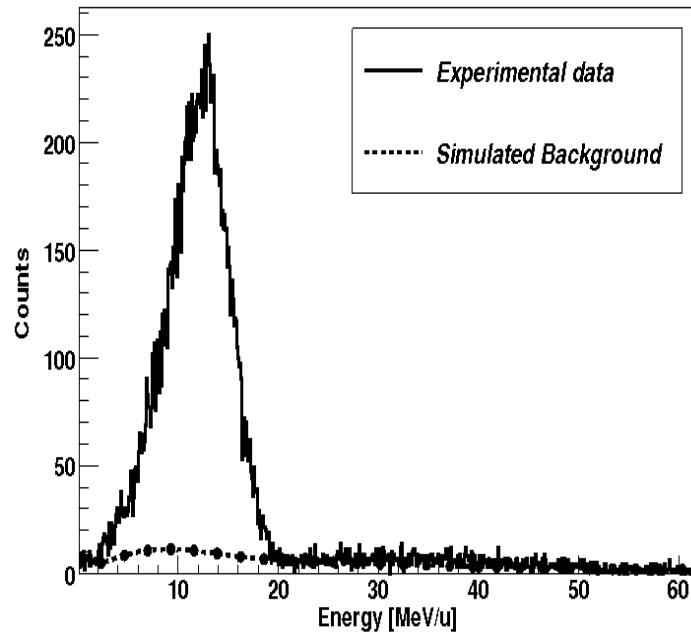


Figure 7.13: Energy distribution of  $^{64}\text{Ni}$  ions after slowing down in Al degrader. A final energy of 13 MeV/u was obtained with a width of 8 MeV/u. The dashed curve represents the integrated simulated background.

In conclusion, the presented experimental results are in qualitative agreement with the performed simulations and hence, support the suitability of the slowed down beams for secondary reactions. An advantage of using this technique for performing Coulomb excitation experiments at low energies might be that the beam after slowing down in the degrader has a range of energies. Different slices of beam energies can be selected with an accuracy allowed by the time resolution of TOF detectors. The data obtained for different energy slices can then be integrated to result in higher statistics. An example of simulated number of counts in the photopeak of  $2^+ \rightarrow 0^+$  and  $4^+ \rightarrow 2^+$  transitions populated in the Coulomb excitation of  $^{64}\text{Ni}$  on a  $^{197}\text{Au}$  target of  $0.76 \text{ mg/cm}^2$  thickness as a function of incident beam energy is shown in Fig. 7.14. A primary beam intensity of  $5 \times 10^5$  particles/s at S4 and a gamma-detection efficiency of 10% is considered.

The planned test measurements involving Coulomb excitation of slowed

down fragments coupled with the newly developed large-area tracking detectors based on the principle described in section 7.1.1.1 will demonstrate the applicability of such experiments and will provide new directions along the studies using in-flight separation techniques.

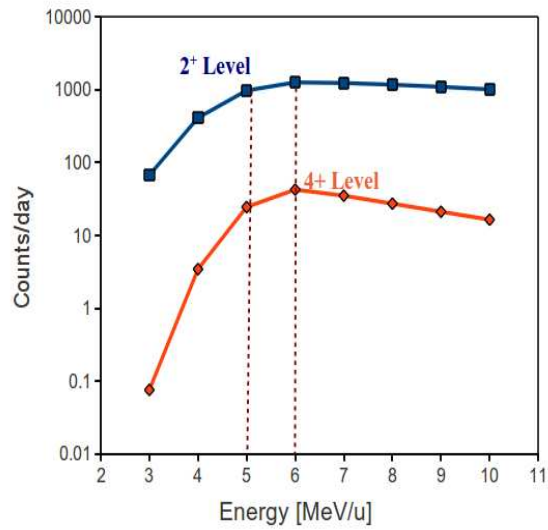


Figure 7.14: Simulated counts in the photopeak of gamma transitions from  $2^+ \rightarrow 0^+$  and  $4^+ \rightarrow 2^+$  populated in the Coulomb excitation of  $^{64}\text{Ni}$  on a  $^{197}\text{Au}$  target of  $0.76 \text{ mg/cm}^2$  thickness. Primary beam intensity of  $5 \times 10^5$  particles/s at S4 and a gamma-detection of 10% is considered. The region selected by dashed lines corresponds to an energy slice. Analysis will be done by integrating the statistics in multiple energy slices.

# Bibliography

- [1] A. Bohr and B. Mottelson, *Nuclear Structure*, Volume I: Single-Particle Motion, (World Scientific, Singapore, 1998).
- [2] M. Goeppert-Mayer, Phys. Rev. **75**, 1969 (1949).
- [3] O. Haxel, J. Jensen, and H. Suess, Phys. Rev. **75**, 1766 (1949).
- [4] M. Goeppert-Mayer, The shell model, Nobel Lecture, December 12, 1963.
- [5] T. Kautzsch *et al.*, Eur. Phys. J. A **9**, 201(2000).
- [6] L. Cáceres *et al.*, Phys. Rev. C **79**, 011301(R) (2009).
- [7] ISOLDE Radioactive Ion Beam Facility,  
<http://isolde.web.cern.ch/isolde/>.
- [8] Helmholtzzentrum für Schwerionenforschung mbH, <http://www.gsi.de/>.
- [9] Grand Accélérateur National d'Ions Lourds, <http://www.ganil.fr/>.
- [10] National Superconducting Cyclotron Laboratory,  
<http://www.nscl.msu.edu/>.
- [11] RIKEN Radioactive Ion Beam Factory, <http://ribfweb1.riken.go.jp/>.
- [12] Isotope Separator and Accelerator, <http://www.triumf.ca/people/baartman/ISAC>.
- [13] S. Pietri *et al.*, Nucl. Instr. Meth. B **261**, 1079 (2007).
- [14] <http://www.phy.anl.gov/gammasphere>.
- [15] J. Dobaczewski, I. Hamamoto, W. Nazarewicz and J.A. Sheikh, Phys. Rev. Lett. **72**, 981 (1994).
- [16] I. Dillmann *et al.*, Phys. Rev. Lett. **91**, 162503 (2003).

- 
- [17] A. Jungclaus *et al.*, Phys. Rev. Lett. **99**, 132501 (2007).
- [18] M. Górska *et al.*, Phys. Lett. B **672**, 313 (2009).
- [19] B. Chen *et al.*, Phys. Lett. B **355**, 37 (1995).
- [20] T. R. Rodríguez, J.L. Egido and A. Jungclaus, Phys. Lett. B **668**, 410 (2008).
- [21] R. F. Casten, *Nuclear Structure from a Simple Perspective*, Second Edition, (Oxford University Press).
- [22] P.J Brussard and P.W.M Glaudemans, *Shell-model applications in nuclear spectroscopy*, North-Holand, Amsterdam (1977) p.53-56.
- [23] K. Heyde *Basic ideas and concepts in nuclear physics*, Third Edition, (2004), p.357-364.
- [24] P. J Brussard and P. W. M Glaudemans, *Shell-model applications in nuclear spectroscopy*, North-Holand, Amsterdam (1977) p.100.
- [25] P. J Brussard and P. W. M Glaudemans, *Shell-model applications in nuclear spectroscopy*, North-Holand, Amsterdam (1977) p.328-333.
- [26] K. Brueckner, Phys. Rev. **97**, 1353 (1955).
- [27] T. T. S. Kuo and G. E. Brown, Nucl. Phys. **85**, 40-86, (1966).
- [28] T. Hamada and I.D. Johnston, Nucl. Phys. **34**, 382-403, (1962).
- [29] M. Hjorth-Jensen, T.T.S. Kuo, and E. Osnes, Phys. Rep. **261**, 125 (1995).
- [30] [http://www.gsi.de/portrait/beschleunigeranlage\\_e.html](http://www.gsi.de/portrait/beschleunigeranlage_e.html).
- [31] H. Geissel, Nucl. Instr. Meth. B **70**, 286 (1992).
- [32] <http://www-inj.gsi.de/>.
- [33] <http://www.gsi.de/beschleuniger/sis18/sis.html>.
- [34] J.-J. Gaimard and K.-H. Schmidt, Nucl. Phys. A **531**, 709 (1991).
- [35] H. W. Barz, J. P. Bondorf, R. Donangelo, I. N. Mishustin, and H. Schulz, Nucl. Phys. A **448**, 753 (1986).
- [36] M. Blann, and M. G. Mustafa, Phys. Rev. C **44**, 431 (1991).

- 
- [37] J. Hüfner, K. Schäfer, and B. Schürmann Phys. Rev. C **12**, 1888 (1975).
- [38] V. Borrel *et al.*, Z. Phys. A **314**, 191 (1983).
- [39] A. S. Goldhaber, Phys. Lett. B **53**, 306 (1974).
- [40] K. Sümmerer *et al.*, Phys. Rev. C **42**, 2546 (1990).
- [41] K. Sümmerer and B. Blank, Phys. Rev. C **61**, 034607 (2000).
- [42] H. Folger *et al.*, Nucl. Instr. Meth. A **303**, 24 (1991).
- [43] R. Kumar *et al.*, Nucl. Instr. Meth. A **598**, 754 (2009).
- [44] H. Stelzer, Nucl. Instr. Meth. A **310**, 103 (1991).
- [45] <http://www-wnt.gsi.de/frs/technical/FRSsetup/detectors/sci.asp>.
- [46] R. Schneider and A. Stolz, Technical Manual Ionization Chamber MUSIC80 (2000).
- [47] M. Wilhelm, J. Eberth, G. Pascovici, E. Rademacher, H. G. Thomas, P. von. Brentano, H. Prade, and R. M. Lieder Nucl. Instr. Meth. A **381**, 462 (1996).
- [48] M. Pfützner *et al.*, Nucl. Instr. Meth. A **493**, 155 (2002).
- [49] [www.xia.com](http://www.xia.com).
- [50] R. B. Firestone. *Table of Isotopes*, Volume I, John Wiley and Sons. (1996).
- [51] W. Andrejtscheff, M. Senba, N. Tsoupas and Z. Z. Ding, Nucl. Instr. Meth. **204**, 123 (1982).
- [52] M. Hellström *et al.*, GSI 2003-1, 5 (2003).
- [53] N. Hoteling *et al.*, Phys. Rev. C **76**, 044324 (2007).
- [54] R. Lozeva *et al.*, Phys. Rev. C **77**, 064313 (2008).
- [55] ENSDF database, <http://www.nndc.bnl.gov/ensdf/>.
- [56] J. K. Hwang *et al.*, J. Phys. G: Nucl. Part. Phys. **28**, L9 (2002).
- [57] A. Scherillo *et al.*, Phys. Rev. C **70**, 054318 (2004).
- [58] A. Scherillo, PhD Thesis, University of Cologne (2004).

- 
- [59] F. Naqvi *et al.*, Phys. Rev. C **82**, 034323 (2010).
- [60] M. Pfützner *et al.*, Phys. Rev. C **65**, 064604 (2002).
- [61] N. Iwasa *et al.*, Nucl. Instrum. Methods Phys. Res. B **126**, 284 (1997).
- [62] S. Steer, PhD Thesis, University of Surrey (2009).
- [63] R. Machleidt, Phys. Rev. C **63**, 024001 (2001).
- [64] H. Grawe *et al.*, to be published.
- [65] B.A. Brown *et al.*, Oxbash for windows, MSU-NSCL report, 1289 (2004).
- [66] E. Caurier, G. Martínez-Pinedo, F. Nowacki, A. Poves and A. P. Zuker, Rev. Mod. Phys. **77**, 427 (2005).
- [67] A. De-Shalit, M. Goldhaber, Phys. Rev. **92**, 5 (1953).
- [68] P. Federman, S. Pittel, Phys. Rev. C **20**, 2 (1979).
- [69] I. Talmi, Rev. Mod. Phys. **34**, 4 (1962).
- [70] K. Heyde, P. Van Isacker, R. F. Casten and J. L. Wood, Phys. Lett. B **155**, 5 (1985).
- [71] T. Otsuka, R. Fujimoto, Y. Utsuno, B. A. Brown, M. Honma and T. Mizusaki, Phys. Rev. Lett **87**, 8 (2001).
- [72] T. Otsuka, T. Suzuki, R. Fujimoto, H. Grawe and Y. Akaishi, Phys. Rev. Lett **95**, 232502 (2005).
- [73] H. Grawe, The euroschool lectures on Physics with Exotic Beams, Vol. 1, p. 35 (2004).
- [74] L. Rydström, J. Blomqvist and R. J. Liotta, Nucl. Phys. A **512**, 217 (1990).
- [75] R. Krücken, private communication.
- [76] Facility for Rare Isotope Beams, <http://www.frib.msu.edu/>.
- [77] Système de Production d'Ions Radioactifs en Ligne, <http://www.ganil-spiral2.eu/spiral2-us>.
- [78] <http://www-wnt.gsi.de/agata/introduction.htm>.

- [79] <http://grfs1.lbl.gov/>.
- [80] H. Mach *et al.*, Phys. Rev. Lett. **63**, 143 (1989).
- [81] N. V. Zamfir, R. L. Gill, D. S. Brenner, R. F. Casten and A. Wolf, Phys. Rev. C **51**, 1 (1995).
- [82] Facility for Antiproton and Ion Research, [www.fair-center.org](http://www.fair-center.org).
- [83] T. Glasmacher, Nucl. Phys. A **693**, 90 (2001).
- [84] [www.gsi.de/GSI-Future/cdr/](http://www.gsi.de/GSI-Future/cdr/).
- [85] G. F. Knoll, *Radiation Detection and Measurement*, Third Edition, John Wiley and Sons Inc., New York (1979), p.276.
- [86] G. Montagnoli *et al.*, Nucl. Instr. Methods A **547**, 455 (2005).
- [87] P. Boutachkov *et al.*, Annual report, GSI, 215 (2007).
- [88] R. Lozeva *et al.*, Nucl. Instr. Meth. A **562**, 298 (2006).
- [89] <http://groups.nscl.msu.edu/lise/lise.html>.



# Acknowledgements

It is a pleasure to thank the many people who made this thesis possible. It is difficult to overstate my gratitude to my PhD supervisors, Dr. Magdalena Górska and Prof. Dr. Jan Jolie. When it comes to Dr. Magdalena Górska, her enthusiasm, her inspiration, and her great efforts to explain things clearly and simply, helped to make physics fun for me. Throughout my PhD period, they provided encouragement, sound advice, good teaching, good company, and lots of good ideas. I could not have imagined having better advisors and mentors for my PhD, and without their knowledge and perceptiveness I would never have finished it.

I would like to mention special thanks to Dr. Plamen Boutachkov who has taught me a lot, during my work with him. Discussing and arguing with him was always fun. I am grateful to Dr. Hubert Grawe who introduced me to the concepts of shell-model calculations and through his numerous discussions taught me some interesting physics.

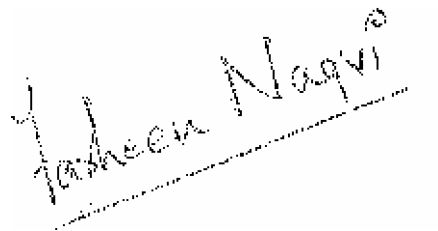
I thank all my teachers specially Dr. Samit Mandal and Prof. Raghuveer Singh from University of Delhi, for inspiring me to do nuclear physics. I have really benefited from various stimulating discussions in the GSI gamma spectroscopy group. It was exciting to attend all those group seminars. I have gained a lot during these, thanks to Dr. Jürgen Gerl, Dr. Hans-Jürgen Wollersheim, Dr. Stephane Pietri, Henning Schaffner, Dr. Ivan Kojouharov, Dr. Cesar Domingo and Dr. Frédéric Ameil. I am indebted to my many student colleagues at GSI for providing a stimulating and fun environment in which to learn and grow is natural. I am especially grateful to Edana Merchán, Namita Goel, Tobias Habermann, Tobias Engert, Eleonora Gregor, Samuel Lago and Patrick Patchakui.

I would also like to thank my colleagues at Cologne specially Dr. George Pascovici and my friends, Bart Bruyeneel, Petra Kudejova and Gabriela Ilie who helped in making my first few days in Cologne really memorable. I am grateful to Dr K. O. Zell, for helping me getting through the German bureaucracy and for assisting me in many different ways. Frau S. Hingott, Frau E. Kroppen and Frau H. Röhnelt all deserve special mention.

I wish to thank my entire extended family for providing a loving environment for me. My siblings and some first cousins were particularly supportive. I also wish to thank all my friends from India for their invaluable support at times. Lastly, and most importantly, I wish to thank my parents. They raised me, supported me, taught me, and loved me. To them I dedicate this thesis.

# Erklärung

Ich versichere, dass ich die von mir vorgelegte Dissertation selbständig angefertigt, die benutzen Quellen und Hilfsmittel vollständig angegeben und die Stellen der Arbeit-einschließlich Tabellen, Karten und Abbildungen-, die anderen Werken im Wortlaut oder dem Sinn nach entnommen sind, in jedem Einzelfall als Entlehnung kenntlich gemacht habe; dass diese Dissertation noch keiner anderen Fakultät oder Universitaät zur Prüfung vorgelegen hat; dass die - abgesehen von unten angegebenen Teilpublikationen - noch nicht veröffentlicht worden ist sowie, dass ich eine solche Veröffentlichung vor Abschluss des Promotionsverfahrens nicht vornehmen werde. Die Bestimmungen dieser Promotionsordnung sind mir bekannt. Die von mir vorgelegte Dissertation ist von Prof. Dr. Jan Jolie betreut worden.

A handwritten signature in black ink, reading "Faheem Naqvi", is written over a horizontal dashed line. The signature is slanted upwards to the right.

Teilveröffentlichungen:

- "Isomer spectroscopy of  $^{127}\text{Cd}$ ", F. Naqvi, M. Górska, L. Cáceres *et al.*, Phys. Rev. C **82**, 034323 (2010).